

AD-A167 849

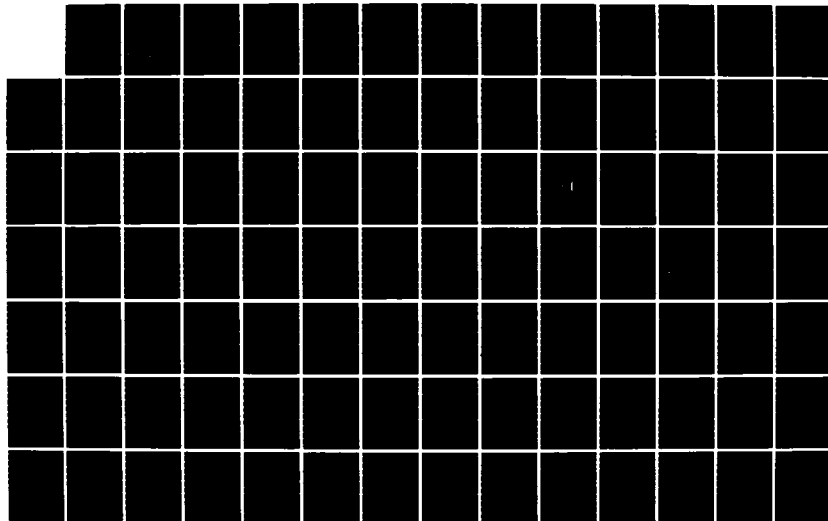
ADVANCED CONCEPTS THEORY ANNUAL REPORT 1985(U) NAVNL
RESEARCH LAB WASHINGTON DC 23 APR 86 NRL-MR-5739

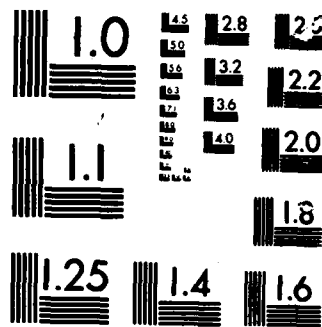
1/2

UNCLASSIFIED

F/G 28/9

NL





MICROCOPY

CHART

2

NRL Memorandum Report 5759

Advanced Concepts Theory Annual Report 1985

*Plasma Radiation Branch
Plasma Physics Division*

AD-A167 849

April 23, 1986

This research was sponsored by the Defense Nuclear Agency under Subtask T99QMXLA,
work unit 00019 and work unit title "Advanced Simulation Concepts."



NAVAL RESEARCH LABORATORY
Washington, D.C.

DTIC
MAY 10 1986



Approved for public release; distribution unlimited.

86 5 19 018

DTIC FILE COPY

REPORT DOCUMENTATION PAGE

1a. REPORT SECURITY CLASSIFICATION UNCLASSIFIED			1b. RESTRICTIVE MARKINGS		
2a. SECURITY CLASSIFICATION AUTHORITY			3. DISTRIBUTION / AVAILABILITY OF REPORT		
2b. DECLASSIFICATION / DOWNGRADING SCHEDULE			Approved for public release; distribution unlimited.		
4. PERFORMING ORGANIZATION REPORT NUMBER(S) NRL Memorandum Report 5759			5. MONITORING ORGANIZATION REPORT NUMBER(S)		
6a. NAME OF PERFORMING ORGANIZATION Naval Research Laboratory		6b. OFFICE SYMBOL (If applicable) Code 4720	7a. NAME OF MONITORING ORGANIZATION Defense Nuclear Agency		
6c. ADDRESS (City, State, and ZIP Code) Washington, DC 20375-5000			7b. ADDRESS (City, State, and ZIP Code) Alexandria, VA 22310		
8a. NAME OF FUNDING / SPONSORING ORGANIZATION Defense Nuclear Agency		8b. OFFICE SYMBOL (If applicable) Code RAEV	9. PROCUREMENT INSTRUMENT IDENTIFICATION NUMBER		
8c. ADDRESS (City, State, and ZIP Code) Alexandria, VA 22310			10. SOURCE OF FUNDING NUMBERS		
			PROGRAM ELEMENT NO. 62715H	PROJECT NO.	TASK NO.
					WORK UNIT ACCESSION NO. DN880-191
11. TITLE (Include Security Classification) Advanced Concepts Theory Annual Report 1985					
12. PERSONAL AUTHOR(S) Plasma Radiation Branch					
13a. TYPE OF REPORT Annual		13b. TIME COVERED FROM 1/85 TO 12/85		14. DATE OF REPORT (Year, Month, Day) 1986 April 23	
				15. PAGE COUNT 122	
16. SUPPLEMENTARY NOTATION This research was sponsored by the Defense Nuclear Agency under Subtask T99QMXLA, work unit 00019 and work unit title "Advanced Simulation Concepts."					
17. COSATI CODES			18. SUBJECT TERMS (Continue on reverse if necessary and identify by block number)		
FIELD	GROUP	SUB-GROUP	Radiation Hydrodynamics		
			Plasma Mixtures		
19. ABSTRACT (Continue on reverse if necessary and identify by block number) This report contains the results of theoretical investigations and analysis on issues concerned with the production, interpretation, and understanding of radiation generated from dense hot plasmas. In particular, the radiation from imploding hollow z-pinch plasmas and ion beam generated plasmas, the influence of radiation on the plasmas' morphology, the x-ray conversion efficiency and spectral emission characteristics, dynamics of double gas puff implosions, imploding plasmas as opening switches, and analyses and interpretation of experimental results. <i>(... of ... discharges)</i>					
20. DISTRIBUTION / AVAILABILITY OF ABSTRACT <input checked="" type="checkbox"/> UNCLASSIFIED/UNLIMITED <input type="checkbox"/> SAME AS RPT. <input type="checkbox"/> DTIC USERS			21. ABSTRACT SECURITY CLASSIFICATION UNCLASSIFIED		
22a. NAME OF RESPONSIBLE INDIVIDUAL Jack Davis			22b. TELEPHONE (Include Area Code) (202) 767-3278		22c. OFFICE SYMBOL Code 4720

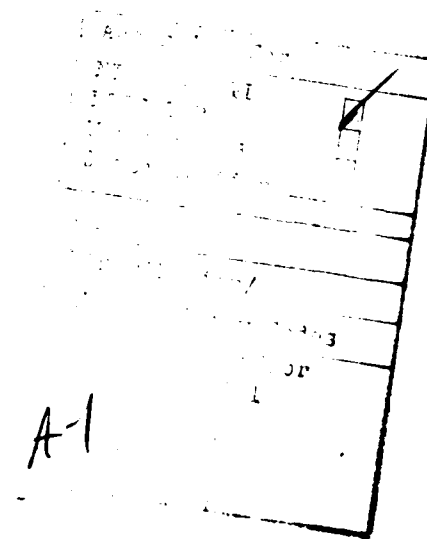
DD FORM 1473, 84 MAR

83 APR edition may be used until exhausted.
All other editions are obsolete.

SECURITY CLASSIFICATION OF THIS PAGE

CONTENTS

PREFACE	iv
A. SPECTRAL ANALYSIS OF GAMBLE SHOTS AND COMPARISON WITH PREVIOUS BLACKJACK 5 PERFORMANCE	1
B. SIMPLODE: A NON-LTE DYNAMIC PINCH MODEL OF IMPLoding GAS PUFF PLASMAS. II. ARGON	6
C. PRISM: PLASMA RADIATION IMPLOSION SOURCE MODEL	30
D. MULTIMATERIAL RADIATION-HYDRODYNAMIC MODELING	37
E. GYROKINETIC PLASMA RADIATION SOURCE CORONA MODEL	57
F. ERODING FOIL SWITCH MODEL FOR MASS FLOW SWITCHES	78
G. PROTON BEAM DEPOSITION, HEATING, AND RADIATION FROM AN Fe PLASMA	88
H. NON-LTE ELECTRON DISTRIBUTIONS IN ELECTRICAL DISCHARGES ...	103
I. ACKNOWLEDGMENTS	107



Preface

The Advanced Simulation Concepts Theory Program at NRL during FY 85 was focused toward applying the computational tools developed in previous years to provide guidance and supervision to the experiments on the GAMBLE II Facility, continue the work on imploding gas puff plasmas, with and without a central core plasma, develop a multimaterial radiation hydrodynamic capability, initiate a program to understand the non-LTE electron distributions in electrical discharges as it relates to and impacts on the understanding and interpretation of experimental results, explore the usefulness of a gyrokinetic corona model to understand the flow of current as the plasma implodes, to continue investigating the x-ray conversion efficiency of proton beams interacting with a planar target, and finally, provide analyses and interpretations of the experimental data.

Numerical simulations were performed to provide guidance, supervision, and interpretation for the gas puff experiments conducted on the GAMBLE II Facility. Comparisons were made between the implosion and radiation dynamics based on current waveforms representative of the generator with and without the plasma erosion opening switch. The numerical simulations were done for both neon and argon gas puff plasmas. The predictions were then borne out experimentally showing that neon was well matched to the GAMBLE II generator in terms of K-shell x-ray production where Argon is not. Most of the K-shell neon x-ray emission resided in the helium- and hydrogen-like resonance lines while argon is a prolific L-shell radiator.

Investigations were also continued on stagnating an imploding gas puff plasma onto a low density core plasma for usefulness as a plasma switch or radiation enhancement. It was determined that the process of stagnation has the effects of stepping-down the photon energy and converting the K-shell photons to L-shell photons. The total yield did not remain constant. In fact, the presence of the post consistently produced a higher total yield in the case of argon than the corresponding implosions in the absence of a central post.

A fully self-consistent multi-material radiation MHD model (DRACHMA) has been developed which includes detailed non-LTE ionization dynamics and radiation transport. An arbitrary number of materials can be treated either as mixtures, discrete shells, or as a combination of the two. Numerical simulations were performed for an argon gas puff plasma imploding on a neon core plasma. The numerical simulations indicate that both

radiation enhancement and filling in of the spectra occurs under the right conditions during the stagnation phase of the implosion.

A new PRS corona model has been formulated on the basis of gyrokinetic theory. Collisionless highly magnetized plasma on the exterior of the PRS load can conduct appreciable current, even when moving at the E/B drift velocity. This gyrokinetic corona has been examined in a self-similar limit and the propagation theory developed into a fully self-consistent nonlinear wave equation.

As an initial foray into the domain of high current opening switches, we have developed the Eroding Foil Switch (EFS) model to explain the observed kinematics of foils exposed to large currents in a coaxial geometry. By calculating the mass erosion rate (from the upstream side of a foil) due to nonlinear magnetic diffusion and ohmic heating, one can obtain a quite detailed and fairly accurate picture of the foil switch conduction phase. We are involved in the Western Research Corp. (WRC) foil switch program as a probable test bed of the EFS model.

The proton beam target interaction studies has continued. Numerical simulations were carried out for beam intensities currently available with existing pulse power generators. Results were obtained for a one MeV mono-energetic proton beam incident on a planar iron target of $\mu 8m$ thickness. The beam is taken to be a square-shaped pulse of 10 nsec duration with a flux of 10^{26} protons $cm^{-2} sec^{-1}$. The simulations of the target response indicate that radiation transport and losses are significant and influence the time history of the temperature and density profiles. Neglect of radiation transport and losses leads, in many cases, to erroneous behavior of the beam plasma interaction.

A program has been initiated to investigate the non-LTE electron distributions in electrical discharges. The electron energy distribution function is the connecting link between the electrical and radiative behavior of electrical discharges; namely, it determines both the strength of the discharge's electrical and thermal conductivities as well as the strength of the ionization and excitation rates, and therefore the radiation loss rates. Thus, it is essential that electron distribution functions be calculated for pulse power x-ray machines, which should be designed to be as energy efficient as is physically possible in converting the heated free electron energy distributions to kilovolt x-rays. Without a good knowledge of the dynamics of the electron distribution function, the

full potentialities of pulse power x-ray generators cannot be well assessed.

From the electrical and thermal conductivities, one calculates the current distributions (and thus the details of the implosion dynamics). Moreover, it has long been appreciated that the conduction properties of pulse power loads are anomalous, i.e. they are not understood in terms of classically calculated Spitzer conductivities. Within the DOE ICF community, flux correctors have long been in use to sharply reduce classical heat conduction in steep temperature and density gradients. Experience has also taught this community that the values of the flux corrector can change markedly depending on experimental conditions. Its use also contributes to the poor agreement that is usually obtained in matching theory with detailed experimental x-ray data. A discussion is presented of the program and its future goals.

Finally, spectral analysis of GAMBLE shots and comparisons were made with previous BLACKJACK 5 performance. The extremely efficient performance of GAMBLE-II (with respect to yield relative to current) clearly indicates the possibility of upgrading the yields of the larger machines like BLACKJACK 5 without increasing their overall power. Employment of a Plasma Erosion Opening Switch (PEOS) on such machines is one obviously promising approach. Current neon puff yields on BLACKJACK 5 are 30 Kj, about a factor of 8 higher than those obtained on GAMBLE-II current of 1.2 MA, strict I^4 scaling would suggest that hundreds of kj could be obtained with neon puffs on BLACKJACK 5. Clearly, this would violate conservation of energy and such an expectation or objective is therefore unrealistic. However, the current yields of 30 kj on BLACKJACK 5 reflect an increase, relative to GAMBLE-II, of less than I^2 .

In addition to the work presented here there have been a number of reports on related activities. They include:

1. Radiative Properties of Puffed-Gas Mixtures: The Case of Optically Thick Plasmas Composed of Two Elements with Similar Atomic Numbers", J. P. Apruzese, and J. Davis, Journal of Applied Physics 57, p. 4349, January 1985.
2. Opacity Broadening as a Density Diagnostics for Spot Spectroscopy", J. Apruzese, Journal of Quantitative Spectroscopy and Radiative Transfer 33, p. 1 February 1985.
3. Radiative Properties of Puffer-Gas Mixtures, D. Duston, J. Davis and C. Agritellis, J. Appl. Phys. 57, 1 February 1985.
4. An Analytic Voigt Profile Escape Probability Approximation, J. P. Apruzese, J. of Quantitative Spectroscopy and Radiative Transfer, 34, p. 447
5. Ion-Beam Deposition, Heating and Radiation from an Aluminum Plasma, J. E. Rogerson, R. W. Clark and J. Davis, Physicial Review A, Vol. 32, May 1985).
6. Memo Report #5609 "The Ionization Equilibrium of Optically Thick Argon Z-Pinch Plasma for Electron Temperatures Between 25 and 65 eV, J. P. Apruzese, P. C. Kepple, and J. Davis, July 1985.
7. Memo Report #5590 "Advanced Concepts Theory Annual Report 1984, Plasma Radiation Branch, June 26, 2985.
8. Memo Report #5613 "Dynamics of Imploding Neon Gas Puff Plasmas - I", R. W. Clark and J. Davis, July 19, 1985.
9. Memo Report #5615 "SIMPLODE: an Imploding Gas Puff Plasma Model I. Neon", J. Davis, C. Agritellis and D. Duston, July 26, 1985.
10. Memo Report # 5482 "Hydrodynamic Response of a Radiation Al Plasma Excited by a Proton Beam", J. E. Rogerson, R. W. Clark, and J. Davis, December 1984.

ADVANCED CONCEPTS THEORY ANNUAL REPORT 1985

A. Spectral Analysis of GAMBLE Shots and Comparison with Previous BLACKJACK 5 Performance

I. INTRODUCTION AND OBJECTIVES

During FY 85, GAMBLE-II at NRL was successfully operated both with and without the Plasma Erosion Opening Switch (PEOS), using neon gas puff loads created with a 2.5 cm diameter supersonic nozzle. One task of the Plasma Radiation Branch related to this work was the analysis of the detailed neon spectra which were emitted on these shots, thereby clarifying the differences in the plasmas produced with vs. without use of the PEOS. When these analyses were complete, a broad-brush comparison of the performance characteristics and efficiency of GAMBLE-II with that of Maxwell Laboratories' BLACKJACK 5 was undertaken.

II. GAMBLE-II NEON PUFF SHOT ANALYSES

A substantial number of successful neon puff shots occurred on GAMBLE-II with and without the PEOS. Experimentally, it has been found that use of the PEOS eliminates any prepulse and reduces the current risetime from ~ 60 ns to ~ 20 ns. The price paid is that typical peak currents with the PEOS are 0.8 - 0.9 MA, while not utilizing the PEOS results in greater peak currents (~ 1.3 MA). Given the expected I^4 yield scaling, one would expect that neon K-shell yields with the PEOS would fall below those obtained without the PEOS by a factor - $(\frac{0.85}{1.30})^4 = \frac{1}{5}$. However, yields obtained with the PEOS were usually only a factor of 2 below those obtained without the PEOS, clearly indicating greater overall efficiency when the PEOS is used. Analysis of prototype spectra with and without the PEOS was undertaken to answer the question: what property or properties of the imploded plasma are responsible for the improvement of yield relative to current when the PEOS is utilized?

Manuscript approved February 3, 1986.

The two shots in which the highest quality K-shell spectral data were obtained are: shot 2531 (no PEOS) and shot 2585 (with PEOS). They are also entirely representative of a much larger data base. We therefore concentrate the spectral analysis on these shots. In each shot over 90% of the radiated K-shell energy was contained in the Ly α and He α lines. The diameter in each case was estimated as 1.8 mm from pinhole images, although some overexposure may render this measurement only an upper limit. Knowing the pulse widths (29 ns for 2531: 21 ns for 2585), the following measured power outputs were obtained.

TABLE OF MEASURED POWER OUTPUTS

<u>SHOT</u>	<u>Ly α POWER</u> <u>(Joules/nsec)</u>	<u>He α POWER</u> <u>(Joules/nsec)</u>	<u>PEAK CURRENT (MA)</u>
2531 (no PEOS)	8.0	26.4	1.30
2585 (with PEOS)	15.0	12.0	0.83

Using the collisional-radiative-equilibrium (CRE) model of the Plasma Radiation Branch, excellent spectral fits matching all the above line powers to better than 8% were found for the plasma parameters given below. These parameters may be interpreted as representative time- and space-averaged values for those shots.

<u>SHOT</u>	<u>TEMPERATURE (eV)</u>	<u>ION DENSITY (CM⁻³)</u>
2531 (no PEOS)	150	4.0×10^{19}
2585 (with PEOS)	185	3.4×10^{19}

The higher temperature achieved in the PEOS shot 2585 is reflected in its higher Ly- α power as seen in the first table presented above. Therefore, the PEOS - created plasmas seem to be better neon K-shell radiators because they are somewhat hotter than non-PEOS - created plasmas while preserving about the same size and density. The above densities constitute nearly 100% of the cold neon gas originally puffed in for the shots. This is in severe contrast to BLACKJACK 5's plasmas analyzed previously by NRL, as seen below.

III. COMPARISON OF PREVIOUS BLACKJACK 5 AND CURRENT GAMBLE-II PERFORMANCE

Based on mature, detailed spectroscopic analyses of aluminum/argon for BLACKJACK 5, and neon presented above for GAMBLE-II, we can now compare the plasma parameters obtained with both machines as they relate to the machine parameters.

The following table is self-explanatory.

COMPARISON OF BLACKJACK 5 AND GAMBLE-II

<u>Machine or Plasma</u> <u>Property</u>	<u>BLACKJACK 5</u>	<u>GAMBLE-II</u>
Peak Current	3.5-5 MA	0.8 - 1.4 MA
Current Risetime	70 nsec (main pulse)	60 ns (no PEOS); 20ns (PEOS)
Implosion relative to current risetime	peak density occurs within 10ns of current peak	peak density occurs 110 nsec after current start
Loaded Mass fraction ending up in K-shell plasma	20 %	> 70%

Fraction of radiation which is K-shell	30-50%	> 70%
K-Shell pulse radiating time	10-20ns	20-40ns
Ion densities achieved	few x 10^{19}	few x 10^{19}
Temperature achieved	300 eV - 1800 eV	100-200 eV
K-shell yields achieved	up to 40 kJ	up to 4 kJ

It is clear from the above table that GAMBLE-II ultimately incorporates a much larger fraction of the cold loaded mass into the K-shell plasma, and, correspondingly, a much larger fraction of its emitted radiation is K-shell lines. Detailed energy budgets confirm that a lot of BLACKJACK 5's wires and argon puffs ended up as L-shell ions emitting L-shell radiation.

IV. IMPLICATIONS FOR DNA OBJECTIVES

The extremely efficient performance of GAMBLE-II (with respect to yield relative to current) clearly indicates the possibility of upgrading the yields of the larger machines like BLACKJACK 5 without increasing their overall power. Employment of a Plasma Erosion Opening Switch (PEOS) on such machines is one obviously promising approach. Current neon puff yields on BLACKJACK 5 are 30 KJ, about a factor of 8 higher than those obtained on GAMBLE-II. However, with a peak BLACKJACK current of 3.7 MA, as opposed to GAMBLE-II current of 1.2 MA, strict I^4 scaling would suggest that hundreds of kJ could be obtained with neon puffs on BLACKJACK 5. Clearly, this would violate conservation of energy and such an expectation or objective is therefore unrealistic. However, the current yields of 30 kJ on BLACKJACK 5 reflect an increase, relative to GAMBLE-II, of less than

I². Certainly these yields can be improved, and we strongly recommend systematic experimentation with different nozzle radii and plenum pressures.

B. SIMPLODE: A Non-LTE Dynamic Pinch Model of
Imploding Gas Puff Plasmas. II. Argon

I. INTRODUCTION

In an earlier paper¹ results were presented on the radiation dynamics of an imploding neon gas puff plasma for conditions typical of the GAMBLE II pulse power generator at NRL. It was shown that for a variety of initial conditions the neon gas puff is a well matched load for GAMBLE II producing upwards of 6 kilojoules of K-shell radiation, with the bulk of the line radiation emanating from the resonance lines of hydrogen- and helium-like neon. It was further observed that the peak of the K-shell radiative yield occurred well after the peak in the current pulse suggesting that it may be possible to enhance the radiative yield by optimizing the implosion dynamics. Although the yields are strongly dependent on peak current, results indicate that application of the PEOS (Plasma Erosion Opening Switch) improves the quality of the implosion, i.e., the re-assembled plasma exhibits less flaring and appears more uniform. However, further experimentation with the PEOS is necessary before we can say with certainty that it further enhances the K-shell yield and improves significantly the quality of the implosion.

In this paper we focus our attention on argon gas puff plasmas. Interest in argon is twofold: (1) provide estimates of the radiative yield for a variety of puff gas and machine conditions and (2) investigate the feasibility of creating conditions favorable to supporting a population inversion and lasing in the $3\ell-3\ell'$ transitions in neon-like argon. Preliminary calculations indicate that it may be possible to generate conditions favorable to lasing. These results are being reported on elsewhere.² The objective of this investigation is to characterize the radiation dynamics of an imploding argon gas puff plasma in much the same fashion as we did for neon. Unlike neon, argon is not a particularly well matched load to the GAMBLE II generator for producing prolific K-shell yields. However, the disappearance of K-shell radiation will more than be made up for by the appearance of prolific L-shell yields. All the calculations are made with the SIMPLODE code containing an argon non-LTE ionization dynamic model which has been reported on elsewhere.³

II. RESULTS AND DISCUSSION

For reference purposes we will present results showing how some of the key plasma parameters vary in time as the implosion evolves. The standardized case is represented by a 30 $\mu\text{gm/cm}$ argon gas puff plasma with initial outer (inner) radius of 1.55 cm (0.95 cm) and a total column length of 4 cm. The mass distribution is uniform and homogeneous. The current waveform driving the implosion is shown in Figure 1 and has a peak value of 0.875 megamps. The shape of the current waveform is typical of the GAMBLE II generator with the PEOS with the exception of the tail beyond about 150 nsec which has been installed for computational expediency. The experimentally measured current may have a longer decay time. However, since it is the peak current that dictates much of the implosion dynamics of interest here, we shall ignore the differences. In Figure 2 the temporal history of the inner (A) and outer (B) radius is shown. Note that the inner radius collapses on axis in about 125 nsec and that the outer radius pinches to 0.18 cm (which is about 1/10 the initial radius) and exhibits a bounce at about 200 nsec indicating that both temperature and density achieve values high enough to produce a gas pressure that retards and exceeds the magnetic pressure. Correspondingly, the velocity reaches a maximum value of 13cm/ μsec at 150 nsec and becomes zero at the bounce point, as shown in Figure 3. The ion density is shown in Figure 4 and indicates a peak ion density of about $5 \times 10^{19} \text{ cm}^{-3}$ at the time of peak compression - the bounce point. Similarly, in Figure 5 the temporal behavior of the temperature is presented. The temperature peaks at about 170 nsec with a maximum value of about 180 ev. The total radiative yield as a function of time over the 4 cm column length is shown in Figure 6. The peak value is about 1.7 kjoules and occurs roughly at the bounce time. Note that the temperature and density peak at different times. This is caused by radiative cooling as the plasma runs in. This can be seen by comparing with the radiative yield curve in Figure 6. The plasma starts radiating significantly at about 180 nsec and has a total radiation pulse of about 40 nsec. The overwhelming contribution to the radiative yield comes from the L-shell and will be shown and discussed in detail later. These Figures summarize the behavior of some of the key plasma parameters characterizing the implosion and radiative dynamics associated with our

reference case. It is apparent from this reference case, which will be shown to be a judicious choice, that argon is not well suited to GAMBLE II in terms of producing significant K-shell radiation but is well suited for generating interesting levels of L-shell radiation.

We will now summarize the results of a series of numerical simulations fixing either the mass or the thickness of the plasma sheath, $\Delta r = R_B - R_A$. The simulations were performed for two typical current waveforms: the no-switch case, which is the current waveform associated with the GAMBLE II generator without the PEOS, having a peak current of 1.25 Megamp which is achieved in 70 ns and is shown in Figure 7, and the current waveform with the PEOS shown in Figure 1 and already discussed in the context of Figures 2-6. Because of the voluminous amount of data it was decided that the best way to present the results was to choose the maximum value of the appropriate variable from each computer run and plot it as a function of mass per unit length or sheath thickness. For example, for fixed Δr , corresponding to $R_B - R_A (= 1.55 - 0.95) = 0.60$, the maximum velocity, V_{\max} , is shown in Figure 8 as a function of mass per unit length for both current waveforms. In comparing the differences between the two current cases it is evident that the higher peak current case gives rise to higher peak implosion velocities. The higher the current the greater the magnetic acceleration the faster the implosion velocity for a fixed mass of plasma. In Figures 9 and 10 are displayed the peak temperatures and ion densities. For low values of M/l the kinetic energy of runin is sufficiently large such that as the plasma reassembles it thermalizes at a high temperature which causes the following events: (1) the plasma overheats causing a burn through of the ionization stages and radiates as a bremsstrahlung emitter, which is not very efficient in cooling the plasma and (2) because of the high temperature the back pressure is high at relatively low densities impeding the implosion and produces to a "hollow implosion", i.e., the plasma cannot compress to relatively high densities which accounts for the behavior shown in Figures 9 and 10. As M/l increases the driving current becomes less effective in generating high implosion velocities which means there is less energy available for conversion to thermal energy. Hence, the plasma temperature is reduced and the implosion proceeds as shown in the Figures 9 and 10. The peak density exhibits broad profile reaching a value of approximately 10^{19} ions/cm³ in

the switch case. The behavior of the peak ion density as a function of M/l can be explained in terms of the driving current. In the switch case as M/l increases, the peak density first increases, then levels off and subsequently decreases. This behavior can be understood as follows: for low and moderate values of M/l the current is over- and well - matched to the load, respectively, in terms of the velocity, temperature, and achieved density. However, as M/l increases the mismatch between current and load also increases producing slower implosion velocities and subsequently reduced peak densities. In the no-switch case very large values of M/l were not considered, so the effect is not shown. However, for large enough M/l similar behavior to the switch case would be observed. The peak K- and L-shell radiative yield as a function of M/l is shown in Figure 11 for $\Delta r = 0.60$. Since the yield is a strong function of density and temperature the behavior of the curves is self-evident. The peak yield with the switch achieves a maximum value of about 3.8 kJ at approximately 22 $\mu\text{g}/\text{cm}$ while the no switch case has a maximum value of about 6 kJ at about 35 $\mu\text{g}/\text{cm}$ for a 4 cm long plasma column. These values are in reasonably good agreement with the experimental observations.⁴

Another series of numerical simulations were performed varying Δr for fixed M/l . The outer radius was chosen fixed at 1.55 cm while the inner radius was permitted to vary from 0.55 to 1.25 cm. The fixed value for M/l was chosen as 30 $\mu\text{g}/\text{cm}$. Figures 12-15 show the peak values of velocity, temperature, density, and yield, respectively, as a function of Δr . The peak velocity decreases as Δr increases for both current waveforms. This simply reflects the fact that for small Δr the inner boundary has further to go and experiences little or no back pressure whereas for large Δr the inner boundary reaches the axis early in time and allows buildup of back pressure which inhibits the implosion velocity. Hence, the peak velocity is greater for smaller Δr . Peak temperatures and densities are shown in Figures 13 and 14 respectively. The peak temperature in the no switch case decreases as Δr increases mainly because the quality of the implosion deteriorates resulting in a cooler plasma. This behavior is tied to the lack of a good compression as shown in Figure 14 for the peak ion density as Δr increases for fixed mass and $j \times B$ force. In the switch case the peak temperature remains relatively constant over the range of Δr values. This just reflects the fact that it is possible to heat a portion of the

plasma to about 180 eV - the plasma doesn't get sufficiently hot enough to radiate prolifically so that the temperature is not significantly reduced by radiation cooling. This is further borne out in Figure 14 where the peak ion density decreases as Δr increases, indicating a reduction in the peak ion density, thereby reducing the number of emitters available to cool the plasma. In Figure 15 the peak yields for this series of simulations is presented. As Δr increases the no switch peak yield increases, peaks, and then decreases whereas the switch peak yield steadily decreases as Δr increases indicating the the best peak yields for this case occur when the temperature and density are also high. Note, however, that the yield scale (vertical axis) does not vary greatly - in fact the difference between the highest and lowest values differ by about 10% for both current waveforms indicating that the initial implosion conditions conspired in such a way as to generate peak values of temperature and density so as to produce little variation in the peak yield.

Figure 16 displays the temporal variation of the L- and K-shell radiated power for the $M/l = 30 \text{ } \mu\text{g}/\text{cm}$ and $R_B(R_A) = 1.55 (0.95) \text{ cm}$ case superimposed on the PEOS current waveform. The peaks in the thermal L- and K-shell emission profiles occur at slightly different times with the K-shell peak just preceding the L-shell peak. This is in qualitative agreement with the observations.⁴ However, the K-shell radiative yield is significantly greater in the experiments than predicted by SIMPLODE. A possible explanation for this disparity is that the experimental K-shell yield is due, for the most part, to nonthermal energetic electrons as suggested by Jones and Kania.⁵ The L-shell accounts for most of the radiated power and peaks around 2 terrawatts. The K-shell radiated power for these conditions is in the noise. Note also that the peak radiated power comes well after the peak in the current pulse. This behavior was also observed in the neon implosions for current waveform having sharp risetimes. Apparently the plasma absorbs the energy and just percolates for a time and then coasts in until it reassembles on axis.

Finally, in Figure 17 the total emission spectra is shown for $M/l = 35 \text{ } \mu\text{g}/\text{cm}$ and $R(R_B)_A = 1.55 (0.95) \text{ cm}$ for the switch case at 177 nsec into the run, which is near the peak in temperature. The ion density at this time is about $1.8 \times 10^{18} \text{ cm}^{-3}$ and the average charge state is 12.56. The final pinched radius is 0.28 cm. All of the lines appearing in

the spectra are L-shell lines with the peak emission occurring at bands centered around 20, 70, and 400 eV. The free-bound continuum around 1 keV falls off rapidly and the K-shell thermal emission is virtually extinct at the temperature associated with the implosion.

III. SUMMARY

A number of numerical simulations using the SIMPLODE code were performed to describe the behavior of an argon gas puff plasma using machine parameters typical of the NRL GAMBLE II pulse power facility. The SIMPLODE code is a 0-D non-LTE dynamic pinch model and should be interpreted as a "scopping" code and is not presented as gospel. Its virtues are a valid treatment of the non-LTE ionization dynamics and radiation, phenomenological representation of the implosion dynamics, and rapid running on a Vax computer. Its principal deficiency is that some of the relevant physics is deleted such as field and current penetration, development and growth of instabilities, and plasma transport properties, to mention a few. However, it must be said that in comparison with more sophisticated multidimensional radiation MHD codes such as PRISIM, SIMPLODE simulates the overall morphology of the implosion physics with the exception of instabilities and provides reasonable agreement with the radiation yields. It is in this context that SIMPLODE is applied.

The results of the simulations shows that argon gas puff plasmas can be heated and compressed to temperatures and densities, respectively, with the GAMBLE II generator, that produce a good plasma radiation source in the soft x-ray region of the spectra with yields of the order of 2-2.5 terrawatts over a 30-40 ns pulse. For fixed $\Delta r = 0.60$, the yield has a peak value of about 6 kJ for an $M/l = 32 \text{ } \mu\text{g}/\text{cm}$ for the no switch case and a peak yield of about 4 kJ for an $M/l = 20 \text{ } \mu\text{g}/\text{cm}$ for the switch case. For a fixed $M/l = 30$, the peak yield as a function of Δr between 0.30 and 0.90 cm maintaining the outer radius fixed at 1.55 cm remains in the neighborhood of 5 to 6 kJ for the no switch case and between 1.6 to 1.75 kJ for the switch case. Obviously higher yields favor lower M/l in the switch case because of the lower peak current.

In conclusion, even with the limited parameter space investigated, imploding an argon gas puff plasma on the GAMBLE II generator produces an efficient L-shell soft x-ray plasma radiator source.

References

1. R. W. Clark, J. Davis, F. Cochran, Phys. Fluids, to be published.
2. J. Davis, J. P. Apruzese, C. Agritellis, and P. C. Kepple, 3rd International Conference on Radiative Properties of Hot Dense Matter, Williamsburg, Va. (1985) Proceeding to be published.
3. D. Duston, R. W. Clark, J. Davis, and J. P. Apruzese, Phys. Rev. A 27, 1441, March (1983).
4. F. C. Young, S. Stephanakis, et al., Bull. APS 30, 1426 (1985).
5. D. R. Kania and L. A. Jones, Phys. Rev. Lett. 53, 166 (1984).

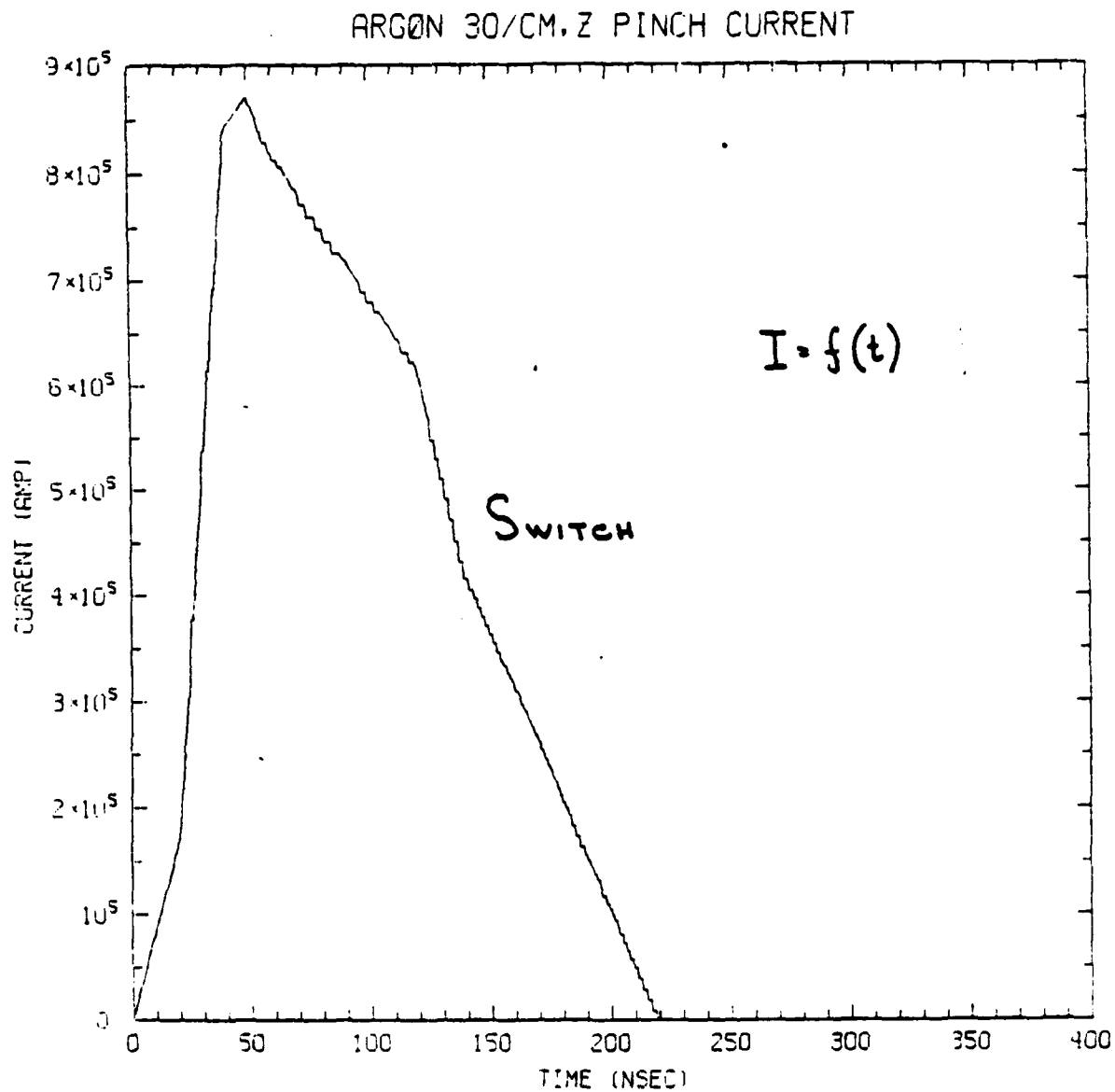


Fig. 1. PEOS Current as a function of time.

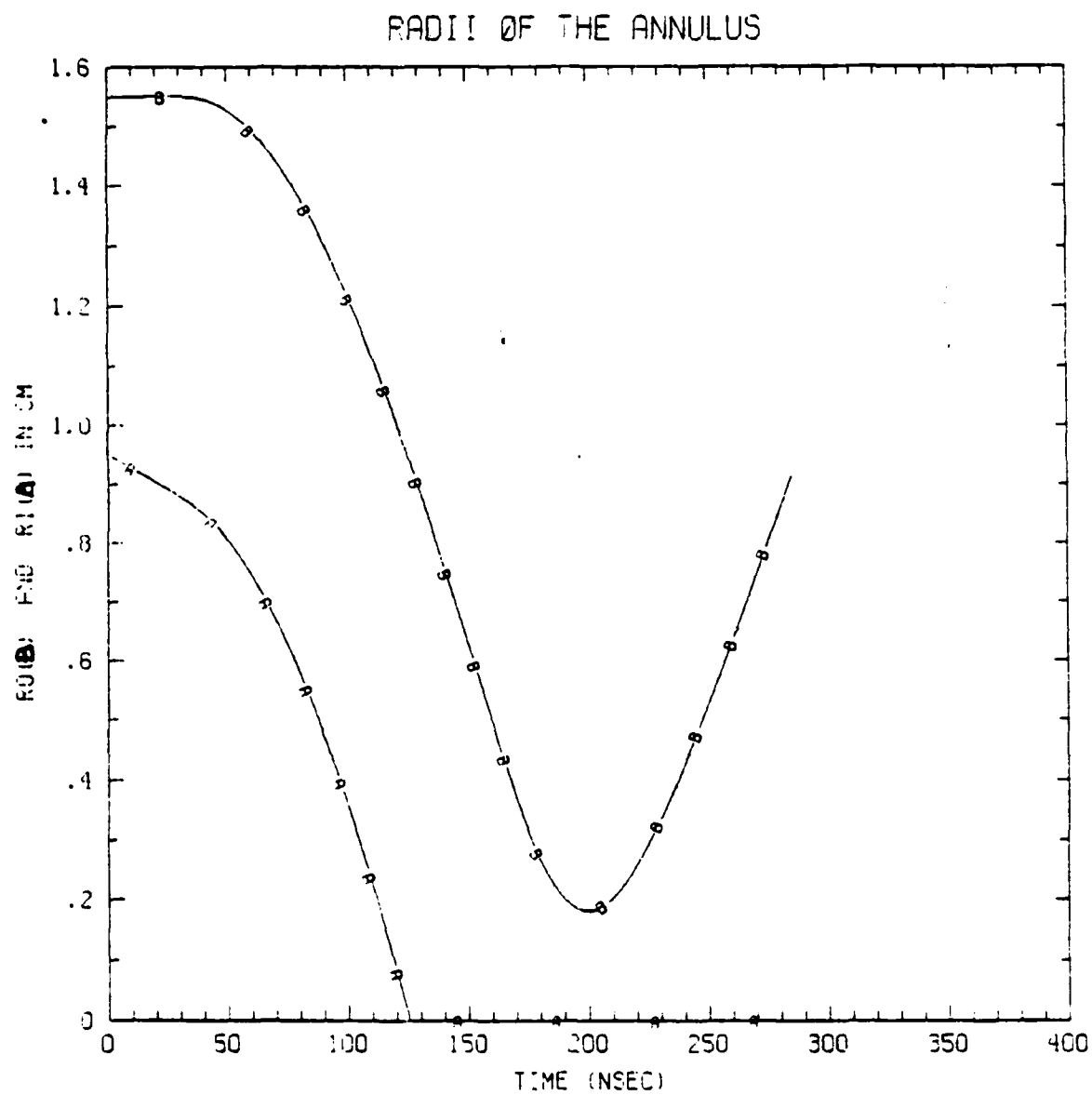


Fig. 2. Radius as a function of time.

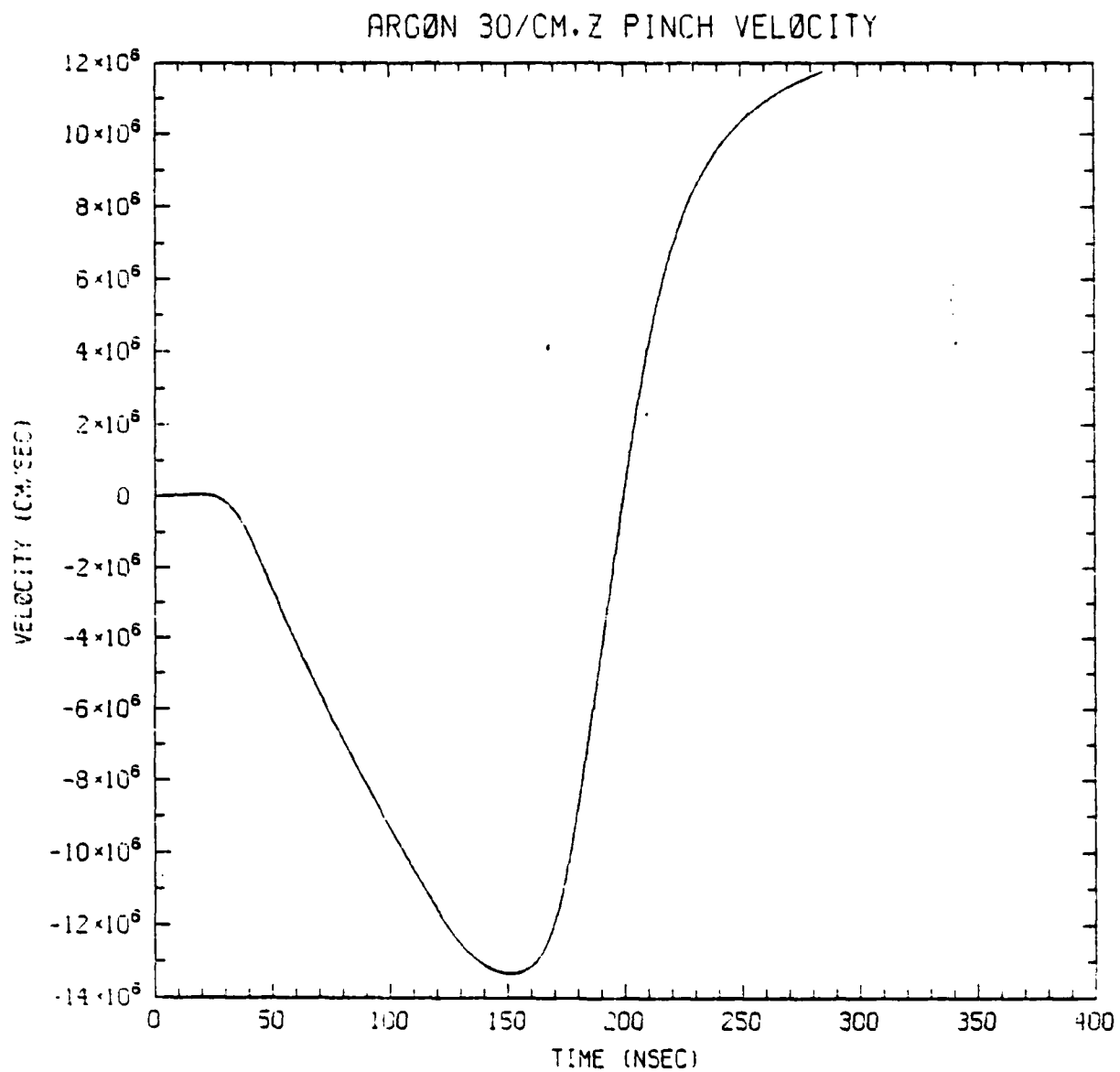


Fig. 3. Velocity as a function of time.

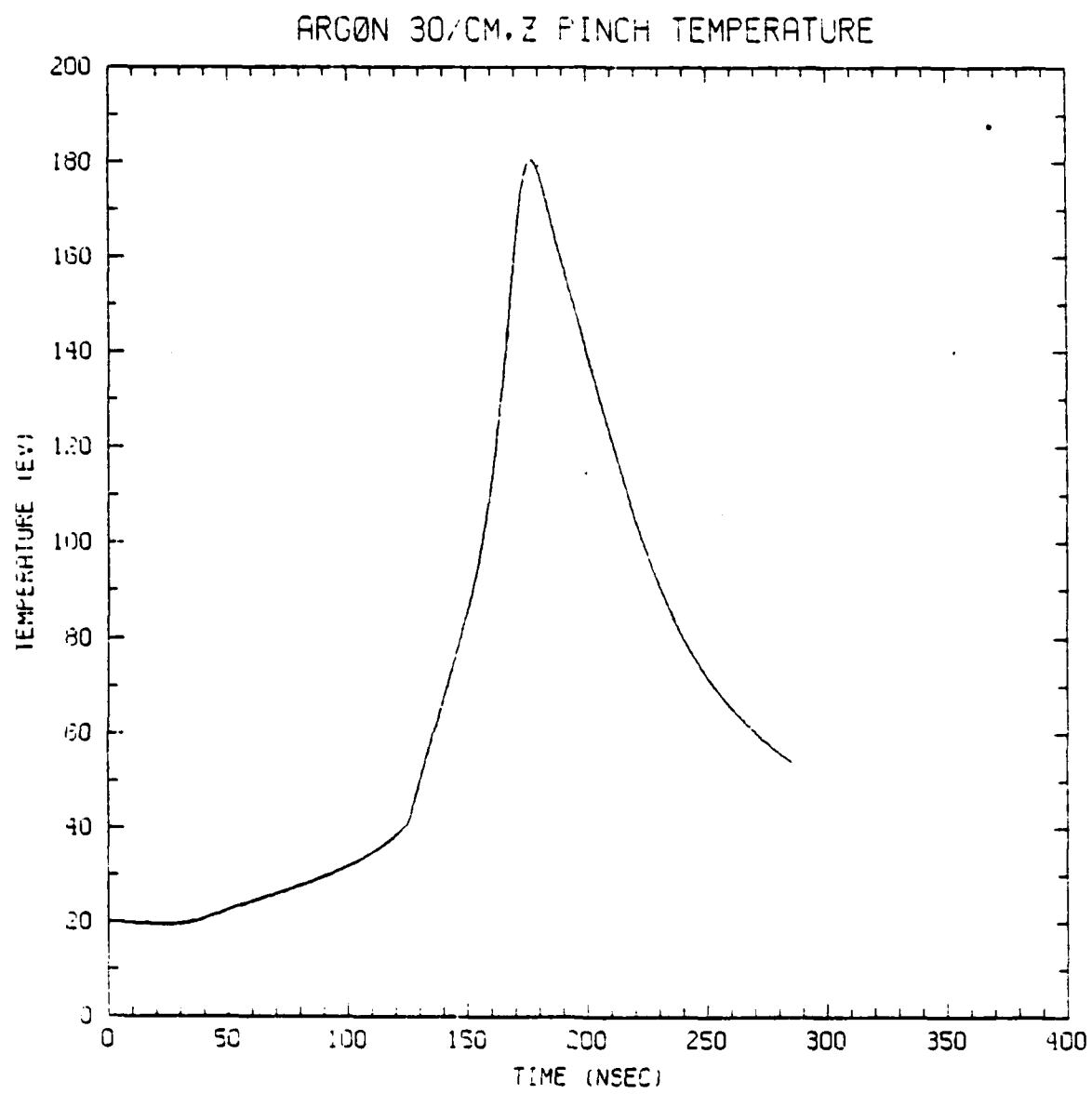


Fig. 4. Temperature as a function of time.

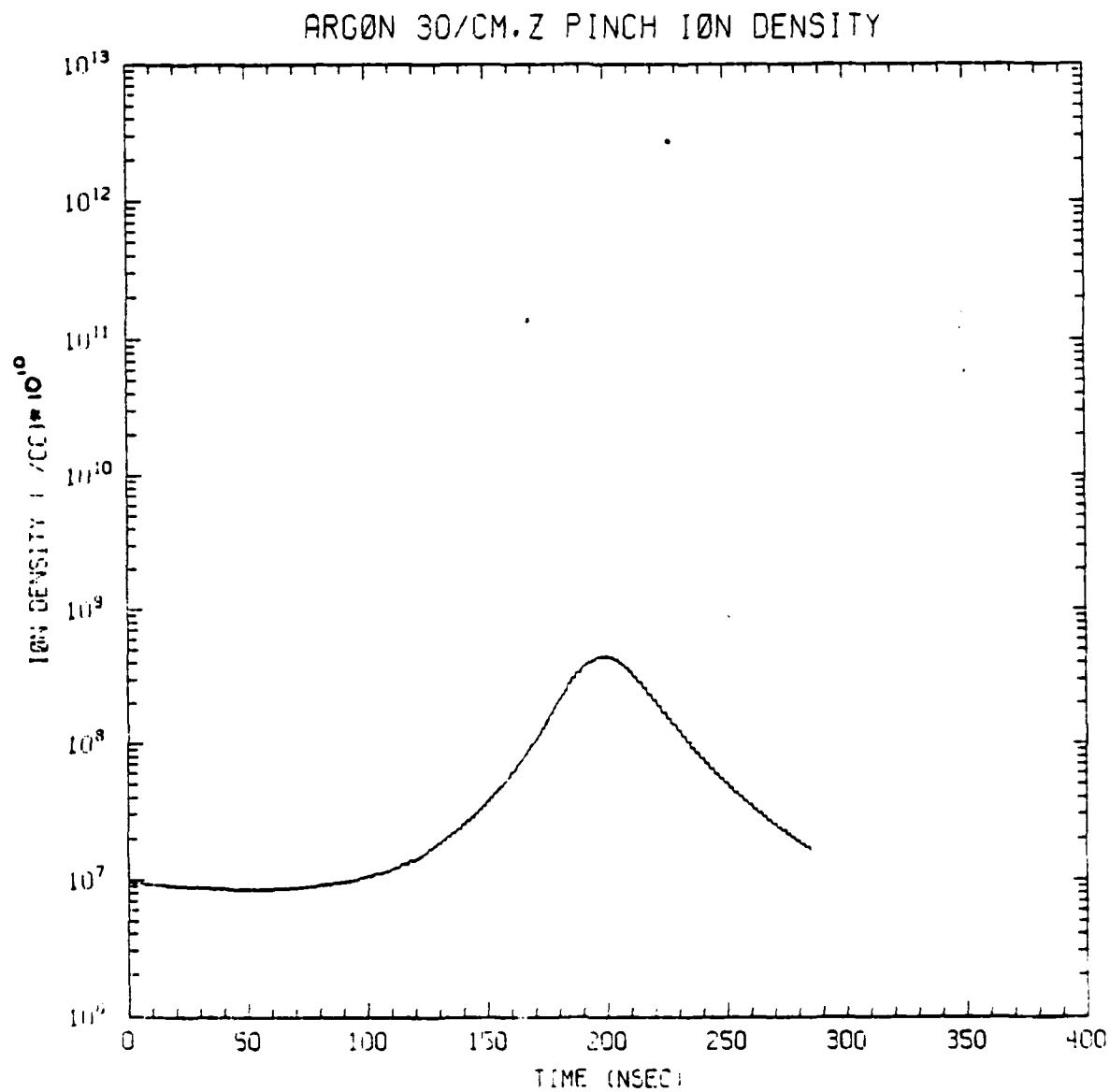


Fig. 5. Ion density as a function of time.

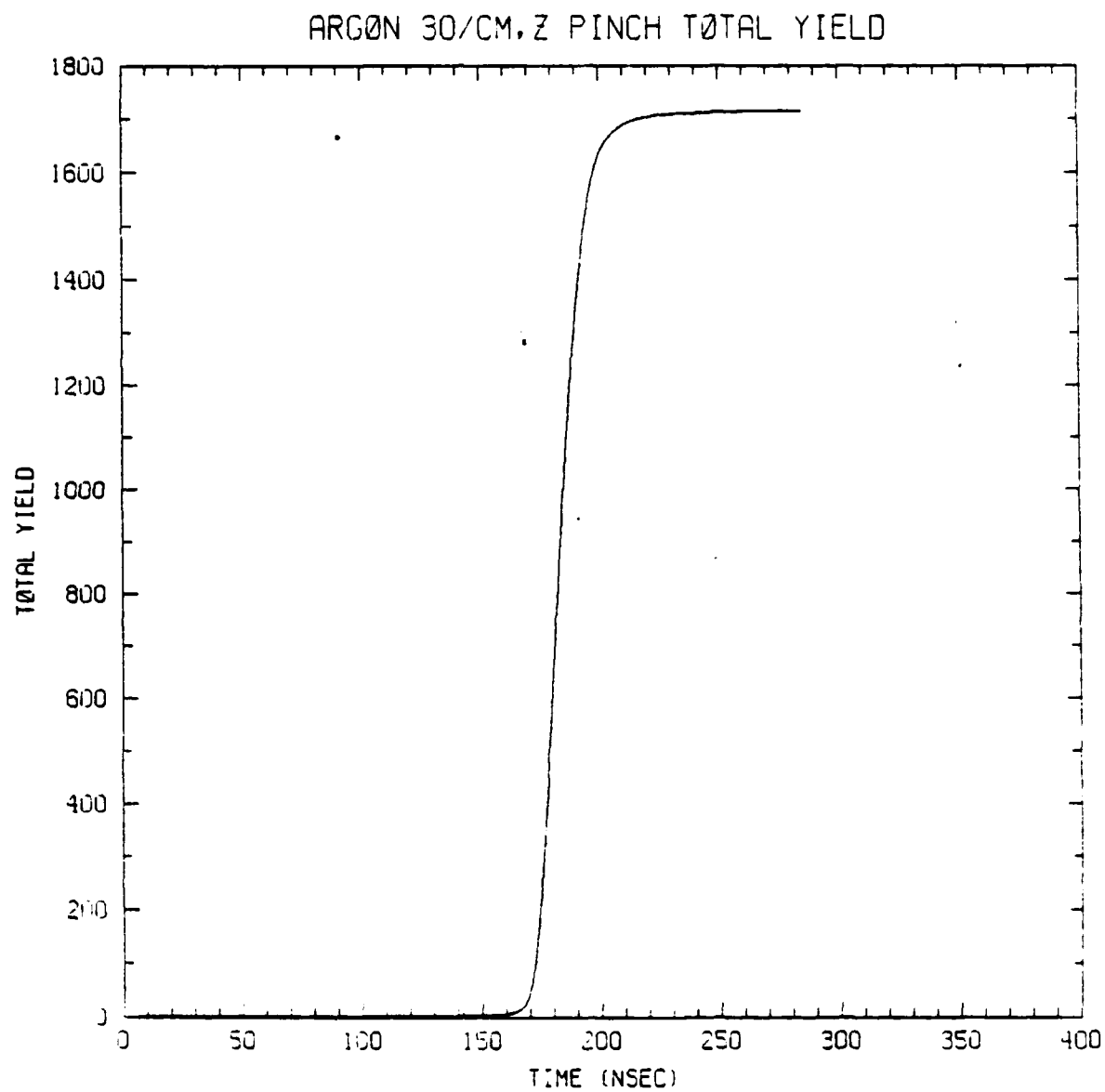


Fig. 6. Total yield as a function of time.

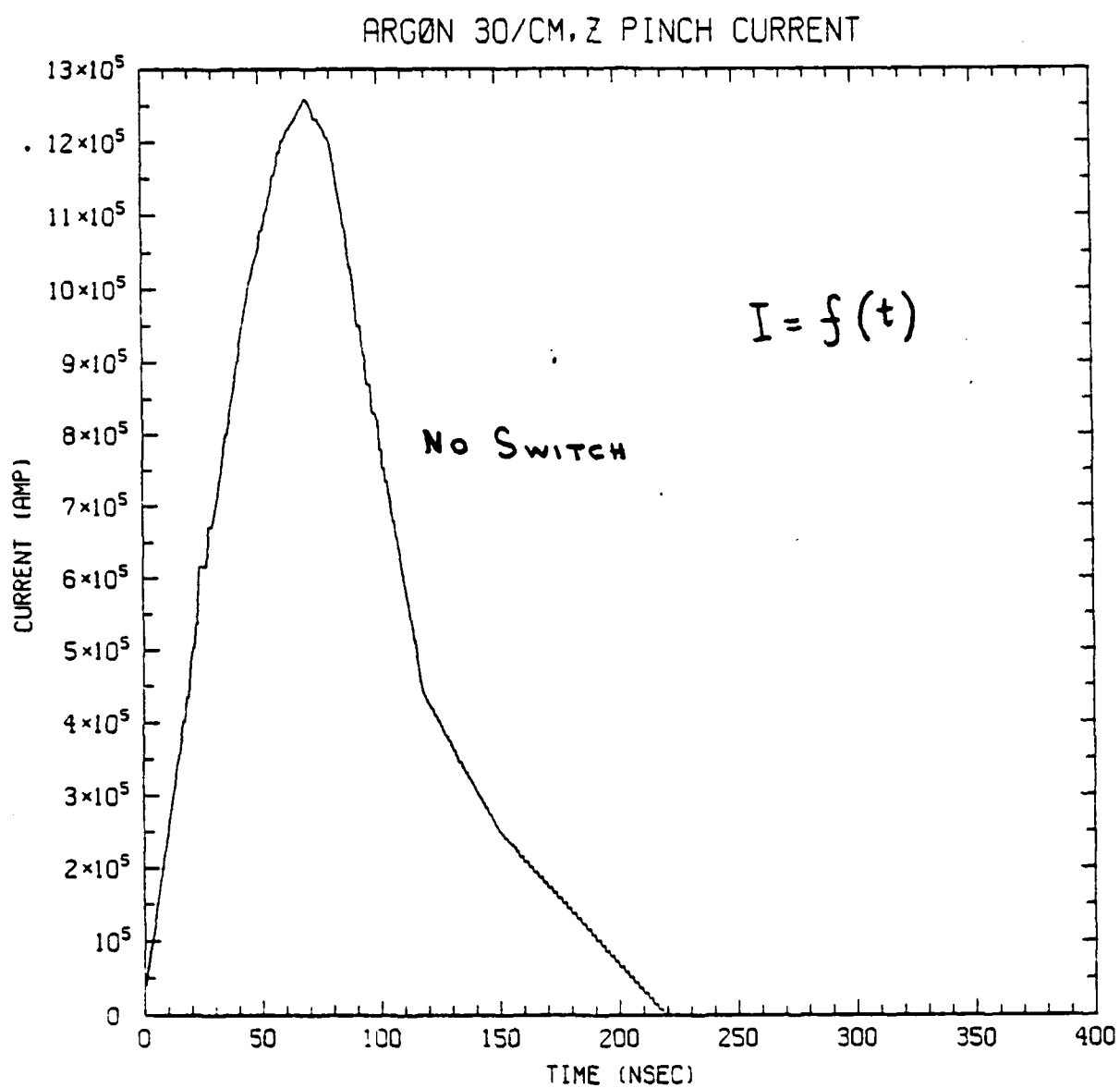


Fig. 7. Current as a function of time.

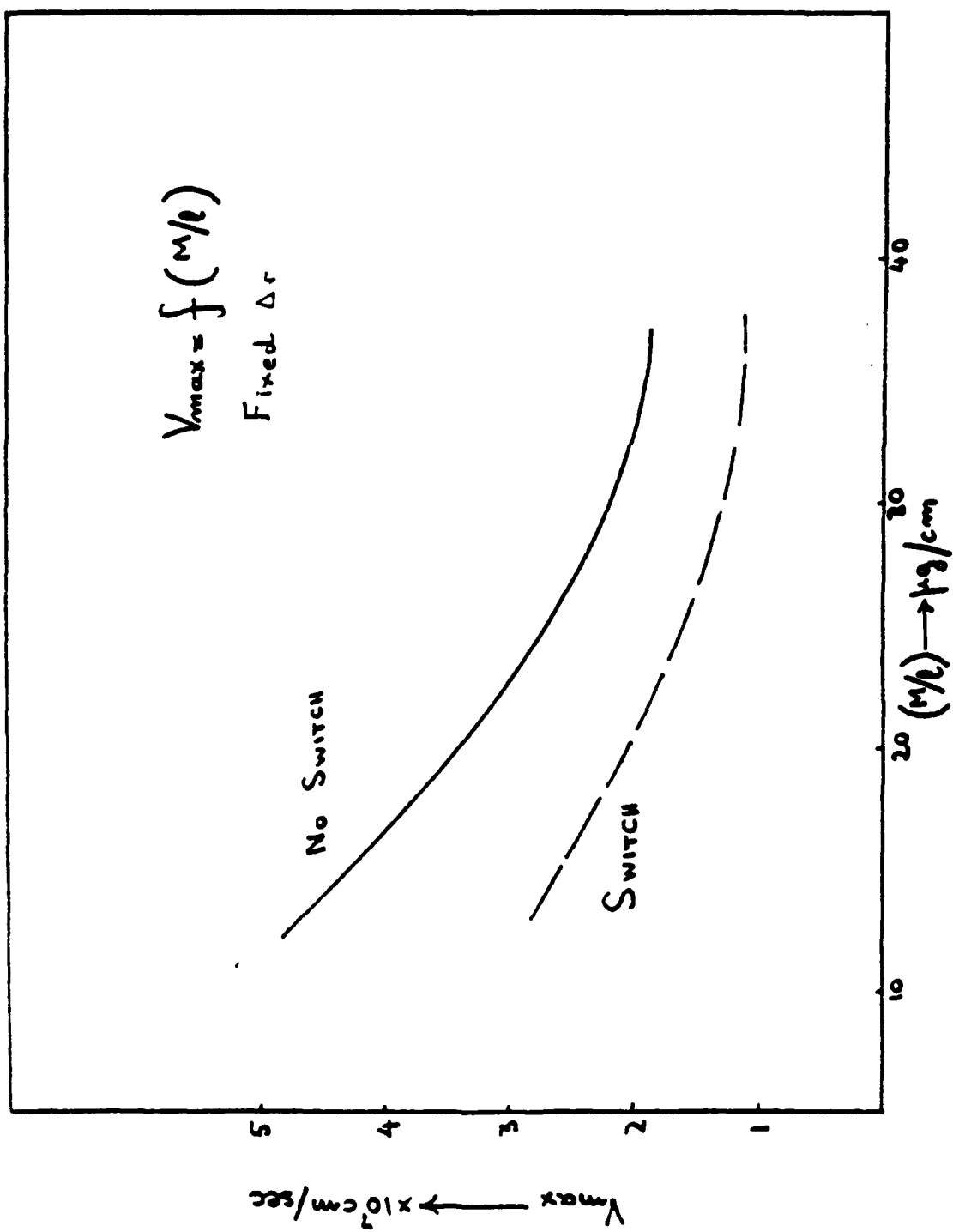


Fig. 8. Maximum velocity as a function of mass per unit length.

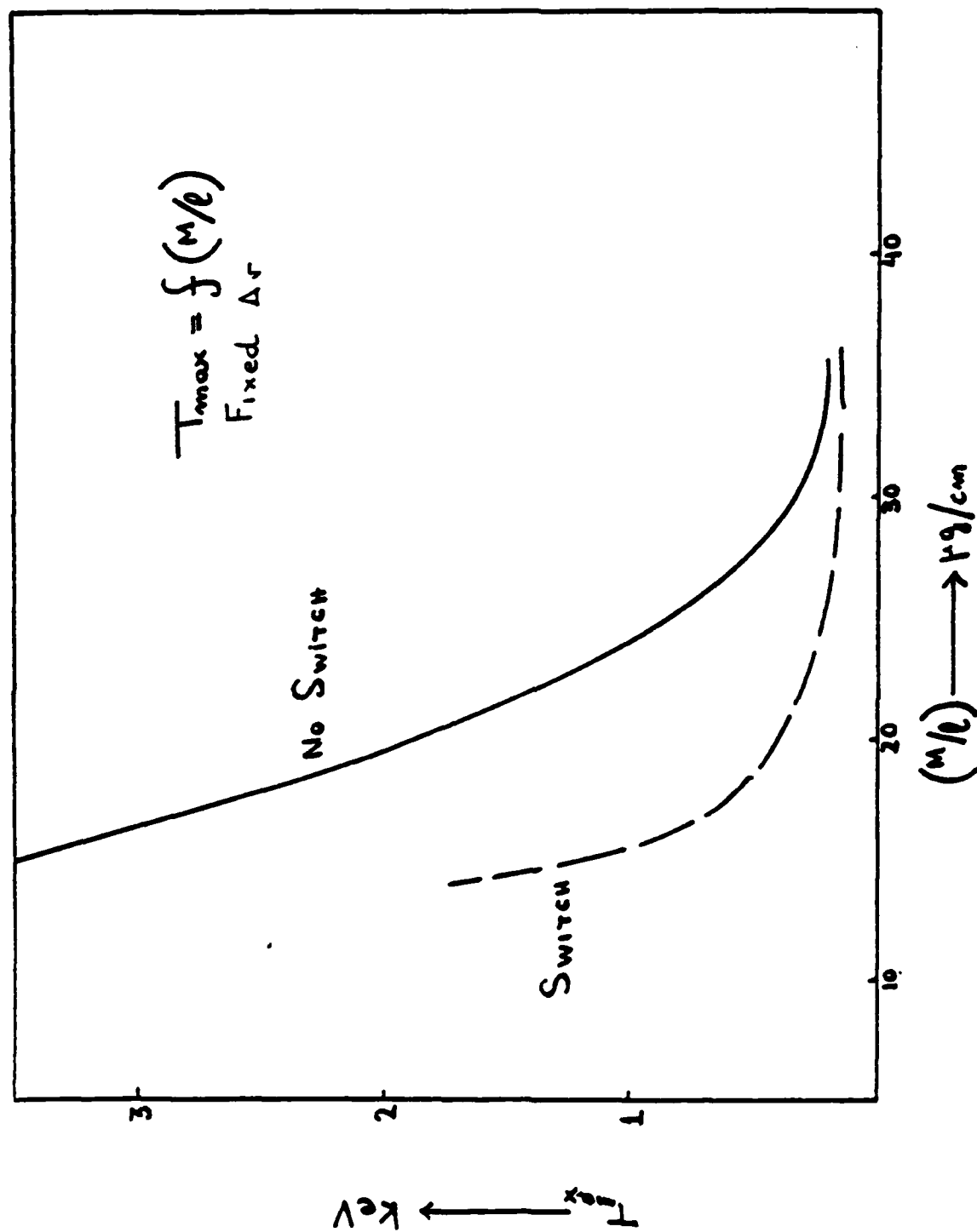


Fig. 9. Maximum Temperature as a function of mass per unit length.

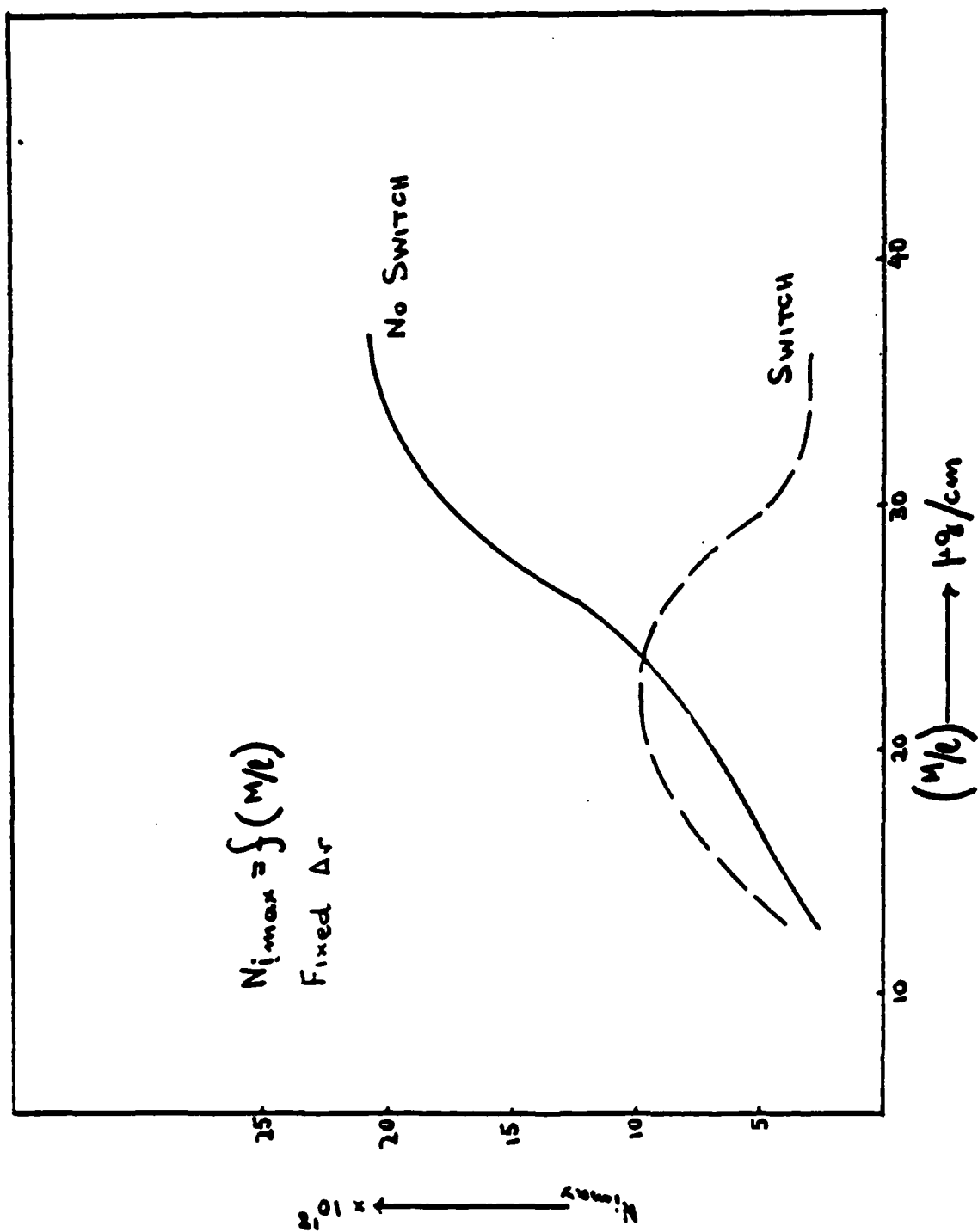


Fig. 10. Maximum ion density as a function of mass per unit length.

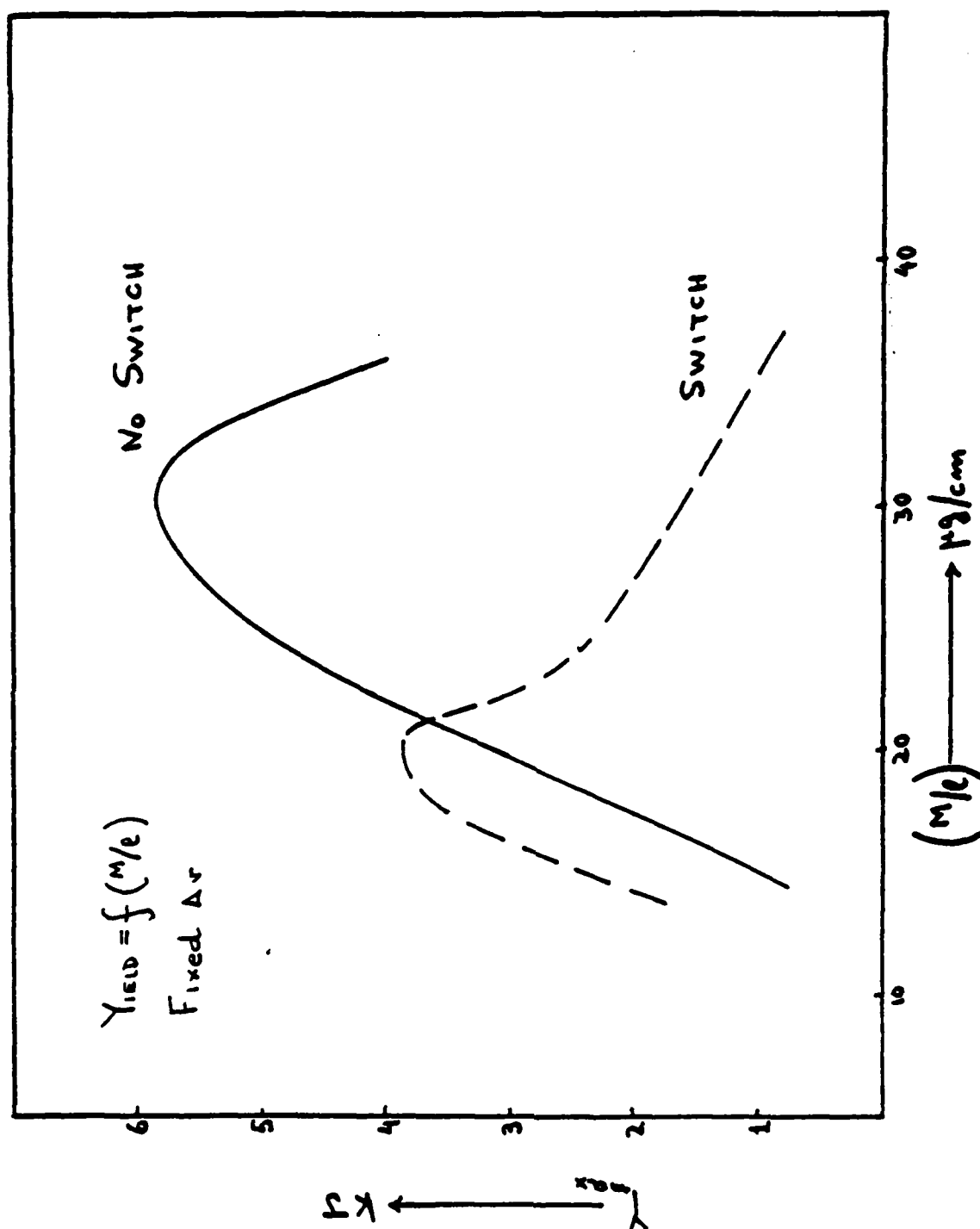


Fig. 11. Maximum yield as a function of mass per unit length.

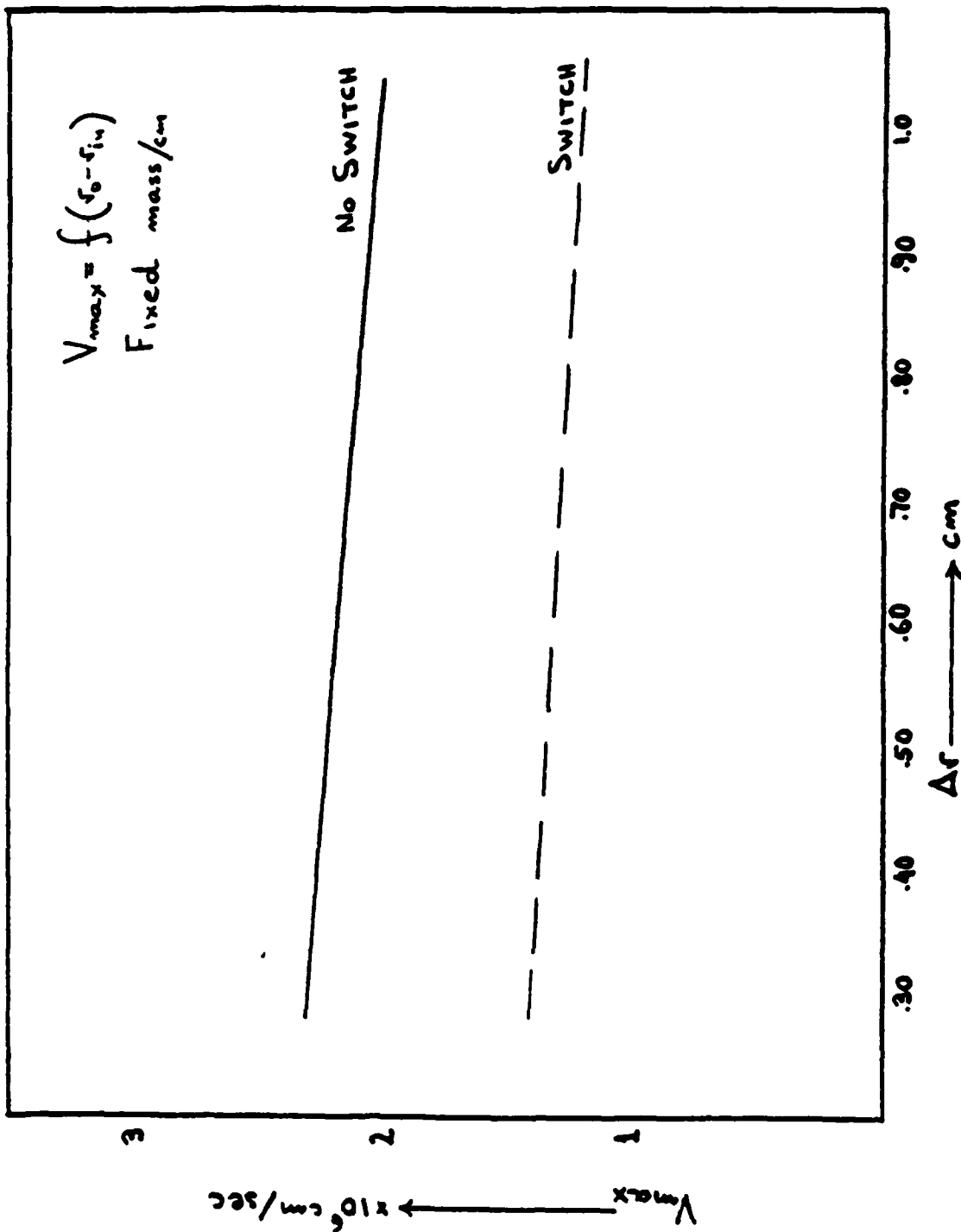


Fig. 12. Maximum velocity as a function of shell thickness.

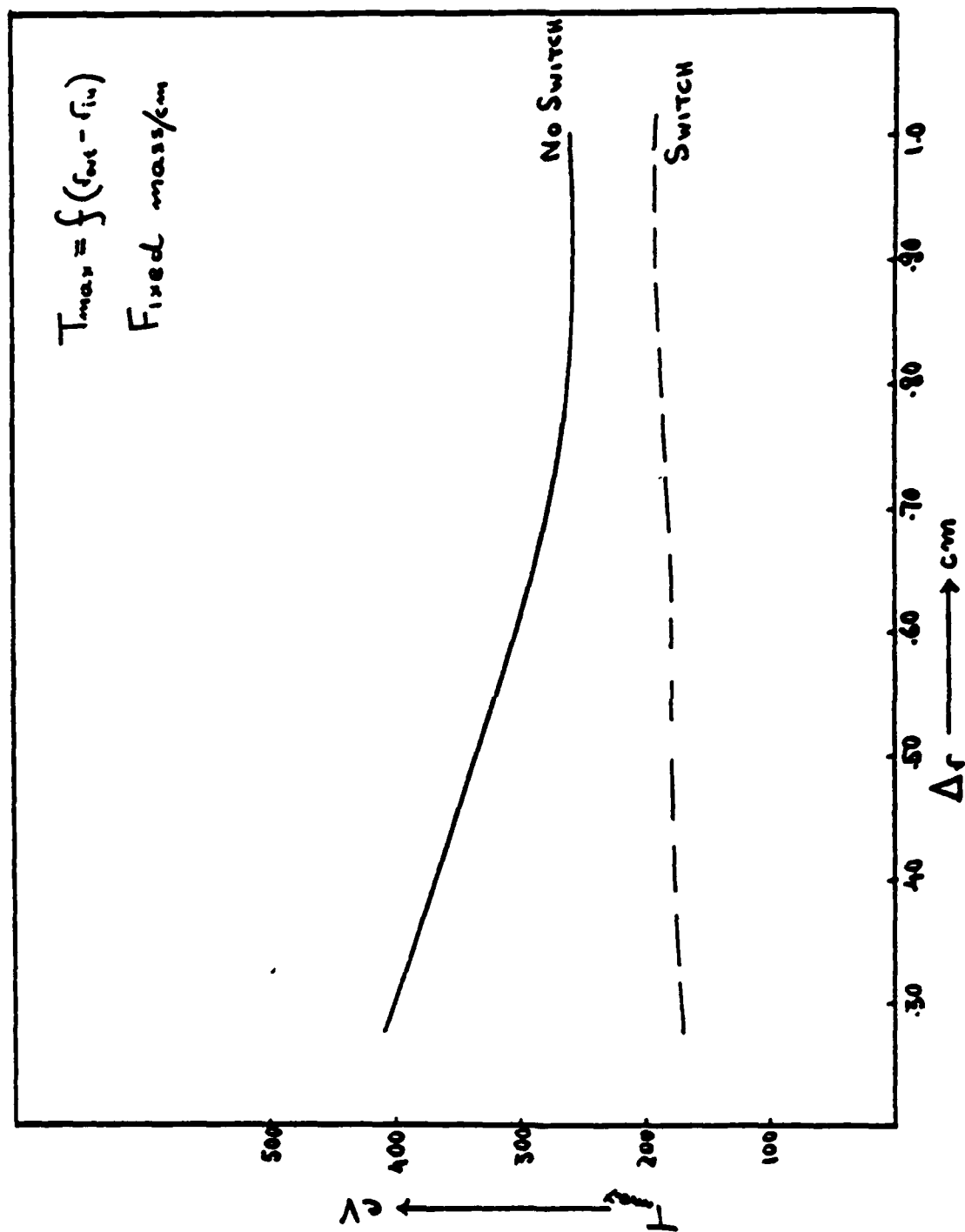


Fig. 13. Maximum temperature as a function of shell thickness.

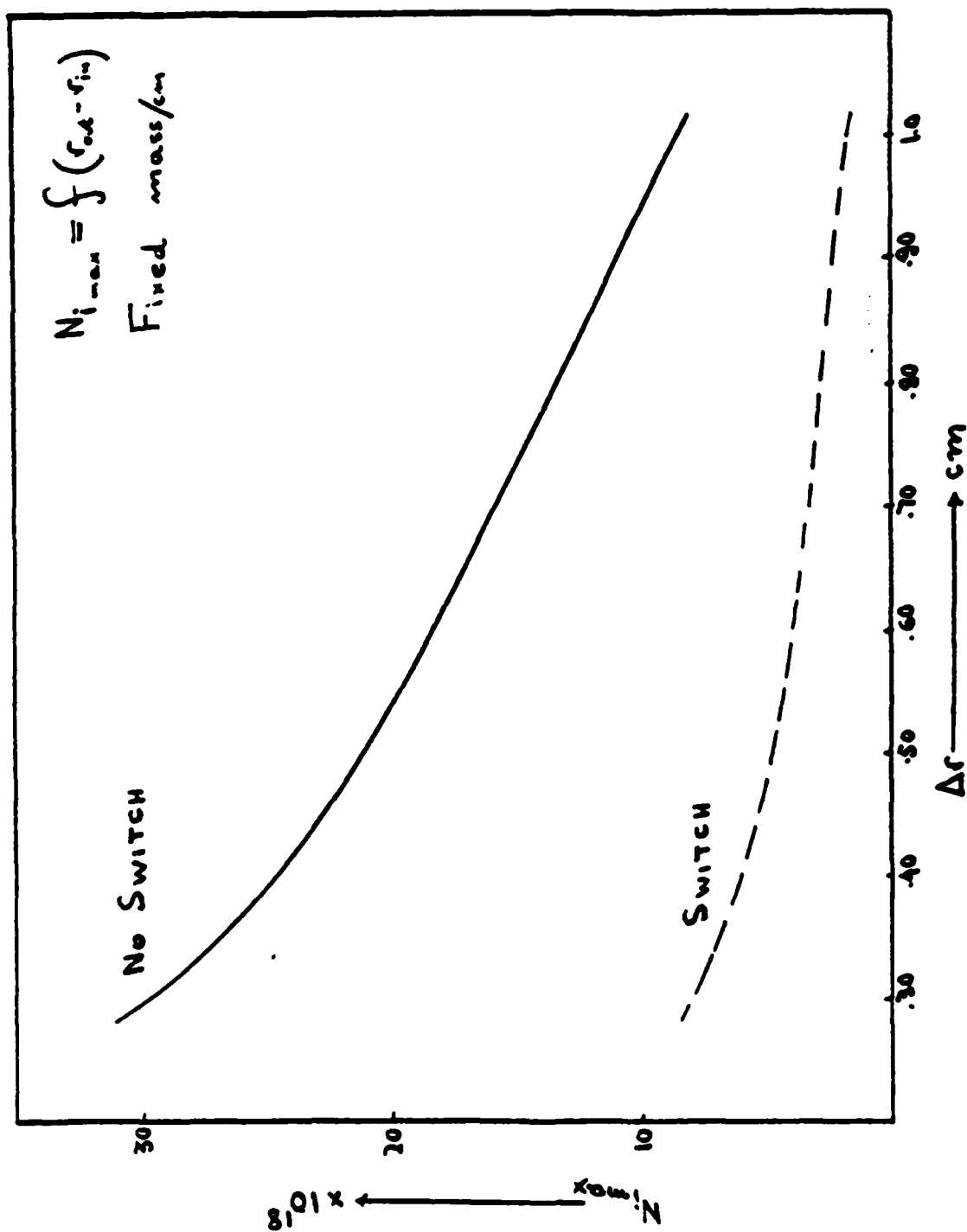


Fig. 14. Maximum ion density as a function of shell thickness.

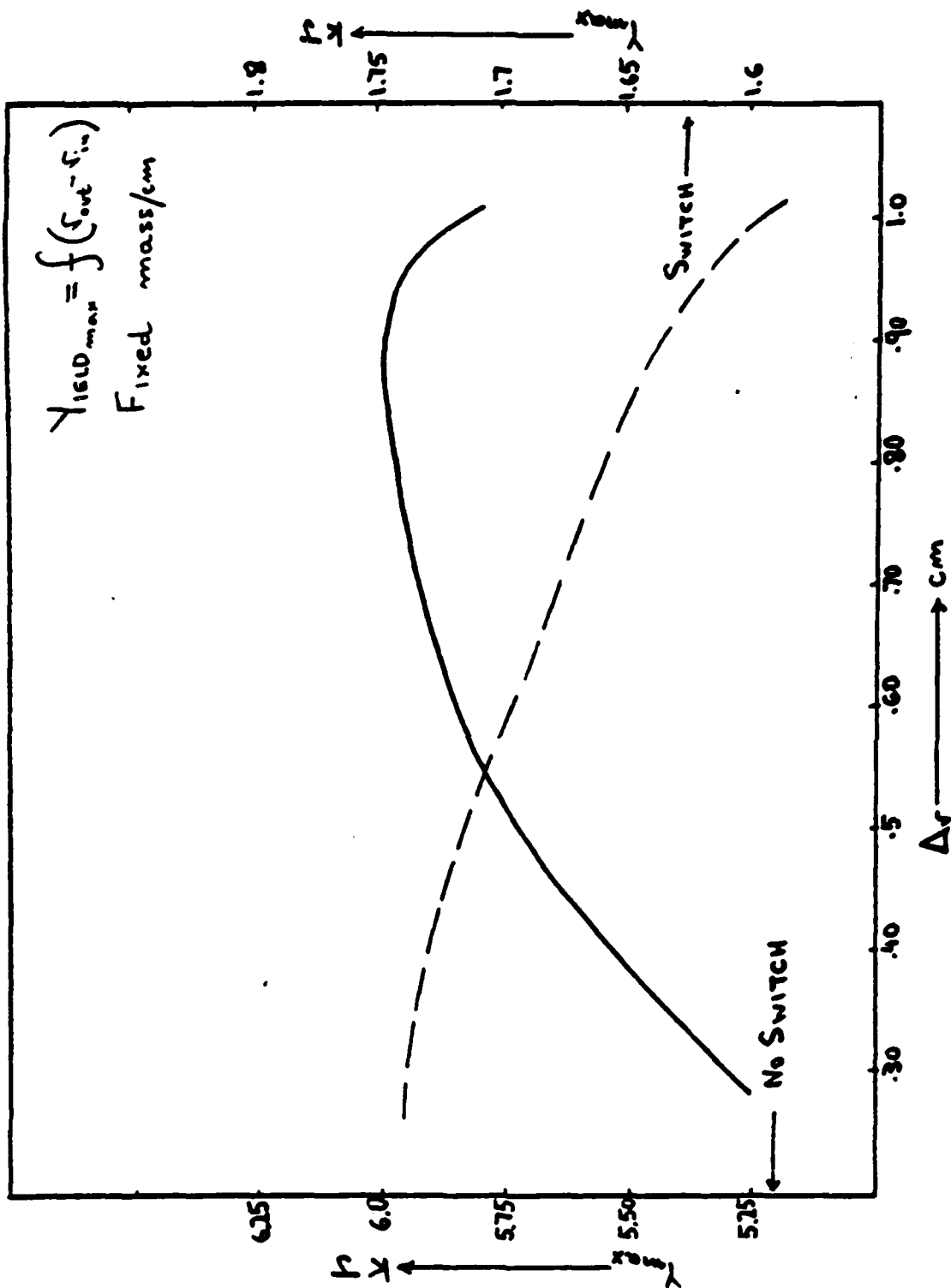


Fig. 15. Maximum yield as a function of shell thickness.

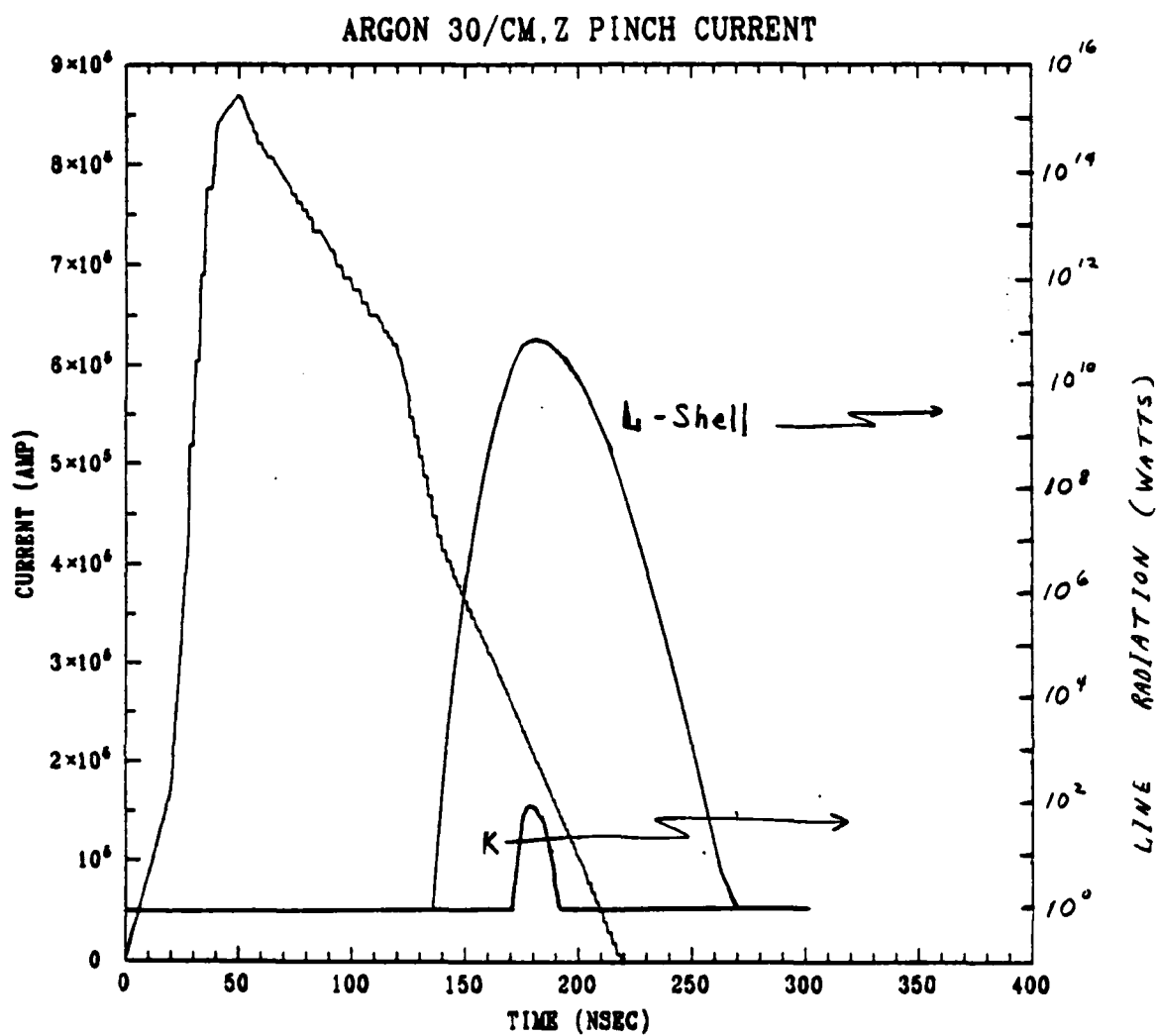


Fig. 16. PEOS current, L- and K-shell yields as a function of time.

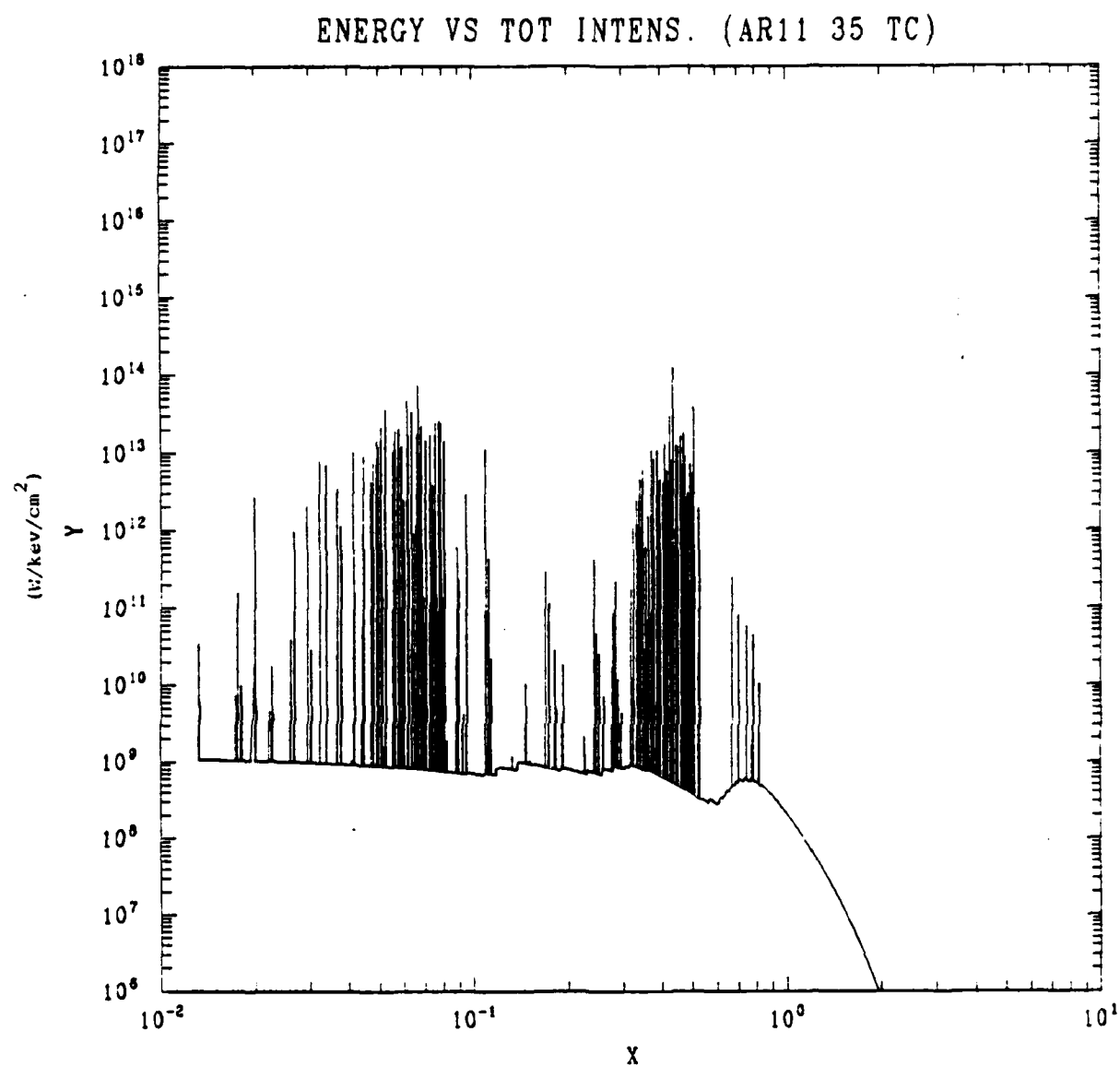


Fig. 17. Emission Spectra as a function of energy.

C. PRISM: Plasma Radiation Implosion Source Model

I. STAGNATING ARGON PLASMAS

One of the problems of interest is that of a stagnating plasma in which a puff gas implodes onto a dense core or post plasma. These configurations allow for a relatively uniform implosion along the axis. A stagnating plasma also allows one to control in a crude manner the yield characteristics of the implosion. That is, if one compares implosions in which a post is present and implosions in which only a background gas is present, more L-shell radiation occurs when a post is present. Similarly, provided the implosion velocity is low enough, more K-shell radiation occurs when there is no post. Although, the goal of the PRS program is to maximize the harder K-shell radiation, some applications may require outputs in the L-shell. The concept of a post thus allows one more degree of flexibility in matching the machine and mass loading to the desired spectral output.

In the process of stagnation, the kinetic energy of the inflowing material is converted into internal energy. In turn, the internal energy is partitioned between ionization and thermal energy. Some of this energy is radiated away from the system or is carried to another portion of the plasma. A shock wave develops and propagates in the direction opposite to the inflowing material and defines the boundary between the region of hot dense stagnated matter from the region of the relatively cool, and less dense imploding matter. In the idealized case ($\gamma = 5/3$), the ratio of the densities is 16 for a cylindrical implosion. If a core plasma is present, some of the kinetic energy is taken up by the core which subsequently implodes and bounces off the center of the column at $r=0$. Depending on the conditions present, the core can interact with the imploding material after bouncing off the center axis before all of this material has become shocked.

Results for argon and neon stagnating plasmas have been obtained. The previous report presented the neon results.¹ In this report, we will briefly describe the argon results. The design which we have modeled contains some important simplifications. First, both the core (or "post") and the imploding puff are taken to be a single material. Second, an

idealized initialization is used in that a low density puff is initially given a uniform velocity and is allowed to drive into the post plasma which is at a much higher density. This is in lieu of a driving magnetic field. This approximation allows us to isolate the implosion physics from the physics of the particular machine which might be under consideration.

As in our previous work,¹ we have performed simulations with and without central posts. The post consists of an initially cold (0.02 eV) argon gas at a density of 5×10^{-3} gm/cm³ and a radius of 1 mm. The argon puff gas which implodes on the core has an initial density of 5×10^{-6} gm/cm³ and extends out to 1.5 cm. The puff gas starts with a uniform velocity across its width. Figure 1 shows an implosion with a core present and a puff gas velocity of 4×10^7 cm/sec. Four times are shown: 4 nsec, 10 nsec, 20 nsec, and 60 nsec. At 4 nsec, contact has been made and the leading edge of the puff gas has been heated to about 800 eV. At 10 nsec, the stagnating shock can be seen propagating outward with a density plateau developing at the interface. A shock can also be seen moving into the core plasma. Note that the scale for the radius is given in log₁₀ cm so that the core can be distinguished. By 20 nsec, the shock in the core is well developed while the outward propagating shock has almost emerged from the puff. At 60 nsec, the entire configuration is in the process of disassembling. thought not shown here, the shock in the core plasma rebounds off the center axis at about 30 nsec.

If we now examine the radiative yields for cases with and without central core plasmas at several velocities there are some interesting features which did not appear in our earlier work with neon. Because of the higher Z of argon we extended the velocity range out to 8×10^7 cm/sec. Our previous work on neon (Z = 10 as opposed to Z = 18 for argon) had only covered the range from 1×10^7 cm/sec to 3×10^7 cm/sec. The first feature which is different is the divergence of the total yield as velocity increases as shown in Fig. 2. At all velocities, the cases with a core plasma present (solid circles) showed a greater yield. The difference between the two cases is very much evident at 8×10^7 cm/sec. The line yield for the L-shell is shown in Fig. 3. Again, the divergence appears and in fact Fig. 3 very closely mimics Fig. 2. The strong turnover in the open points (no core plasma present), is due to burning through the L-shell ionization stages at velocities greater than 4×10^7 cm/sec. The K-line

yield is shown in Fig. 4. At the highest velocity, 8×10^7 cm/sec, the K-line yield has flattened out when a core is not present while it has increased dramatically when a core is present. This reflects the fact that with the absence of a core more of the kinetic energy of the puff gas is converted to thermal energy with the result that even the He-like ionization stage is being burned through.

The results for argon at these higher velocities show that there can be substantial differences in the total radiative output when a post is present. This is a different result than that which was obtained from neon implosions initiated with velocities in the $1 - 3 \times 10^7$ cm/sec range. At puff gas velocities greater than 4×10^7 cm/sec, the yields with a post present are significantly larger for the K-shell yield as well as for the total and L-shell yields.

References

1. R. W. Clark, J. Davis, F. L. Cochran, Phys. Fluids, to be published.

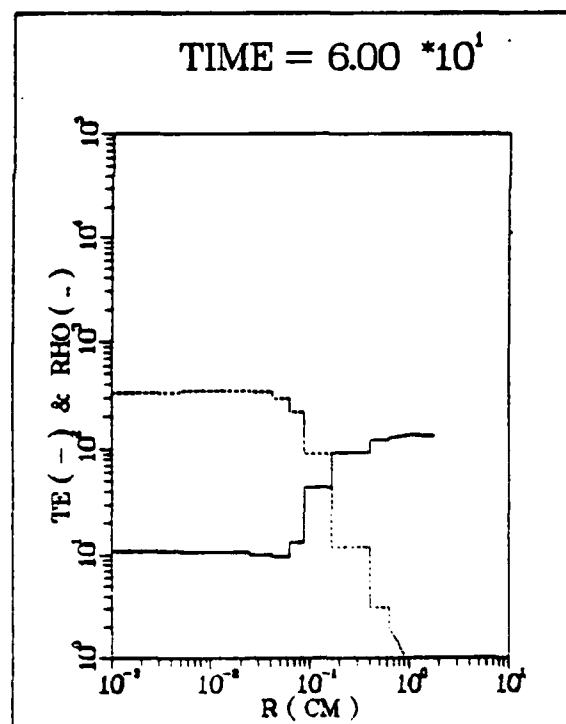
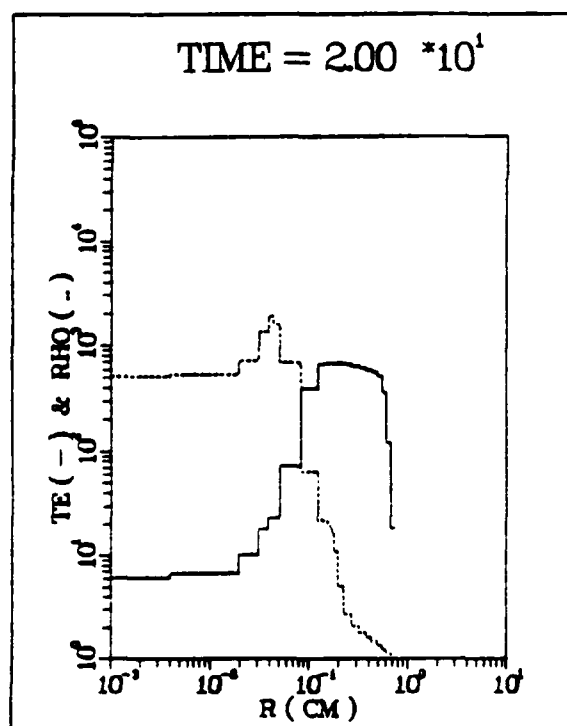
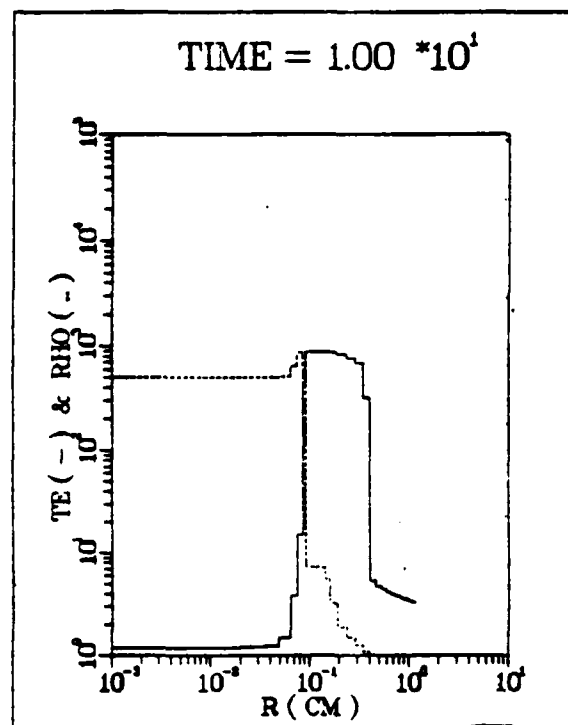
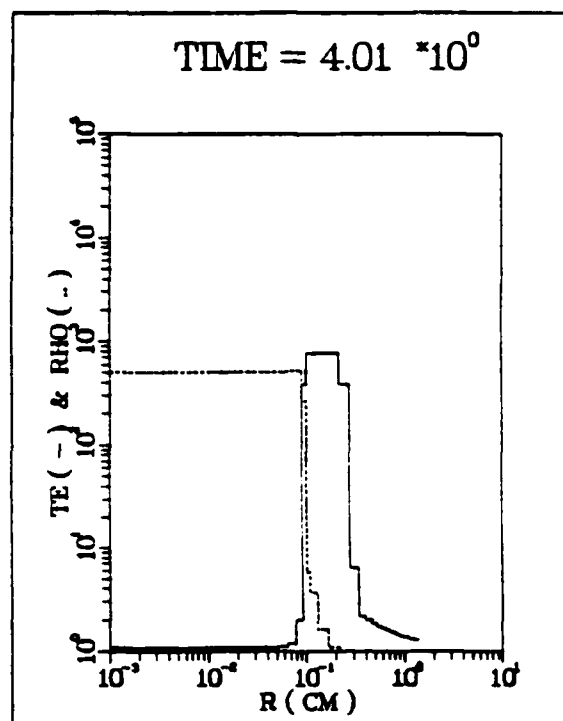


Figure 1 - Density and temperature profiles for an implosion in which a core is present and an initial puff gas velocity of 4×10^7 cm/sec. The densities are multiplied by a factor of 10^5 gm/cm³ and the temperatures are in eV. Four times are shown: 4 nsec, 10 nsec, 20 nsec, and 60 nsec.

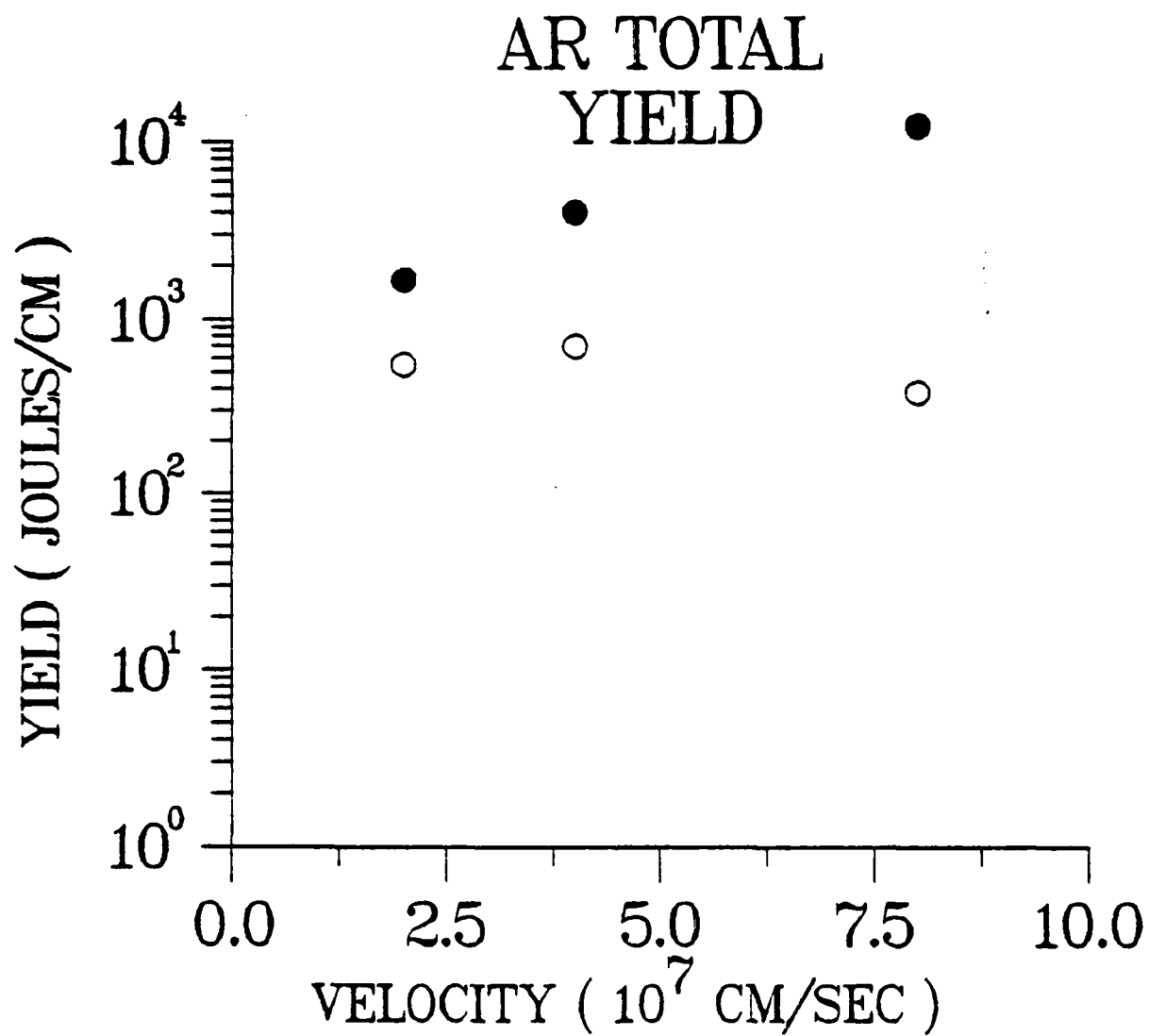


Figure 2 - Total radiation yield for the argon implosions as a function of initial velocity. Closed circles represent cases where a core is present and open circles represent cases where there is no core.

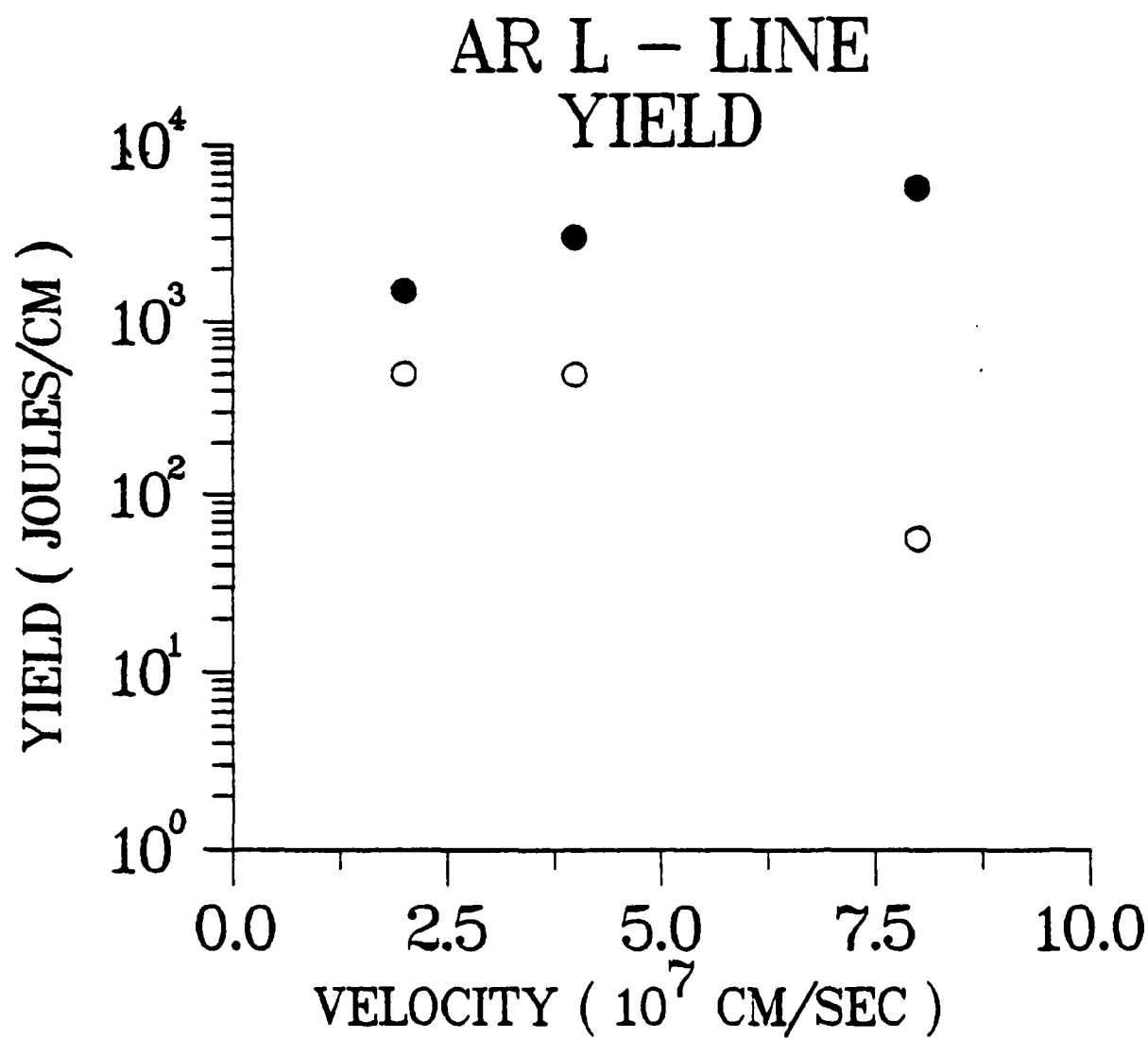


Figure 3 - L-shell line yield for various velocities.

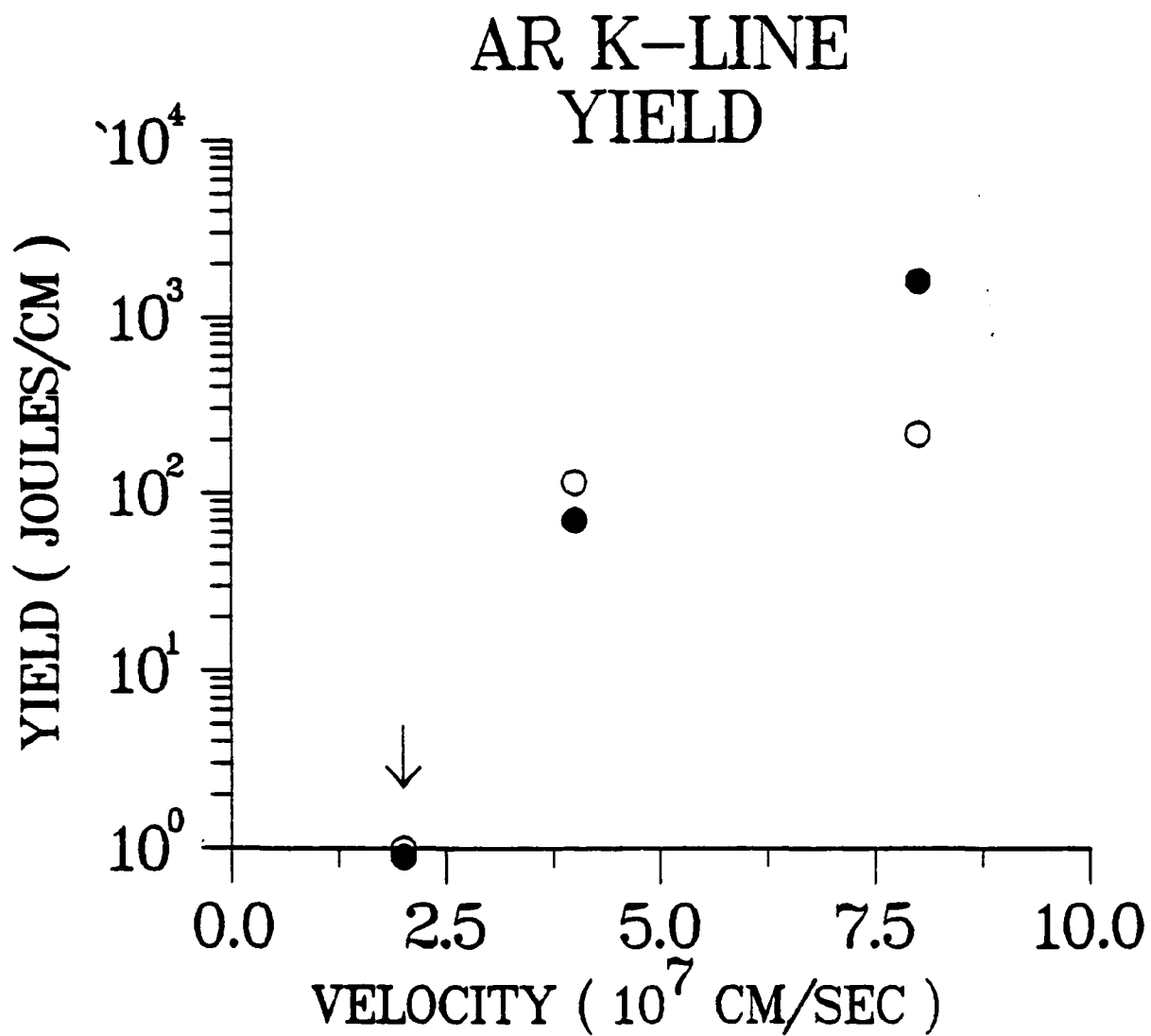


Figure 4 - K-shell line yield for various velocities. The arrow indicates the values at 2×10^7 cm/sec are below 1 Joule/cm.

D. Multimaterial Radiation-Hydrodynamic Modeling

A fully self-consistent multimaterial radiation hydrodynamic model has been developed for application to problems of interest to DNA. It features detailed non-LTE ionization dynamics and radiation transport using a probabilistic formalism. An arbitrary number of materials can be treated in full generality - as a mixture, as discrete shells, or as a combination of these. A multi-material puff-gas implosion calculation will be described, involving an argon puff-gas incident upon a neon core plasma.

I. INTRODUCTION

A number of recent DNA pulsed-power experiments have made use of mixtures or layered configurations consisting of multiple materials. For example, experiments have been performed involving annular puff gases imploding onto dissimilar axial puff gases or low density plasma cores. In addition, a number of interesting x-ray laser schemes propose to use photons from a strong transition in one element to create a population inversion in another. There are many important applications where a general multimaterial radiation hydrodynamic algorithm is necessary. For this reason, the DRACHMA code (detailed-configuration radiation-transport and coupled hydrodynamics multimaterial-mixture algorithm) has been developed.

As a test of the multimaterial algorithm, and to demonstrate its capabilities, a simulation of an annular argon puff-gas imploding onto a central neon core plasma was performed. Sandia National Laboratory has carried out a program involving puff-gas implosions onto low density foams to determine the feasibility of creating a homogeneous, uniform gain medium along the central core axis. Preliminary experimental results indicate high radiative conversion efficiencies from relatively uniform reproducible implosions. The geometry of the simulation corresponds to the Sandia experiments, but the materials chosen do not. They were chosen for convenience and for ease of comparison with existing single material calculations.

II. THEORETICAL MODEL

Since the implosion of a cylindrical puff-gas plasma can result in a substantial fraction of the total plasma energy being radiated away, the hydrodynamic evolution of the plasma may be appreciably altered. The interaction of the plasma dynamics, the atomic physics of the plasma components and the transport of radiation is both nonlinear and nonlocal and must be calculated self-consistently.

Discussion of the theoretical model will be separated for convenience as follows: (a) hydrodynamics and thermal conduction (b) ionization and atomic physics and (c) radiation emission and transport.

(a) Hydrodynamics and Thermal Conduction

The basic hydrodynamic variables of total mass, momentum, and total energy are transported in one dimension using a numerical scheme with a sliding-zone version of flux-corrected transport. A special gridding algorithm is employed which moves zones in a Lagrangian fashion and adjusts the mesh in order to resolve steep gradients in the flow. The hydrodynamic equations solved are

$$\frac{D\rho}{Dt} = \frac{\partial \rho}{\partial t} + \nabla \cdot (\rho u) = 0 \quad (1)$$

$$\frac{D\rho u}{Dt} = - \nabla P \quad (2)$$

$$\frac{DE}{Dt} = - \nabla \cdot (Pu) + \dot{E}_{\text{rad}} + \nabla \cdot (KVT) \quad (3)$$

where ρ is the mass density summed over species,

$$\rho = \sum_s N_s m_s \quad (4)$$

with N_s the number density of species s and m_s the associated mass, u is velocity, P is pressure, E is total energy density, \dot{E}_{rad} is the rate of

energy loss or gain due to radiation, and K is the thermal conductivity. The thermal conduction is calculated implicitly, using an iterative Crank-Nicholson scheme.

Since density did not exceed solid density in this problem, a simple equation of state was assumed,

$$P = 2/3 (E - 1/2 \rho u^2 - E_{ion}) \quad (5)$$

where E_{ion} is the potential energy due to ionization and excitation, summed over species. A single temperature model was employed.

$$kT = P / (N_e + \sum_s N_s) \quad (6)$$

where T is temperature. E_{ion} and N_e , the electron number density, are calculated from the ionization-radiation equations which are described below. A single temperature approximation is valid in the core plasma, where the equilibrium time is of the order of picoseconds, and it is adequate in the stagnation region, where the equilibration time can be of the order of nanoseconds. In the blowoff plasma, it is a marginal approximation, but the consequences are minor since little radiation is emitted from this region, and most of the energy is carried by the electrons in the blowoff.

The local rate of change of energy due to radiation transport, \dot{E}_{rad} , will be discussed below.

(b) Ionization and Atomic Physics

The ionic populations in the plasma are determined by a set of atomic rate equations of the form

$$\frac{df_{is}}{dt} = \sum_j W_{jis} f_{js} - \sum_j W_{ijs} f_{is} \quad (7)$$

where f_{is} is the fractional population of atomic level i for the plasma species s . W_{jis} is the net reaction rate describing the transition from

initial state j to final state i . An equation of this type is constructed for each of the levels included in the model for each of the atomic species.

For sufficiently dense plasmas, the effective populating and depopulating rates are sufficiently fast compared with the hydrodynamic timescales that an equilibrium assumption can be justified, which involves dropping the explicit time dependence in Eq. (7). The plasma is then said to be in collisional-radiative equilibrium (CRE), whereby the plasma ionization state responds instantaneously to changes in hydrodynamic quantities.

The rate coefficients which are used to calculate the populating and depopulating rates, W_{jis} , are calculated using various atomic calculational methods. The processes included and the methods employed in generating the corresponding rate coefficients are summarized elsewhere.

Once the set of rate equations, including the optical pumping from the radiation field, has been solved for the level populations, f_{is} , the electron density can be calculated,

$$N_e = \sum_s N_s \sum_i f_{is} z_{is} \quad (8)$$

where z_{is} is the ionic charge of level i for species s , and N_s is the total ion density of species s .

The ionization and excitation energy can also be calculated by

$$E_{ion} = \sum_s N_s \sum_i f_{is} x_{is} \quad (9)$$

where x_{is} is the energy of level i , measured from the ground state of the neutral atom of species s .

For the simulation described below, the atomic model for neon contains 27 atomic levels and 13 emissions lines, and the model for argon contains 31 atomic levels and 11 emission lines.

(c) Radiation Emission and Transport

Radiation emission from and absorption by a plasma are dependent on the local atomic level population densities. Except for optically thin plasmas, however, the level populations depend on the radiation field, since optical pumping via photoionization and photoexcitation can produce significant population redistribution. Thus, the ionization and radiative processes are strongly coupled and must be solved self-consistently. In this model, an iterative procedure is used, where level populations for each material are calculated using the radiation field from the previous iteration, then using these populations to calculate a new radiation field and recalculating populations until convergence is achieved.

A probabilistic radiation transport scheme is employed, which forms local angle and frequency averaged escape probabilities for each emission line and for each bound-free process. This amounts to characterizing each emission line and each bound-free process by a frequency at which the probability of escape is maximized for the greatest number of photons, since a decrease in opacity away from the line center or the edge frequency can be accompanied by a corresponding decrease in emissivity. Free-free radiation is treated with a multifrequency transport formalism. The radiation transport and emission spectra are calculated from these escape probabilities. The method can treat comprehensive atomic models and provides good overall energetics, but cannot calculate accurately certain spectral details and lines with very high optical depths.

Inner-shell opacities are included in the model, since these processes are very important in cool, dense plasma regions. Inner-shell photoionization cross sections for each of the neutral elements are taken from the fits of Biggs and Lighthill, and the positions of the ionization-dependent absorption edges are taken from the Hartree-Fock calculations of Clementi and Roetti.

The local rate of change of energy in zone j , due to radiation transport is given by

$$\dot{\epsilon}_{\text{rad } j} = - \sum_s \sum_{p(s)} (F_{pjs} - \sum_k C_{pkjs} F_{pks}) \quad (10)$$

where F_{pks} is the rate of energy loss in zone k due to a discrete radiative process (or frequency group) p for species s , and C_{pkjs} is the radiative coupling of zone k to zone j for that process. The couplings are functions of opacity, integrated over process and photon path. In the probabilistic model, a matrix of couplings must be computed for each bound-bound, bound-free and free-free process. In this way, the net cooling and heating by radiation emission and absorption between the various zones of the plasma is accurately taken into account.

III. RESULTS

A simulation was performed for a cylindrical annular argon puff-gas of density 5×10^{-6} g/cm, with inner radius 0.55 cm and outer radius 1.95 cm, imploding radially at a velocity of 5×10^7 cm/sec onto a central neon core plasma of density 5×10^{-3} g/cm and radius 0.10 cm. The initial configuration is shown in Fig. 1. The temperature of the puff-gas was taken to be about 2.5 eV initially, and a tenuous background argon plasma was placed between the puff-gas and core plasmas of density 5×10^{-7} g/cm.

These initial conditions were chosen to correspond approximately to simulations conducted with a neon puff-gas stagnating on a neon core plasma, described in an earlier report; however, the implosion velocity has been increased in order to produce some K-shell argon radiation.

For the first 10 nanoseconds, the argon puff-gas essentially coasts radially inward. The forward edge of the puff-gas is heated to about 100 eV through accretion of the background plasma. At about 10 nanoseconds (Fig. 2), the puff-gas makes full contact with the core, and conversion of kinetic energy to thermal energy begins to build an overpressure at the interface.

By 19.4 nanoseconds (Fig. 3) the peak temperature near the interface is approaching a keV, and a narrow annulus of intense net radiative emission centered at the contact region is formed. The emission spectrum at this time is shown in Fig. 4. It is dominated by neon and argon L-shell radiation at this time, and the emission falls off rapidly above 1 keV. The individual contributions of the argon and neon components to the total emission spectrum can be seen in Figs. 5 and 6, respectively. In Fig. 5, the argon spectrum is plotted together with the total free-free

radiation. The total argon emission is substantially larger than the neon emission, shown in Fig. 6, since the bulk of the core plasma is still very cold. Optical depth through the plasma is plotted as a function of photon energy in Fig. 7. At 19.4 nanoseconds, inner-shell opacity is the major component, and since most of the plasma is still relatively cool, inner-shell optical depths have not dropped substantially from cold-target values except at low energies. The neon cold-target L-shell and K-shell absorption edges occur at 0.018 keV and 0.867 keV, whereas the corresponding argon L- and K-shell edges occur at 0.245 and 3.203 keV, respectively.

By 19.4 nanoseconds, the overpressure at the interface has caused shocks to propagate radially inward in the core and outward in the puff-gas. Heating from the soft x-rays produced in the interface region is evident in the dense core, and radiation heating is warming the puff-gas. Thermal conduction is ineffective in transporting energy into the core plasma.

The inward propagating shock reaches the origin at about 31 nanoseconds. Plasma profiles at this time are shown in Fig. 8. Although the neon plasma approaches solid density on axis, the temperature there is still only about 50 eV. This region of very dense plasma radiates strongly in the L-shell, but its volume is small. A broader annulus of hot plasma situated outside the core plasma is producing most of the radiation. This can be seen from the emission spectrum at this time, shown in Fig. 9, where argon L-shell radiation still dominates.

Optical depths are plotted as a function of photon energy for this time in Fig. 10. The neon inner-shell optical depths are characteristic of a strong temperature gradient, resulting in an array of ionization states. The ionization-shifted L-shell absorption edges of neon are seen as a series of steps below about 200 eV. The increase in optical depth above the shifted L-shell edge of neon is due to the compression of the core.

At 60 nanoseconds (Fig. 11), the entire plasma is moving radially outwards. The temperature of the neon core plasma has fallen to about 20 eV, and the argon puff-gas has cooled to about 120 eV.

The energy history of the plasma throughout the first 110 nanoseconds is shown in Fig. 12. Initially, about 98% of the total energy is kinetic;

the remainder is in thermal and ionization energies. The energy lost to radiation begins to increase sharply at about 12 nanoseconds, as the argon puff-gas comes into contact with the neon core. Thermal and ionization energies also begin to climb at this time. Kinetic energy goes through a well defined minimum at about 38 nanoseconds, at which time more than half of the total plasma energy has been radiated away. By 110 nanoseconds, more than 70% of the total energy has been converted to radiation.

IV. CONCLUSIONS

Puff-gas implosions show promise as a means of efficiently converting kinetic energy to radiation. With a central stagnation core plasma, higher plasma densities and total radiative yields can be achieved.

This simulation served as a testbed for the DRACHMA multi-material code, it accurately calculated the generation and transport of radiation in a multi-species environment, including a detailed accounting of continuum and inner-shell opacities.

Since radiation plays such a crucial role, it must be generated and transported accurately. As we have shown previously, optically thin radiation ignores the importance of transport of radiative energy and grossly overestimates losses. LTE or corona equilibrium models for the level populations will also lead to inaccurate energetics. Finally, because the radiative energy loss and the transport of energy in the plasma substantially modify the hydrodynamic response, a self-consistent calculation, linking radiation and fluid transport with the ionization dynamics, must be performed.

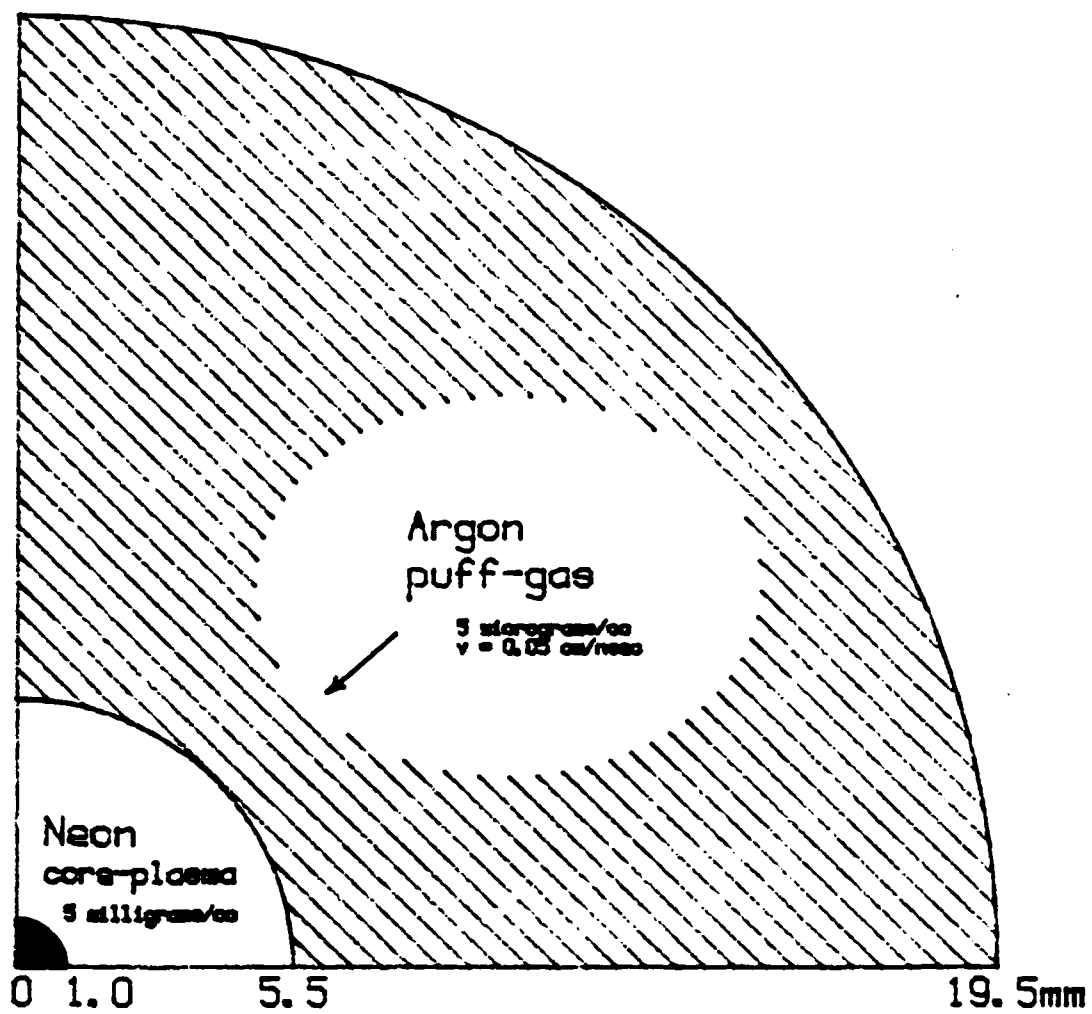


Figure 1

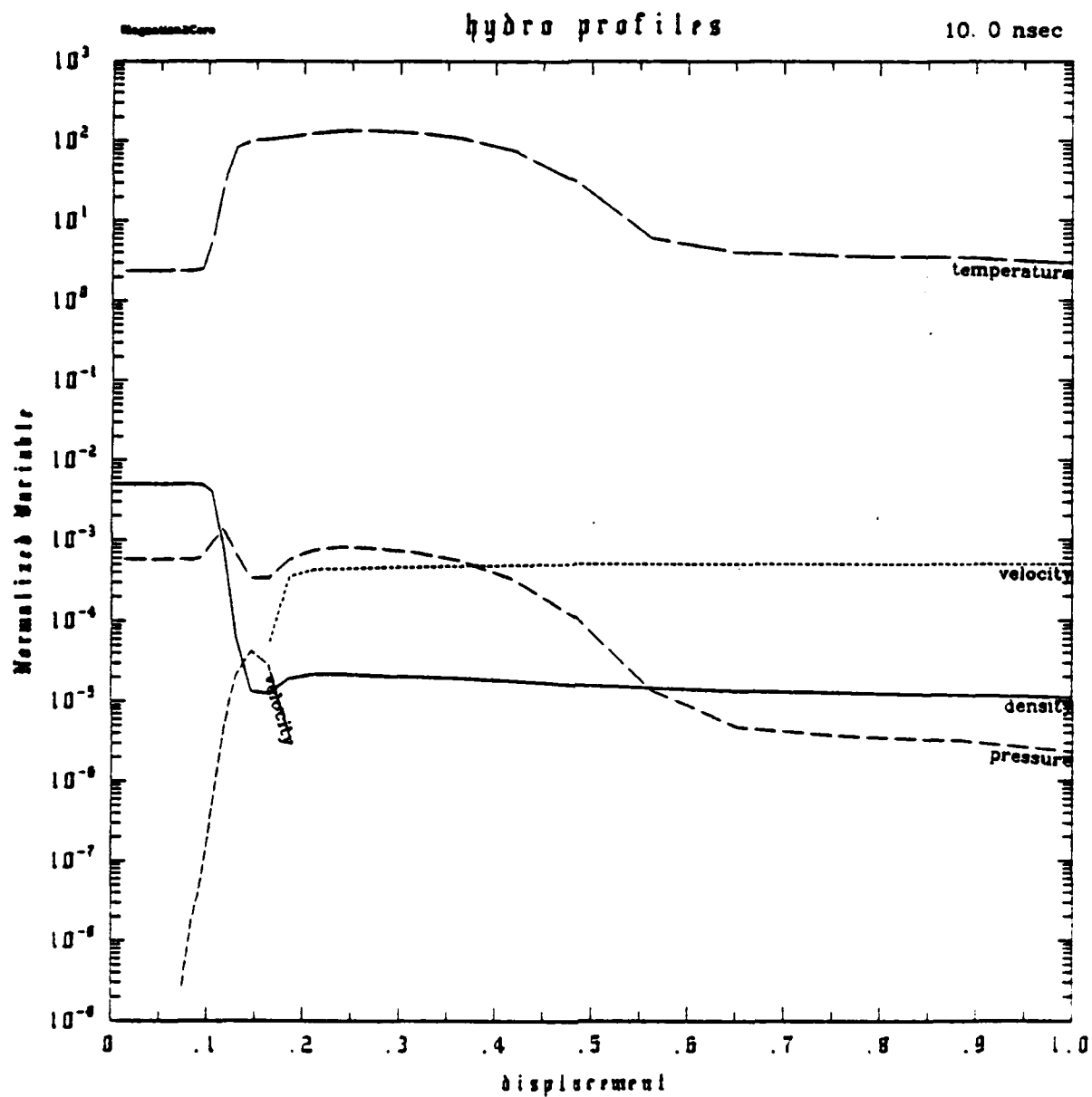


Figure 2

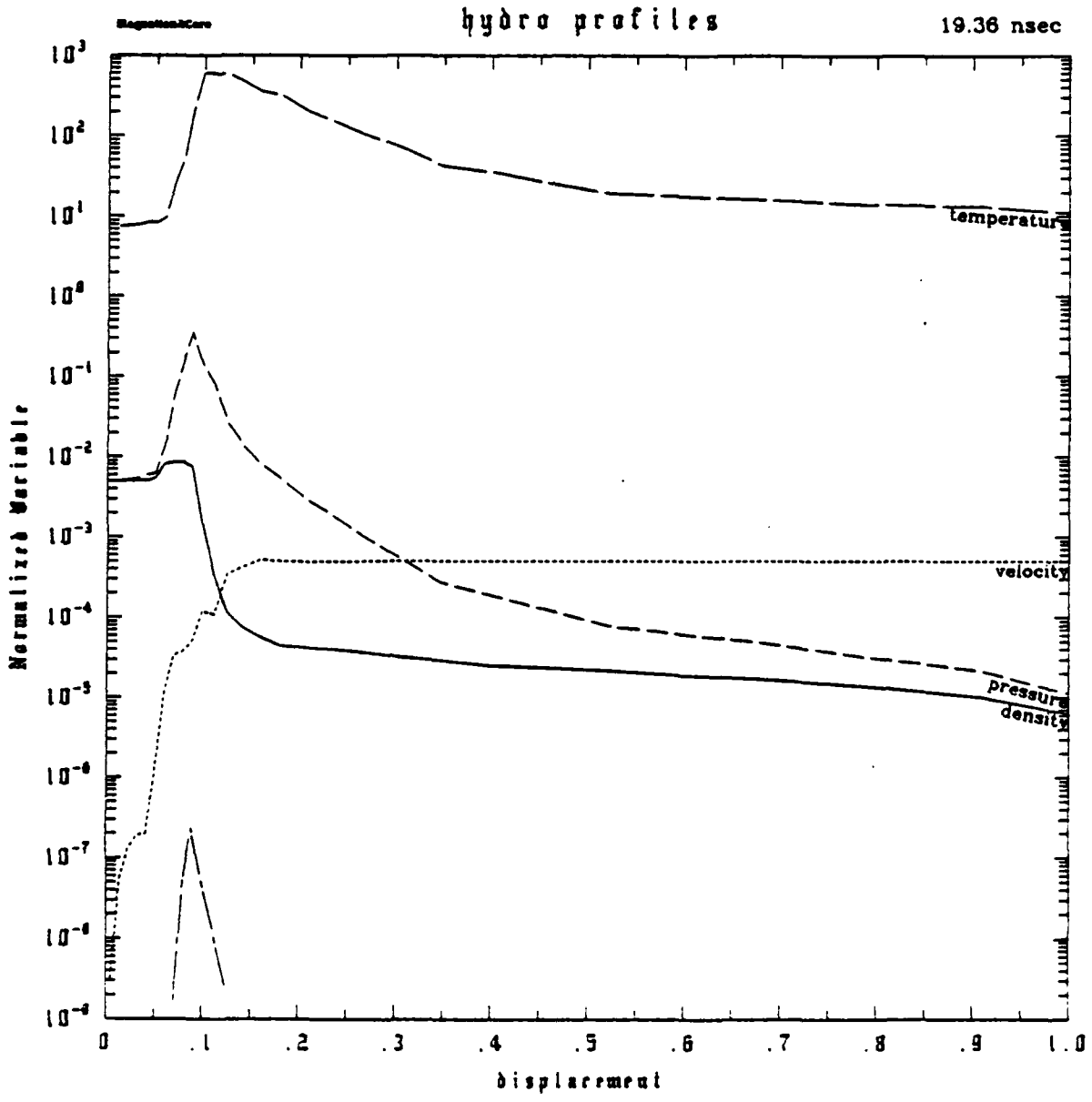


Figure 3

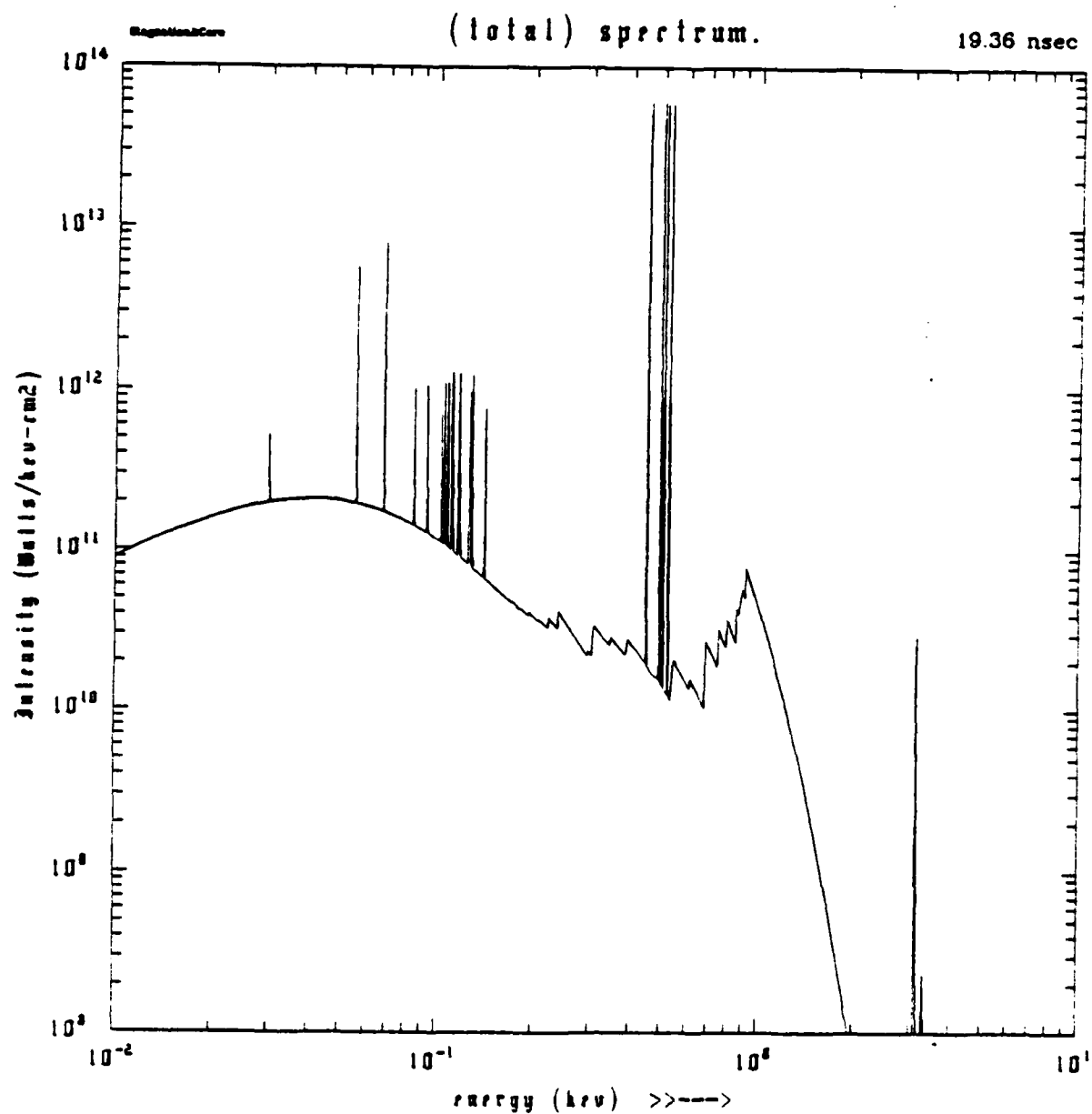


Figure 4

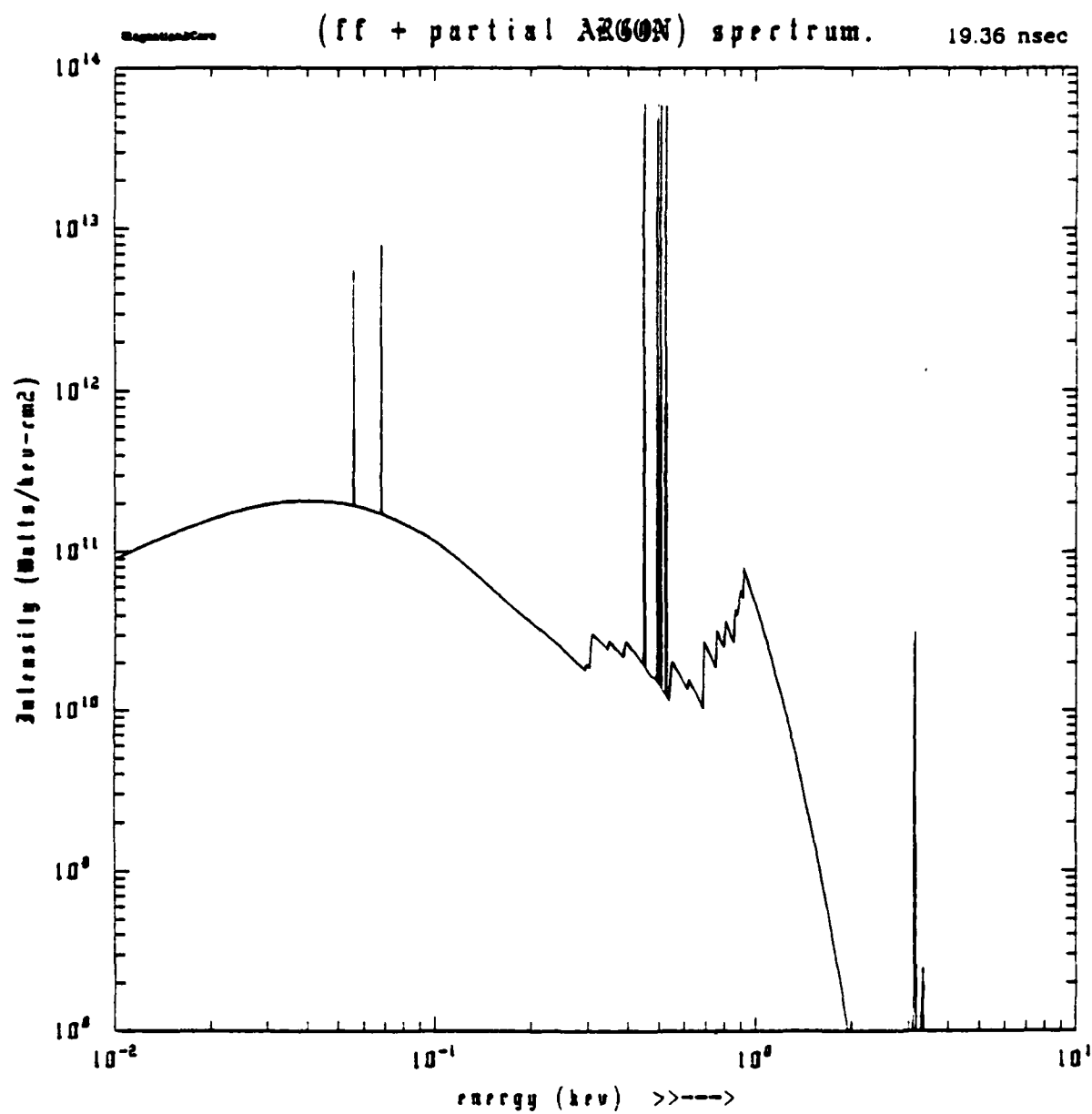


Figure 5

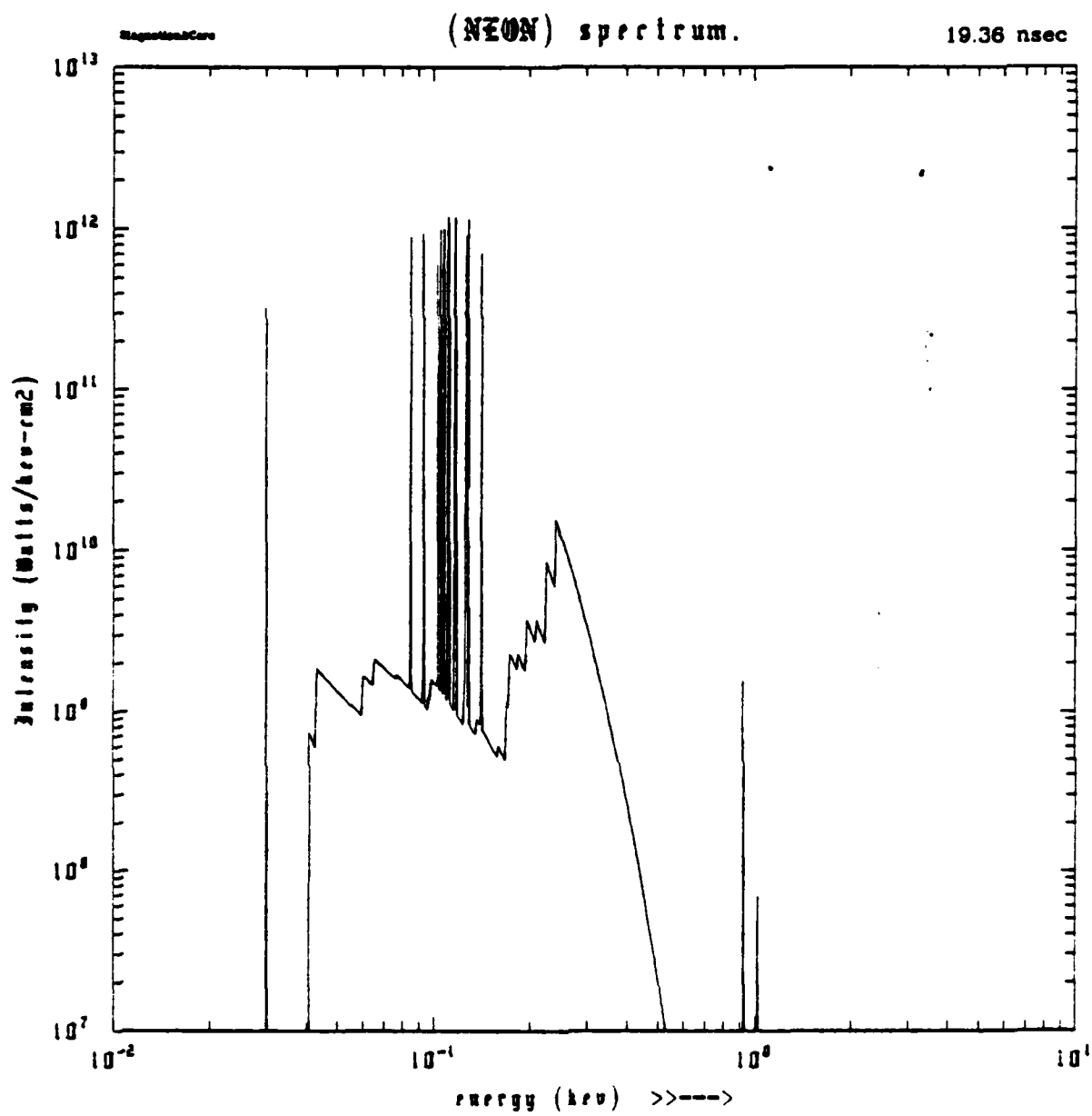


Figure 6

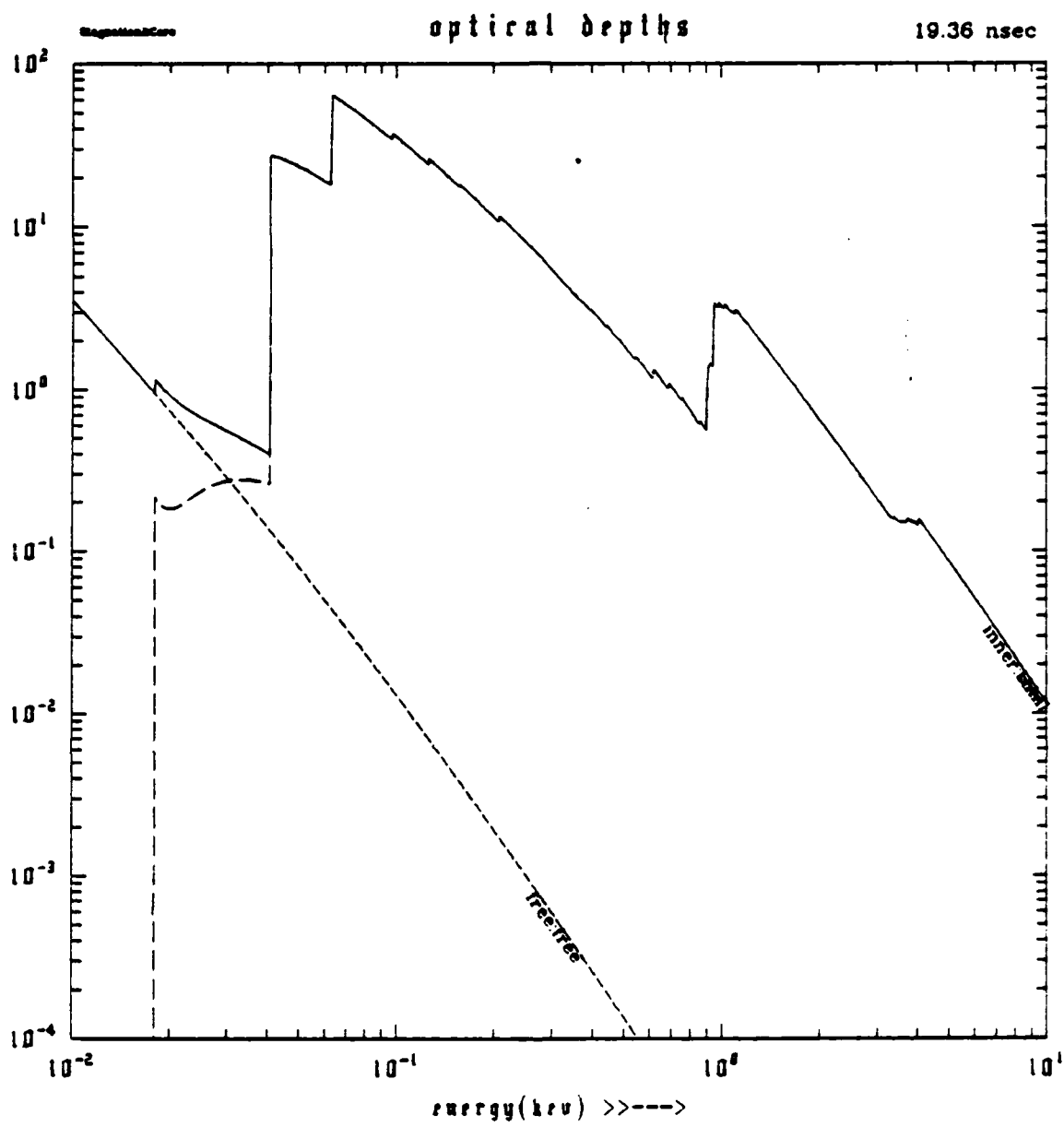


Figure 7

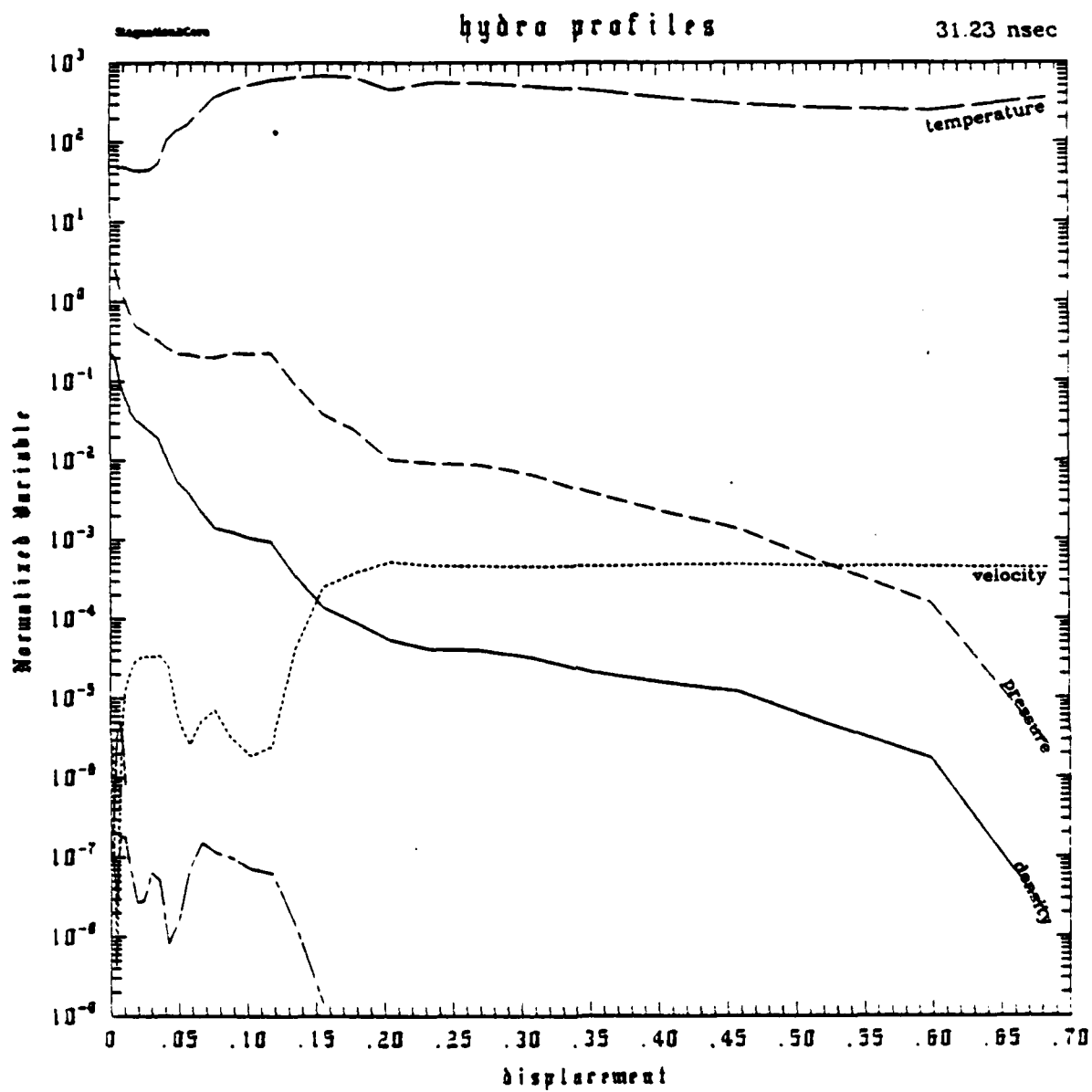


Figure 8

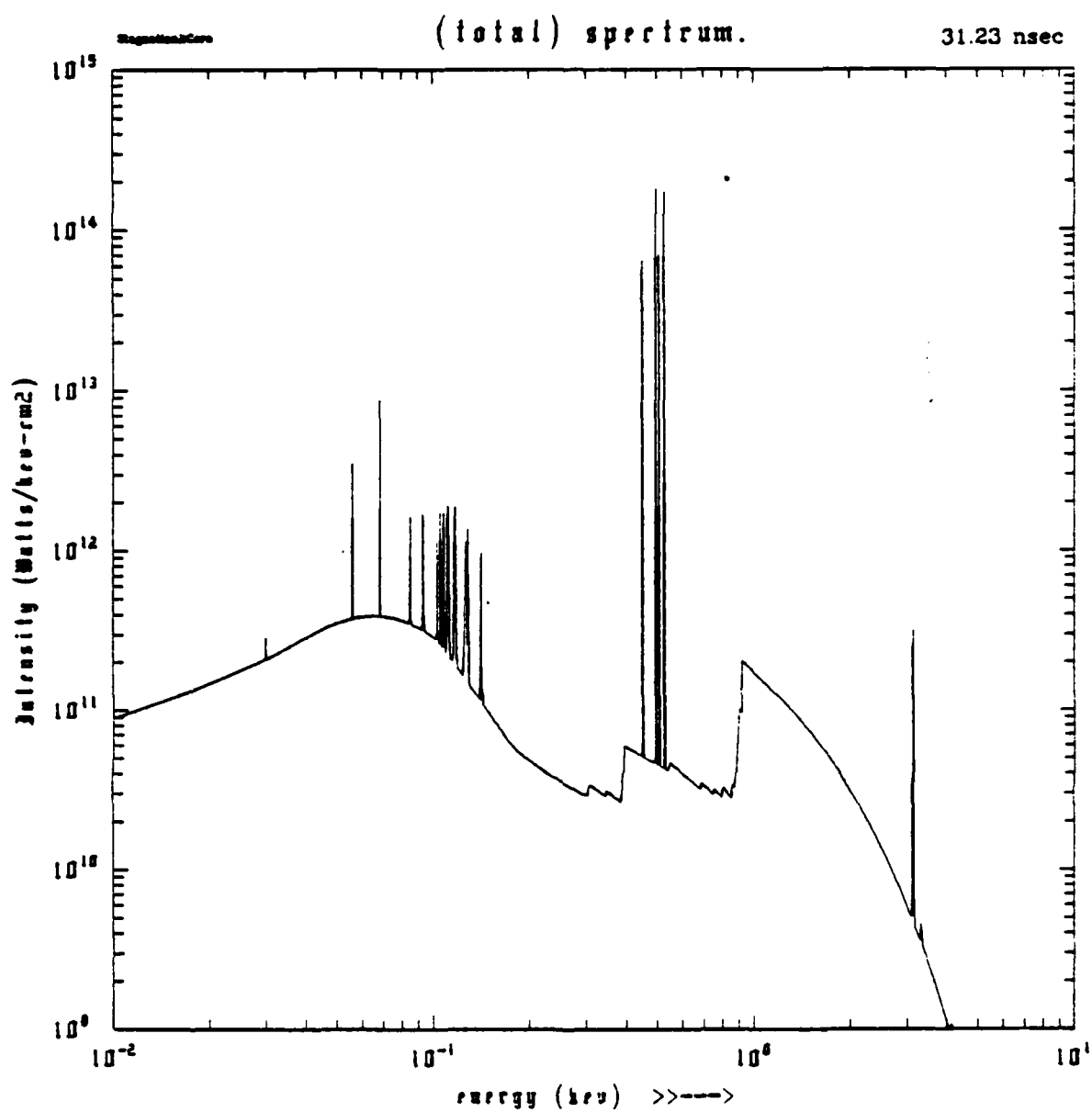


Figure 9

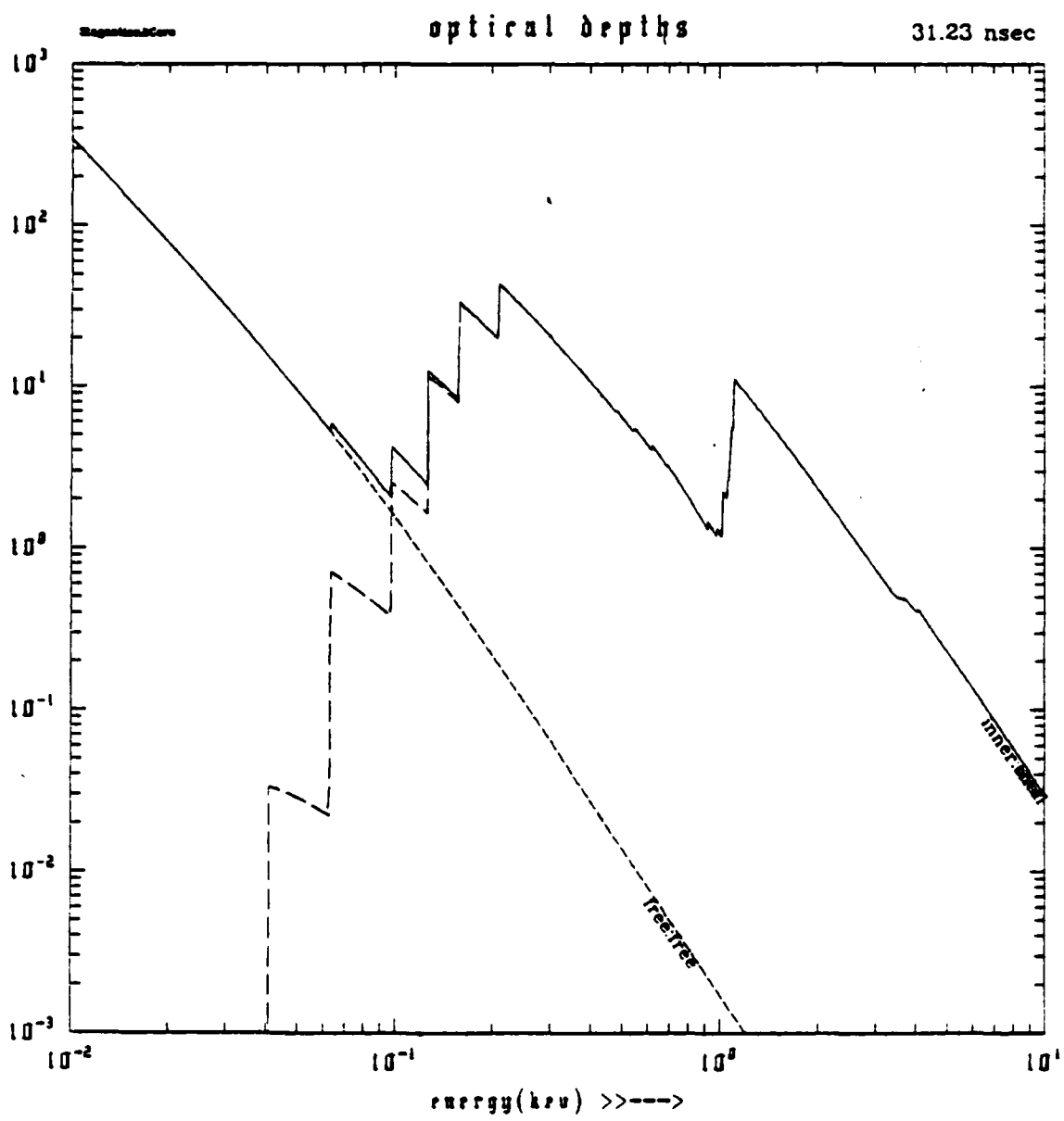


Figure 10

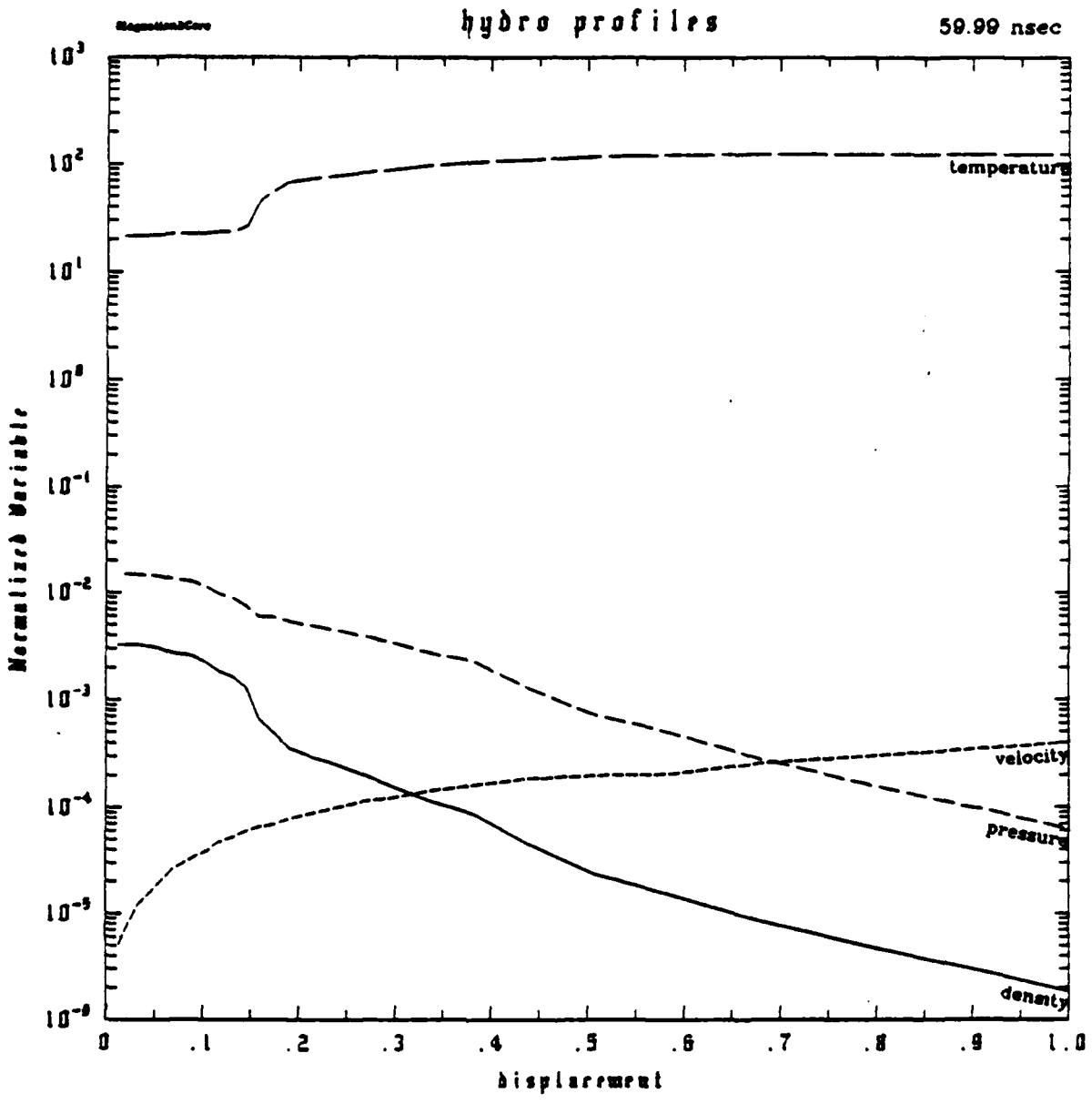


Figure 11

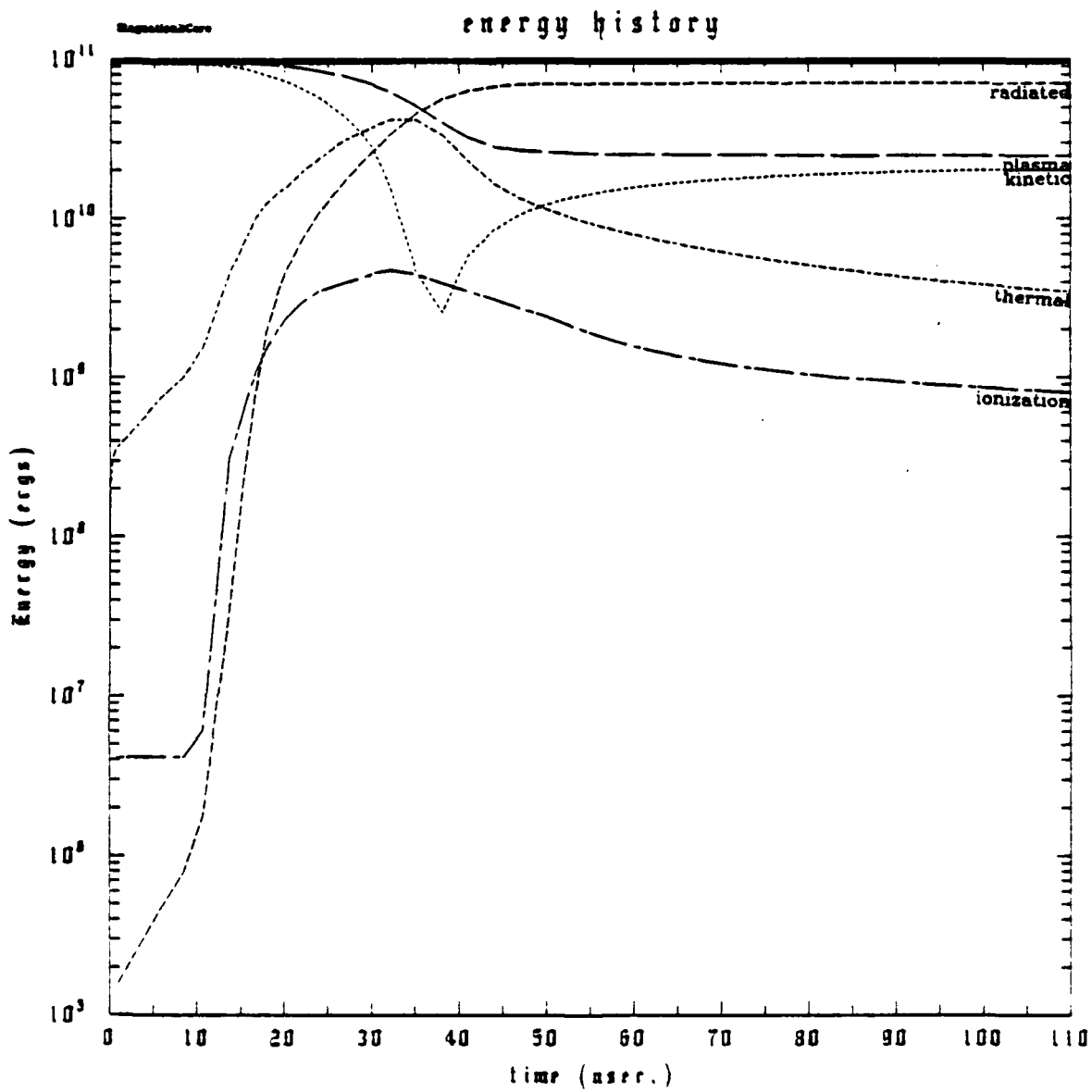


Figure 12

E. GYROKINETIC PLASMA RADIATION SOURCE CORONA MODEL

I. Corona Plasma Phenomenology

Because pure magnetohydrodynamic models generally predict faster, denser Z-pinch implosions than one observes in pulse power diodes, a common corrective hypothesis has been one form or another of "anomalous resistivity". In early NRL models^{1,2} of the plasma radiation source (PRS), an exterior plasma domain characterized by thin density and high temperature was invoked as a mechanism for softening the pinch by providing an alternate current path. By carrying a drift speed limited current density and being too tenuous to lose heat through radiation, such a plasma could perhaps absorb a modest fraction of the diode current and thus rob the interior, denser load plasma of its driving force, the "magnetic piston". If so the limitations of "pure" MHD models could be understood from a more fundamental viewpoint.

Such a simple model for "anomalous resistivity" proved severely limited. In its original form, the constraints of quasi-static pressure balance, rather than smooth radial acceleration, and a conventional Ohm's law, produced a corona of consistently small current and mass, relative to the main load. On the other hand, it is now apparent that a more general picture of the exterior plasma does provide a potentially significant current channel. The basis for this current lies in two phenomena -- the heating of tenuous gas by the first part of the electromagnetic driving pulse, and the magnetization of the resulting plasma by the interior current driving the main load mass.

A. Electron "Driftaway"

The details of early heating are at present unexplored in the PRS community. Such thin, hot plasmas as might occur in the exterior region are difficult to diagnose spectroscopically due to the large fluence of XUV and soft X-rays emitted by the denser portions of the load as it begins to absorb the electromagnetic pulse. Yet it is this very fact which makes reasonable the partial or perhaps complete photoionization of the tenuous load gas or "pump oil" surrounding the load. The tendency of magnetically insulated transmission line (MITL) systems to propagate poorly at background pressures much exceeding 10^{-4} torr substantiates this conjecture³. One can generally expect atomic densities in the range of 10^{15} to 10^{12} per cm^{-3} in the immediate exterior neighborhood of a PRS load. When this gas is partially ionized its radial flow velocity is initially small, any large axial E field such as that of the incoming driver pulse will force further ohmic heating, and possibly drive unstable microturbulence, which will make the medium even more resistive. This heating will proceed until the plasma can no longer absorb energy through collisions. Hence a reasonably credible production scenario⁴ for diffuse exterior plasma is:

i. Early ohmic heating of tenuous, partially photoionized load gas or "pump oil" drives the electron collision time above the PRS implosion timescale of [10 - 100] ns.

ii. Non-maxwellian distributions of electrons and some lighter ions decouple from the colder population and effectively drop the conductivity, further increasing the heating rate.

iii. Heating proceeds until an energy density is reached for which all the electrons are locked up in the non-maxwellian population.

iv. High energy electrons are continuously captured in $E \times B$ drift motions rather than axial runaway.

The details are accessible through a Fokker-Planck calculation, which is in development.

B. Tenuous Plasma Corona -- Gyrokinetic Currents and Drifts

Once the collisionless populations are "boiled off" of the background gas, the rising interior current carried by the diode load tends to prevent runaway in the usual sense. The magnetic field demands an ever more insulated state and some fraction of the tenuous gas will drift inward as a magnetized plasma. The magnetic insulation of this $E \times B$ plasma is not perfect, however, because work must be done on it to make the radial drift follow the boundary conditions imposed by the pulse power.

The power absorbed manifests itself in current density and E field attenuation, the "corona" therefore presents an energy sink between the pulse power source and the PRS load. Such magnetized drift current densities have three components when described by a "gyrokinetic" theory. The first arises in radially accelerating the guiding centers due to increases in E/B during the driver pulse. The second, from the azimuthal angular momentum associated with guiding center circulation around the diode axis. The third, from the "gyration" angular momentum about the guiding center, usually expressed

in terms of a magnetic moment. In moving the magnetized plasma toward the diode axis these conserved angular momenta force an increase in the particle speed with decreasing radius or increasing magnetic field. The work required to increase this speed comes from the energy in the electromagnetic driver.

The level of this power loss does not diminish as the plasma compresses (in fact the magnetization criteria improve near the origin). Moreover, the angular momentum conservation in the tenuous region would require an infinite amount of energy to get the magnetized plasma to the origin. Later in time, only the onset of collisionality, or the relaxation of the magnetic field, can destroy the constants of the motion and permit a dissipative end to the process. The theory of gyrokinetic coronal phenomena is thus dominated by three considerations:

- i. Collisionless, magnetized electrons and ions persist in gyrokinetic drifts, cf. Fig.1 n - I contours of $\Omega_i r_{ii}$, the number of gyrations in a collision time;
- ii. Unmagnetized ions follow the magnetized, gyrokinetic species through space charge fields; any regions of charge separation allow narrow, intense $E \times B$ current channels;
- iii. Late-time populations may reach the core plasma, releasing stored energy, or providing exterior current channels which soften the core implosion.

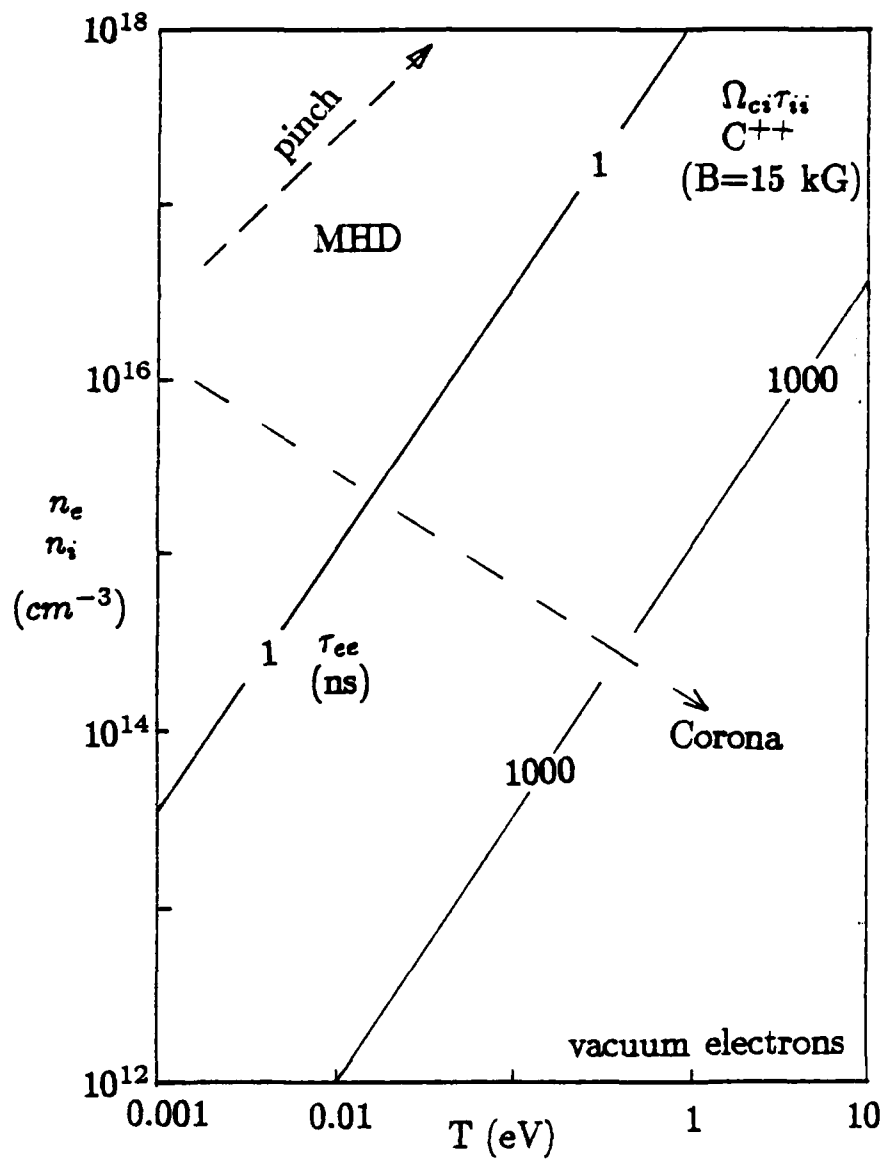


Fig. 1 Contours of $\Omega_{ci}\tau_{ii}$ for C_{12}^{++} at $1.5 \cdot 10^4$ Gauss

- ii. Unmagnetized ions follow the magnetized, gyrokinetic species through space charge fields; any regions of charge separation allow narrow, intense $\mathbf{E} \times \mathbf{B}$ current channels;
- iii. Late-time populations may reach the core plasma, releasing stored energy, or providing exterior current channels which soften the core implosion.

II. Gyrokinetic Plasma Model

The natural substrate on which to build a corona model is collisionless gyrokinetic theory and, as in any Vlasov description, the fundamental class of functions is that of metaequilibria. These time stationary solutions of the gyrokinetic Vlasov equation are associated with the free streaming particle orbits in the self-consistent diode electromagnetic fields. In the following development are: (i) the nature of such metaequilibria, (ii) the minimum set of observable moments required to pose a drift current constitutive relation, and (iii) a general propagation equation appropriate to one dimensional absorption and reflection of transverse magnetic modes. The later sections show a particular solution of the propagation problem and discuss the implications for the PRS.

A. Geometry and Fundamentals

Specializing the gyrokinetic picture of Bernstein and Catto⁵ to a double disk configuration with an interior axial current, a general calculation of electromagnetic power flow across an exterior, collisionless plasma annulus begins with the observation that any ambipolar electric field present can be represented by a potential function $\chi_{amb}(z, r, t)$ so long as its gradients are orthogonal to the purely azimuthal magnetic field. This potential function can be determined in principle by momentum conservation between the magnetized species and the unmagnetized ions, if any. In the simplest form of the problem all species are assumed magnetized and the radial field can be neglected or assumed to come to a quasi-equilibrium configuration just strong enough to preserve the local charge balance. In such a case the primitive variables of the model are easy to summarize.

In the transverse magnetic field: $B = B_\theta(r, t) \hat{\theta}$, the TEM mode electric field: $E_z(r, t) = E(z, r, t) - E_{r, amb}(z, r, t) = E + \nabla \chi_{amb}$, represents the vacuum solution of the radial line. This mode set implies a radial drift velocity: $U = -\hat{r}(E_z/B_\theta)c$, and a total drift velocity: $V = U + u\hat{\theta}$ which includes circulation about the axis. In addition, the peculiar velocity: $w_{r,z} = v_z\hat{z} + (v_r - U_r)\hat{r}$, is orthogonal to the local gyration radius vector, which is in turn located at a gyrophase angle: $\phi = \tan^{-1}((v_r - U_r)/v_z)$. The total particle velocity is then $v = V + w_{r,z}$.

The goal of the gyrokinetic theory is the determination of one body distribution functions which describe the collisionless microstates of the diode corona. Since the corona production process is not expected to favor any gyrophase, the gyrophase is averaged in defining the "gyrokinetic gyroaverage" distribution functions,

$$f_{o,\alpha}(r, \mu_\alpha, u, t) = (1/2\pi) \int d\phi f_\alpha(r, \tilde{\mu}_\alpha, \tilde{u}, t, \phi)$$

where the more accurate gyrophase dependent variables $(\tilde{\mu}_\alpha, \tilde{u})$ are used, at least formally. This implies, however, that some Vlasov metaequilibria, further specializations of the $f_{o,\alpha}$, will depend in effect on averaged values of the higher order invariants which can be labeled by the spatially local values of lowest order invariants.

As a further simplification to the gyrophase averaged kinetic equation which provides the metaequilibria, one has, for this situation, the additional result $\hat{\theta} \cdot (\nabla \times V) = 0$.

All appropriate metaequilibria here are functions of *strict* constants of the motion, such as

$$P_{\theta,\alpha} = m_{\alpha} r \bar{u} \left(1 - \frac{w_{rz} \cos(\phi)}{\Omega r} \right) = m_{\alpha} r u_{\theta} ,$$

expressed in terms of both gyrophase dependent and independent variables. Alternately, an incompletely known constant of the motion admits higher order approximations in the form of gyrophase dependent invariants, e.g.

$$\bar{\mu}_{\alpha} = \frac{m_{\alpha} w_{rz}^2}{2B_{\theta}} (1 - \delta) ,$$

with $\alpha = (e, i)$ and

$$\delta = 2 \frac{V_{z,drift}}{w_{rz}} \cos(\phi) + \frac{c}{2 \Omega} \partial_r \left(\frac{E_z}{B_{\theta}} \right) \sin(2\phi) .$$

When the "gyrokinetic gyroaverage" operation is applied to any function of these strict or approximate invariants, the strict invariants such as the angular momentum, $P_{\theta,\alpha}$, remain useful arguments; but the gyrophase dependent invariants are effectively reduced to the ordinary ones -- magnetic moment, $\mu_{\alpha} = m_{\alpha} w_{rz}^2 / 2B_{\theta}$, and initial guiding center position, r_0 . Note that this reduction in complexity is not a reduction in precision because the lower order variables are really just labels for gyroaveraged higher order invariants.

All such mutually independent invariants, numbers labeling guiding center orbits, therefore determine (through order $1/\Omega$) gyrokinetic Vlasov metaequilibria of the general form

$$f_{o,\alpha}(r, v, t) = \left(\frac{m_{\alpha}^2 r}{2\pi B(r, t)} \right) n_{\alpha}(r, t) F_{o,\alpha}(\mu_{\alpha} , P_{\theta,\alpha} , r_0) .$$

The factor involving r , m_{α} , and B_{θ} arises from the velocity space transformation to μ_{α} and $P_{\theta,\alpha}$. Various functions $F_{o,\alpha}$ are possible, but only the lowest velocity moments are needed to determine the gyrokinetic density evolution. Such moments are *time independent*

expectation values of high order gyrophase averaged invariants, observations or calculations of the corona production phase must establish them.

There is also no magnetic diffusion in the gyrokinetic plasma, viz.

$$\partial_t \mathbf{B} = \nabla \times (\mathbf{U} \times \mathbf{B}),$$

forces the magnetic field evolution to conserve the magnetic flux through any closed curve that follows the drift velocity \mathbf{U} , and the power absorption is therefore determined by the dynamics of the field E_z .

B. Drift Current Density

The current density for the gyrokinetic fluid is *not* accessible through a linear Ohm's law. The axial drifts which constitute such a current are imbalances in mean charged particle flow caused by changes in the local macroscopic fields and the spatial transport of guiding centers. When the gyrokinetic equation is transformed to a sequence of moment equations, this current can be determined through the constraints imposed by momentum conservation, and the time invariant moments

$$L_{||}^2 = \frac{\rho_\alpha}{\rho} \int d\mu_\alpha dP_{\theta,\alpha} F_{o,\alpha} \frac{P_{\theta,\alpha}^2}{m_\alpha^2}$$

and

$$W_\perp = \frac{\rho_\alpha}{\rho} \int d\mu_\alpha dP_{\theta,\alpha} F_{o,\alpha} \frac{\mu_\alpha}{m_\alpha},$$

summed on α the index of magnetized species. The mass density

$$\rho = m_\alpha n_\alpha = m_\alpha \left[\left(\frac{2\pi B(r,t)}{m_\alpha^2 r} \right) \int d\mu_\alpha dP_{\theta,\alpha} f_{o,\alpha} \right],$$

is of course determined by particle conservation. These moments alone define the divergence of the pressure tensor, yielding a current density

$$J_z = \frac{\rho c^2}{B_\theta} D_t \left(\frac{E_z}{B_\theta} \right) + \left(\frac{c}{B_\theta} \right) \left[\frac{\rho L_{||}^2}{r^3} - r^{-1} \partial_r (r \rho B_\theta W_\perp) \right],$$

and an equivalent momentum conservation equation

$$\rho D_t U_r = \frac{\rho L_{||}^2}{r^3} - r^{-1} \partial_r (r \rho B_\theta W_\perp) - J_z B_\theta c^{-1}.$$

For those ion species which are not magnetized, the momentum conservation rule becomes modified by the addition of an ambipolar stress term, a scalar pressure term, and the use of W_o , the "center of mass" velocity, rather than U_r as the flow field, viz.

$$\rho D_t W_o = - \sigma \partial_r \chi_{amb} - \partial_r (P) - J_{ion,z} B_\theta c^{-1}.$$

W_o is then determined primarily by the ambipolar stresses arising when lighter species drift inward ahead of the heavier ions. It will tend to match the U_r drift, with some time delay, as the heavier species are also imploded.

C. General Propagation Equation

Since the current density can be assessed only from the dynamics of U_r and $f_{o,\alpha}$, the most general formulation is to eliminate J_z from the field equations and develop a wave equation for E_z to complete the picture. The mass density and magnetic field are conveniently described by a Lagrangian position $R(r_o, t)$ for the guiding center, while the field equation is naturally posed in terms of dimensionless variables $\tau = t/t_o$, $\tilde{r} = r/l_o$, $l_o = c t_o$. For example, one might set t_o as the current risetime, providing a useful scale for E_z as $E_{z,o} = L_{diode} I_{peak}/t_o$.

The Alfven speed $c_A = (B^2/4\pi\rho)^{1/2}$ arises as a natural, variable wave speed and using the Jacobian associated with the Lagrangian flow, $d\tilde{R}(\tilde{r}_o, r)/d\tilde{r}_o$, the position, density and magnetic field are given by

$$\tilde{R}(\tilde{r}_o, r) = \tilde{r}_o - \int_0^r d\tau_1 \left[\frac{E_z}{B_\theta} \right] (\tilde{R}(\tilde{r}_o, \tau_1), \tau_1) ,$$

$$\rho(\tilde{R}, r) = \rho(\tilde{r}_o) \left(\frac{\tilde{r}_o}{\tilde{R}} \right) \left(\frac{d\tilde{r}_o}{d\tilde{R}} \right)$$

and

$$B_\theta(\tilde{R}, r) = B_\theta(\tilde{r}_o) \left(\frac{d\tilde{r}_o}{d\tilde{R}} \right) .$$

With the \tilde{r} notation suppressed and the fields understood as scaled by $E_{z,o}$, the material derivative is expanded and combined with the "frozen" magnetic field constraint, the current density $\tilde{J}_z = 4\pi t_o J_z$ now becomes

$$\tilde{J}_z = \frac{c^2}{c_A^2} [\partial_\tau E_z - \partial_r \left(\frac{E_z^2}{B_\theta} \right)] + B_\theta \frac{W_{||}}{c_A^2} \left[\frac{1}{r^3} - \frac{B_\theta W_\perp}{W_{||}} \partial_r \ln(r \rho B_\theta W_\perp) \right],$$

where $W_{||} = L_{||}^2 l_o^{-2}$, and $c_A = c_{A,o} (\frac{R}{r_o} \frac{dr_o}{dR})^{1/2}$. A nonlinear wave equation can be developed for E_z by eliminating the magnetic field in Faraday's law and collecting those terms in $\partial_r \tilde{J}_z$ which depend on the displacement current. The propagation equation is then

$$r^{-1} \partial_r (r \partial_r E_z) - (1 + \frac{c^2}{c_A^2}) \partial_r^2 E_z - \partial_r (\frac{c^2}{c_A^2}) \partial_r E_z + \partial_r [\frac{c^2}{c_A^2} \partial_r (\frac{E_z^2}{B_\theta})] = \\ \partial_r \left[B_\theta \frac{W_{||}}{c_A^2} \left(\frac{1}{r^3} - \frac{B_\theta W_\perp}{W_{||}} \partial_r \ln(r \rho B_\theta W_\perp) \right) \right] .$$

This propagation equation points out three important characteristics of the gyrokinetic population --

i. The E_z field evolution remains *hyperbolic* in character, but the electromagnetic phase velocity slows to the Alfvén speed, viz. $\tilde{v}_{ph} = \frac{c_A/c}{(1+c_A^2/c^2)^{1/2}}$. Even when the Alfvén speed equals the light speed, the phase velocity is still half the vacuum value; the Alfvén speed must be much larger than the light speed in order to recover the usual macroscopic transit times. This provides a strong modification to the magnetic diffusion picture, where prompt wave propagation is usually invoked to neglect displacement current. The gyrokinetic medium shows a natural pulse compression mechanism which may find useful applications.

ii. Comparing the coefficient of the first order time derivative of E_z with the mass density and magnetic field evolution rules, one notes that damping occurs when the plasma compression exceeds the magnetic field energy compression, since $\partial_r \ln(c^2/c_A^2) = -\partial_r \ln(\frac{X}{r_o} \frac{dr_o}{dX})$.

This is just the condition for which the guiding centers are being accelerated by an increasing E_z field. In contrast, a plasma which is decelerating its guiding centers will generate E_z field through this mechanism, a kind of negative conductivity. The energy flow between particles and E_z field is smoothly reciprocal and non-dissipative.

iii. The extended sources of reflection are dependent on the ρ, B compression profiles in such a way that the cross derivative term can combine with the right hand side to produce spatially similar source terms when the E_z field is primarily inductive and the compression is spatially homogeneous. This fact is exploited indirectly in the next section.

III. Special Cases

One can restrict the problem to quasi-static fields ($\partial_r E < \tilde{J}$) and seek specialized solutions to the momentum conservation equation. In such cases the E_z field is a prescribed space-time function and dominantly inductive in character, external electrical reservoirs supply any needed currents, and the solution defined inside some radius can be viewed as a circuit element.

Using the conserved flux $\psi_<(r_o) = \int^{r_o} dr B_\theta(r)$ to formulate the $\mathbf{J} \times \mathbf{B}$ stress term, the momentum equation can be written

$$D_t U_r = \tilde{R} = -\frac{c_A^2(r_o)}{r_o} \frac{d}{dR} \left(R \frac{dr_o}{dR} \right) + \frac{L_{||}^2}{R^3} - \frac{\partial_R (R \rho \frac{dr_o}{dR} H_\perp(r_o))}{R \rho},$$

where $H_\perp(r_o) = B_\theta(r_o) W_\perp(r_o)$, and $c_A^2(r_o) = [\partial_{r_o} \psi_<]^2 / 4\pi \rho_o$.

If one has the further restrictions that H_{\perp} , L_{\parallel}^2 are independent of r_o , and that the initial $B_{\theta}(r_o)$ is imbedded such that $r_o^{-1} c_A(r_o) = a_o^{-1} c_A(a_o)$, a constant, then a specific radial density profile can link the two tensor pressure components -- the isothermal perpendicular energy and the rigid rotor circulation energy -- with the uniform Alfvén compression profile. The introduction of the temporally scaled profile

$$n(r, t) = \frac{a_o}{r} M_o \exp - \left[\left(\frac{r}{a_o} \frac{1}{\lambda(t)} \right)^2 + \left(\frac{\lambda(t) L_{\parallel}^2}{2 H_{\perp}} \right) \frac{1}{r^2} \right],$$

produces a single equation of motion for $\lambda(t)$ at any radius $r_o \leq r_I^*$, the radius of vanishing current density. The total current, within $r_I(t) = \lambda(t) r_I^*$, for N ions per cm, is

$$I_{total} = \frac{I_{Bennett}}{\epsilon \pi^{1/4}} S^{3/4} \exp \left[\frac{b_o}{a_o} - \frac{1}{2} \left(S + \frac{b_o^2}{a_o^2} \frac{1}{S} \right) \right],$$

where $I_{Bennett} = (2Nm_i H_{\perp})^{1/2}$, $c_S = (2 H_{\perp})^{1/2}$, $\epsilon = c_S/c_A$, $S = \frac{3}{4} + \left(\frac{9}{16} + \frac{b_o^2}{a_o^2} \right)^{1/2}$, and $b_o = \left(\frac{L_{\parallel}^2}{2 H_{\perp}} \right)^{1/2}$. For a given current, the effective electron temperature is $T_{\perp} = 3.47 \cdot 10^{-13} \frac{(\epsilon I_{total})^2}{N}$, e.g. $T_{\perp} = 0.994$ [keV] at $I_{total} = 1.26$ MA , $N = 5.0 \cdot 10^{16} \text{ cm}^{-1}$, $\epsilon = 0.1$. Such a typical profile set is shown in Fig. 2.

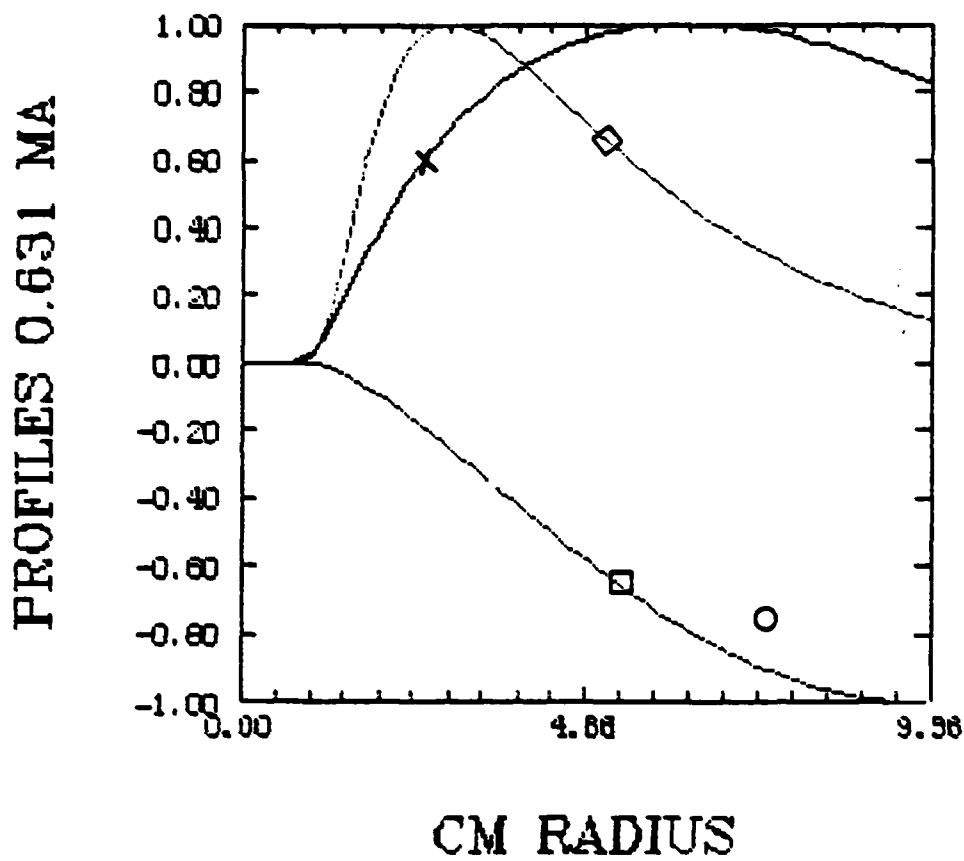


Fig. 2 Typical Solution Profiles

$n : 3.55 \cdot 10^{14} \text{ cm}^{-3}$ \diamond $B_\theta : 1.45 \cdot 10^4 \text{ Gs}$ \times
 $-E_z : 4.2 \text{ stV/cm}$ \square $U_r : 9.36 \cdot 10^6 \text{ cm/sec}$ \circ

Normalizing the time by the sound speed associated with H_{\perp} , let $t_S = a_o/c_S$, $t_S d\tau = dt$. The scale factor equation of motion in "sound transit time units" is then

$$\ddot{\lambda} = \frac{1}{\lambda(\tau)} \left(\frac{1}{\lambda(\tau)} - \frac{1}{\epsilon} \right),$$

with initial conditions $\dot{\lambda}_o = d\tau \lambda|_{\tau_o}$, $\lambda(\tau_o) = 1$. This equation has an energy integral,

$$h = 1 + \dot{\lambda}_o^2/2 - \frac{1}{\lambda} \left(1 + \frac{\lambda \ln \lambda}{\epsilon} \right).$$

For $\epsilon < 1$, $\dot{\lambda}_o = 0$ there is always an interior turning point and oscillation inside $\lambda = 1$; for $\epsilon > 1$, $\dot{\lambda}_o = 0$ there is an exterior turning point and oscillation outside $\lambda = 1$. Small values of ϵ imply implosion at velocities higher than c_S and deeper turning points arrived at more quickly. Some trajectories and turning points are shown in Fig. 3, labeled by various $\dot{\lambda}_o$, ϵ combinations.

Such a gyrokinetic oscillator represents a special case of the propagation problem for which:

$$\lambda(\dot{\lambda}_o, \tau)$$

$$\dot{\lambda}_o = -0.50, \quad \times$$

$$\dot{\lambda}_o = -0.25, \quad \diamond$$

$$\dot{\lambda}_o = -0.0, \quad \square$$

$$\lambda_{min}(\dot{\lambda}_o, \epsilon)$$

$$\dot{\lambda}_o = [-0.0, -5.0]$$

$$\epsilon = [0.05, 0.95]$$

Fig. 3 Typical Trajectories and Turning Points

- a. the Alfvén speed is linear in space and invariant on a Lagrangian trajectory, and
- b. the larger total current cases are those for which the electron population is hotter and the Alfvén speed is also large compared to the sound speed, and
- c. the electromagnetic energy propagation is slowed further, *below* the Alfvén speed, by the tensor pressure of the particle population and suffers a complete reflection in the expansion phase of the motion.

The present solution contrasts with a comparable MHD solution due to Felber⁶ in that the implosion remains hollow on axis, recoiling from the "centrifugal potential" at some nonzero radius. In addition, the tensor pressure requires no "completing" equation of state assumption, being specified through observables at some initial time. The current density is also constituted in a fully self-consistent manner, requiring no "infinite conductivity" assumption in a linear Ohm's law.

The energy absorbed over one quarter cycle $H(\epsilon, \dot{\lambda}_0)$, i.e. down to the turning point, can be conveniently written in terms of the total current at any typical value ϵ_0 and the logarithm of the turning point value λ_{min}

$$H(\epsilon, \dot{\lambda}_0) = \left(\frac{\epsilon_0}{\epsilon} \frac{I_{total}}{c} \right)^2 \ln \left(\frac{1}{\lambda_{min}(\epsilon, \dot{\lambda}_0)} \right),$$

and $H(\epsilon, \dot{\lambda}_0) \left(\frac{\epsilon}{\epsilon_0} \right)^2$ is shown below for $I_{total} = 1.26$ MA, $m_i = 12$ amu, $\epsilon_0 = 0.1$.

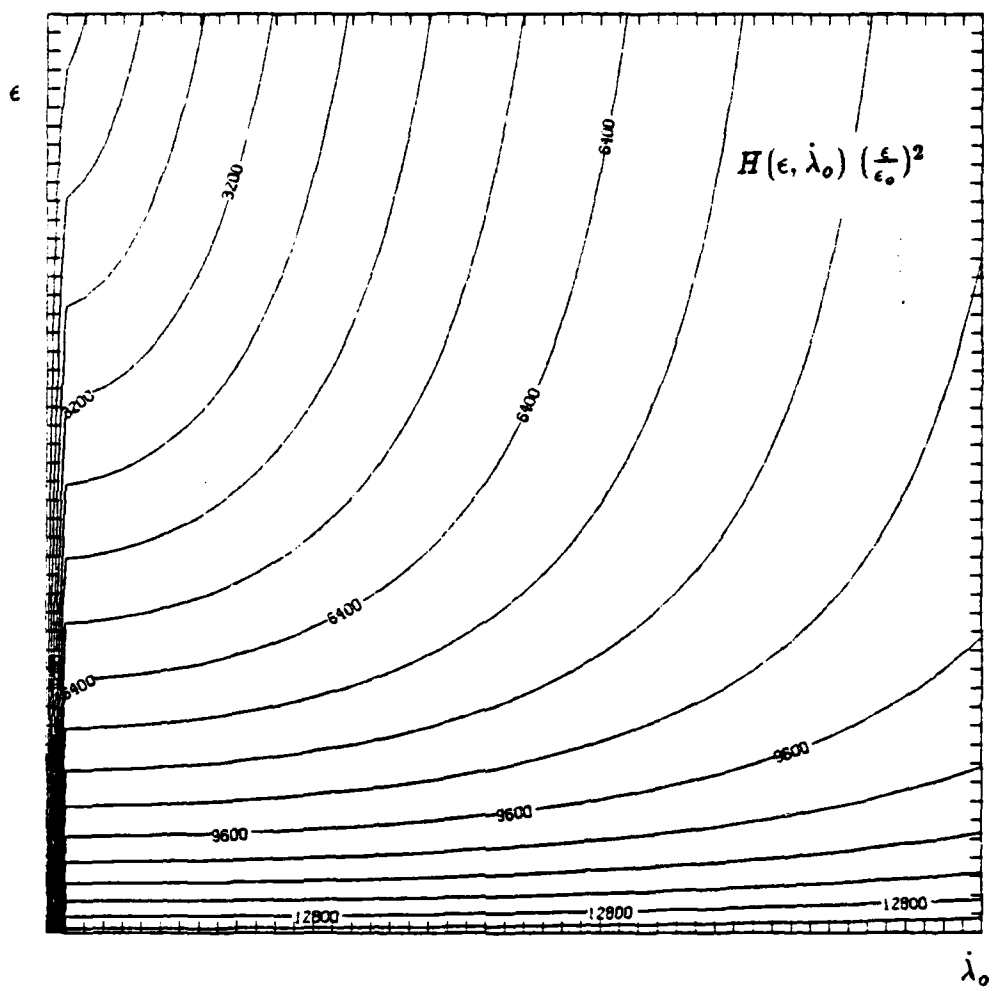


Fig. 4 Quarter Cycle Energy Absorption [J/cm]

IV. Implications for DNA Objectives

If gyrokinetic current densities approaching those of the self-similar oscillator are actually present in PRS diodes, then one must suspect a significant loss of driver current to the main pinch. The power absorbed in the corona plasma may be much more modest, since it depends on the difference of incoming and outgoing E_z field components, but the possibility of significant reflected power from the corona cannot be discounted. However this is the worst case scenario.

It is more likely that gyrokinetic populations are difficult to obtain in the clean form required by our simple solution. They may tend to occur only once in a while and participate in the many factors which produce the shot to shot variation in PRS diodes. It is clear from the theory to date that a serious experimental effort is warranted to fix the early peripheral conditions which help define the gyrokinetic corona. Experiments of particular importance would be early time neutral gas *density* measurements as (r, z) profiles and spacetime resolved magnetic field measurements emphasizing the period of run-down and stagnation. Since the radial extent of the gyrokinetic corona can be on the order of centimeters, spectroscopic (Zeeman effect) measurements based on seeded trace impurity concentrations may prove viable. Such work can be guided by more general theoretical calculations of the power flow which are made possible by the progress achieved so far.

Even more intriguing is the issue of microstability for the Vlasov solutions examined here. Having fixed only the lowest velocity moments in defining the current density, a infinite sequence of higher moments remains available and the quasilinear spectrum of unstable modes which might be excited remains to be determined through these observables. Insofar as the gyrokinetic populations have been shown

capable of sustaining high currents, these populations may well prove to be useful as *switches* if the conditioning of the higher moments can produce unstable plasmas which will *interrupt* those currents in a predictable time frame. The present formulation is perhaps the first theoretical development suited to the study of such phenomena in a simple, yet geometrically relevant context.

References

1. *Development and Exploration of the Core-Corona Model of Imploding Plasma Loads*, J.U.Guillory, R.E.Terry, DNA Report 5234F, July 1980. AD A131175
2. *Modeling of Imploded Annular Plasmas*, J.U.Guillory, R.E.Terry, DNA Report 6152F, April 1982. AD A126179
3. J.Shannon, private communication.
4. N.R.Pereira, private communication.
5. I.B.Bernstein, P.J.Catto, *Phys.Fluids* 28(5),p.1342 (1985)
6. F.S.Felber, *Phys.Fluids* 25(4), p.643 (1982)

F. Eroding Foil Switch Model for Mass Flow Switches

I. THE EFS MODEL AND FIELD PENETRATION

The Eroding Foil Switch (EFS) model was originally formulated¹ as a zero dimensional picture to fit unexplained experimental results. It was derived, not from first principles but rather empirically, from study of experimental results and physically reasonable assumptions. Preliminary results of both theory and numerical simulation for the magnetic diffusion process in thin foils have shown the basic concepts of the model to be accurate and a more thorough investigation is ongoing.

While the acceleration of foils in a coaxial geometry is truly a two dimensional problem due to variation of the magnetic field strength with radius, it is clear from exercises with the simulation code AXFOIL² that proper "mass grading" can produce a stably accelerated, essentially one dimensional motion. This suggests that models for the kinematics and field dynamics which are restricted to the axial domain can remain viable analysis tools.

In events like the "foil switch"³ and "magnetic gate"⁴ experiments at LANL the foil behavior indicates that some substantial mass loss is a prime feature. For both experiments the object is to accelerate a foil, using Lorentz forces, past a gap in the transmission line where switching can occur. The foil switch experiment is done in a coaxial transmission line with one switch gap, while the magnetic gate experiment occurs in a linear stripline with three switching gaps. In Fig. 1, 2, and 3 the geometry, current and foil position are summarized to indicate that as little as five percent of the original mass may

participate in the final commutation of the current. The switch signal itself was a linear rise over 10^{-6} sec, one tenth the characteristic time associated with the foil equation of motion with the mass fixed at its original value. This indicates a broad current sheath, perhaps a centimeter wide, as the mechanism of current transfer to the "load" cavity. The lost mass was also hot, optical pyrometry indicated a foil temperature of 4000 °C. The mass loss was smooth in time rather than abrupt and a fair fraction of the foil had apparently vaporized.

Since the foil mass had been chosen to insure much lower temperatures under the assumption that the current would be uniformly distributed, it seems that some localization of the current is responsible for both the high temperatures and the rapid, nonuniform acceleration of the switch mass. Concentration of the current in a thin surface layer would produce early heating and mass erosion. The higher temperature increases the local resistance and forces the current density to propagate deeper into the metal. As the process continues the heated portion of the switch either melts or vaporizes, but the point of maximum axial stress is always in front of the high temperature zone. Some of the liquid phase and all of the vapor phase is then left behind and the axial kinematics is determined by the mass ahead of the $J_r \times B_\theta$ stress front.

A. Eroding Slab Picture

Regardless of the details in the mass loss process, the rate of mass loss should be proportional to the ohmic heating rate and thus to the square of the magnetic field on the upstream boundary of the foil. As a rough cut at the erosion process, one may then let

$$\partial_t \mu = -K \frac{\delta B_\theta^2}{8\pi} ,$$

where μ is the foil mass per unit area, and K is measured in $[\text{gm/cm}^2 \text{ sec bar}]$ when the magnetic field pressure is measured in bars, $1 \text{ bar} = 1.0 \cdot 10^6 \text{ Gs}^2$. Since the mass graded foil equation of motion for $V_z(t)$ can be integrated from rest to yield

$$\mu V_z = W(t) = \int^t dt_1 \frac{\delta B_\theta^2(t_1)}{8\pi},$$

the axial velocity of the eroding foil can be expressed in terms of the velocity $V_c(t) = W(t)/\mu_0$ of a fixed mass foil, viz.

$$V_z(t) = \frac{V_c(t)}{(1 - K V_c(t))},$$

with μ_0 the initial foil mass. In these expressions the field value δB_θ^2 connotes a field pressure *difference* across the slab. As mass

erodes this pressure difference is applied deeper in the slab; this rough model assumes that eroded mass is highly resistive -- the original surface δB_θ^2 is just shifted to the interior. In order for the model to retain self-consistency, the factor K must be independent of radius. In any first principles development of this theory therefore one must heed whatever constraints are needed to make this happen.

The factor K has been evaluated in three ways for the parameters of the LANL experiment. The first is through a finite difference calculation of the erosion process; the second, through a self-similar solution for the field penetration; the third, by examination of the experimental kinematics. All three evaluations are in rough agreement.

B. Magnetic Diffusion and Self-Similar Descriptions

The magnetic diffusion equation is naturally posed in terms of dimensionless variables $\tau = t/t_0$, $\tilde{z} = z/l_0$, $l_0 = c t_0$. The axial velocity of the foil is then $\beta_z = V_z/c$, and the effective resistivity is $\eta = 1 / t_0 \sigma$. This resistivity is generally a function of the internal energy per unit mass of the switch material. In the following development the basic simulation unit is a ring at some intermediate radius r_0 in a coaxial waveguide, with a mass M_{ring} . The electromagnetic power deposition in this ring is the spatial integral of radial current density squared and the local resistivity, viz.

$$D_\tau Q = \left(\frac{l_0 A_0 h_z}{16\pi} \right) \eta(Q(\tilde{z}, \tau)/M) [\partial_{\tilde{z}} B_\theta]^2,$$

where $h_z = \tilde{z}_{j+1} - \tilde{z}_j$ the axial cell size, $A_0 = (r_o^2 + h_r^2) - r_o^2$ the cross sectional area factor, and $D_\tau Q$ is the material derivative with respect to the scale time of the internal energy per ring. Integration of this equation, over any time domain on which the axial gradient of B_θ is provided, allows the self-consistent evaluation of the resistivity as $\eta(Q(\tilde{z}, \tau)/M_{ring})$. Various resistivity models are available and the present implementation arises from a fit to LANL and AFWL data for Aluminum⁵ of the form $\eta = \eta_0 [1 + A(Q/M) + B(Q/M)^2]$.

Turning to the magnetic field, one may write the diffusion equation with the same material derivative operator applied to B_θ

$$D_\tau B_\theta = \frac{1}{4\pi} \partial_{\tilde{z}} [\eta(Q(\tilde{z}, \tau)/M) \partial_{\tilde{z}} B_\theta] - B_\theta \partial_{\tilde{z}} \beta_z.$$

The convective term involving the axial gradient of β_z can be ignored in the simplest EFS application because the material is assumed incompressible until it is in the vapor phase and long lost to the mass being convected.

This formulation will leave the solution invariant with the radius r_0 provided the ring mass is graded such that the effective mass density scales $\propto (R_{scale}/r_0)^2$ and the driving boundary value is scaled $\propto (R_{scale}/r_0)$. The axial scales must be preserved in the transformation, however, so the EFS theory is limited, rigorously, to those mass graded cases where the switch *mass density*, rather than the axial foil thickness, is conditioned.

With the above *caveat* in mind, to assess the EFS mass erosion constant K one need only supply an upstream boundary condition for the field B_θ , together with a switch mass and radius which are consistent with the experiment. The results are illustrated in Fig. 4.

Following the current density peak across figures such as these one can assess the mass uncovered by its progress and thus establish a factor K , at the foil mass and for the driver current waveform chosen in any model solution. At present this analysis indicates a value $K_{pdc} = 27$ [gm/cm² sec bar], but planned model refinements and more detailed exploration of the initial conditions will probably reduce this result.

An alternate path to such an estimate lies in self-similar or progressive wave solutions to the diffusion and heating equations. Here of course the specialized boundary conditions will not accomodate general driver waveforms, but the essential elements of the penetration physics can be displayed. Let $\tilde{A} = \eta_0 A/M \approx 4.8 \cdot 10^{-21}$ [sec bar], using the resistivity expansion above. In the case $\beta_z = 0$, consider the diffusion equation in the region where $\partial_z J_r = \partial_z^2 B_\theta = 0$. At this point the diffusion equation is a simple advective relation, viz.

$$\partial_r B_\theta = \frac{1}{4\pi} \partial_z \eta \partial_z B_\theta ,$$

and any progressive wave solution will propagate at speed $V_B = \frac{c}{4\pi} \partial_z \eta$. Using the heating equation with this simple field equation provides a local spatial constraint on η

$$\partial_z \eta = \left[\frac{\tilde{A} \eta}{4\pi} \right]^{1/2} \partial_z B_\theta .$$

If this equation is integrated over an interval $\delta \tilde{z}$ back into the magnetic field wave, one can relate η to the change in magnetic field pressure, obtaining $\eta = \frac{\tilde{A} \delta B_\theta^2}{16\pi}$. Whereupon a first order estimate of the gradient in η and some simplification provides the speed

$$V_B = \left(\frac{c \tilde{A}}{32 \pi^2} \right) \frac{\delta B_\theta^2}{\delta \tilde{z}} .$$

Evaluating in cgs units and recalling that $\partial_t \mu = -K \delta B_\theta^2 / 8\pi = -\rho_{Al} V_B$, the "self-similar" erosion factor becomes

$$K_{ss} = \frac{c^2 \tilde{A} \rho_{Al}}{4\pi \delta z} = 21 [gm/cm^2 \text{ sec bar}] .$$

II. The EFS Model and Foil Kinematics

As the mass erosion proceeds through the slab, a final state obtains wherein the foil must vaporize to a slightly ionized, snowplowed plasma. At this point the remaining mass will convect at the local Alfvén

shock speed⁶ $V_A = \left(\frac{B_\theta^2}{8\pi\rho} \right)^{1/2}$. Using the value $V_A = 3.0 \cdot 10^5$ cm/sec from the LANL switch experimental parameters and assuming a change from

erosion to convection at a time t_E , the equation to fit for the experimental kinematics can be written

$$\Delta Z_{gap} = \left(\frac{V_A}{B_f} \right) \int_{t_E}^{t_f} dt_1 B(t_1) + \int_0^{t_E} dt_1 \frac{W(t_1)/\mu_o}{(1 - K W(t_1)/\mu_o)}.$$

By matching velocities at t_E from the two model phases, one may estimate t_E and then unfold K through the match condition itself,

$$\frac{\mu_o}{W(t_E)} - K = \frac{B_f}{V_A B_E}.$$

For the LANL switch parameters one finds $t_E = 3.9 \mu\text{sec}$ and $K = 19 [\text{gm/cm}^2 \text{ sec bar}]$, somewhat below the two theoretical estimates.

III. Implications for DNA Objectives

At the present level of sophistication, the EFS model appears to explain many basic features of mass flow switches which originate the switching action with a solid phase conductor. If a well defined experiment is fielded, the detailed application and verification of the model will, if successful, provide a very useful "calibration" of the mass erosion process. A useful experiment would involve three critical elements:

i. Axial resolution of the location of the current channel, and perhaps the width as well, as a function of time. The obvious method would be sequential current monitors along either coaxial conductor, but the short length of travel may present something of a challenge.

ii. Temporal resolution of the voltage, measured downstream across the switch, during the conduction (run-down) phase. This acts as a diagnostic of motional impedance and field penetration through the foil. Naturally, it suggests the use of an open circuit termination on the coaxial line in which the foil travels.

iii. Temporal resolution of the upstream foil temperature and the foil blowoff material, with particular attention to an estimate of the size of any liquid droplets present in the eroded material.

Once thoroughly tested, the EFS model can be incorporated in more general switch models, such as AXFOIL, and will thus improve the physics content of such codes.

References

1. J.E.Brandenburg, private communication in MRC memoranda -- "The Eroding Foil Switch (EFS) Model" and "An Improved EFS Model".
2. J.Ambrosiano and J.E.Brandenburg, "AXFOIL: A Simple, Finite Element Computer Code to Model Moving Axial Foils", Berkeley Research Associates Technical Report BRA-85-310R, July 1985.
3. D.R.Kania, *et. al.*, Appl.Phys.Lett.,(45)26, 1984
4. D.R.Kania, *et. al.*, Appl.Phys.Lett.,(44)741, 1984
5. I.R.Lindemuth, *et. al.*, J.Appl.Phys.(57), p.4447,1985
6. N.A.Krall and A.W.Trivelpiece, *Principles of Plasma Physics*, McGraw-Hill, New York, p.124 .

Foil Switch Behavior

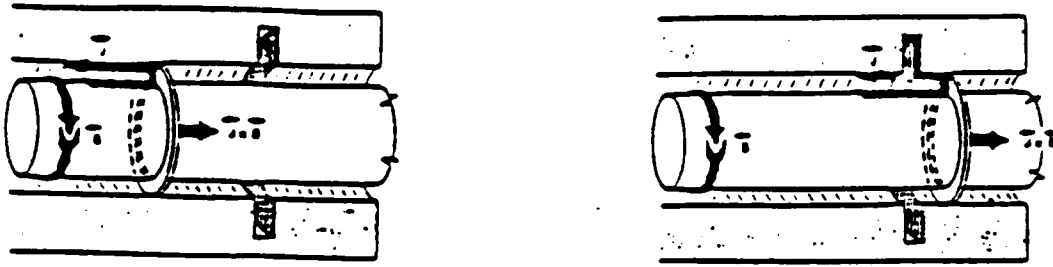


Figure 1. A Diagram of the LANL Foil Switch Experiment.

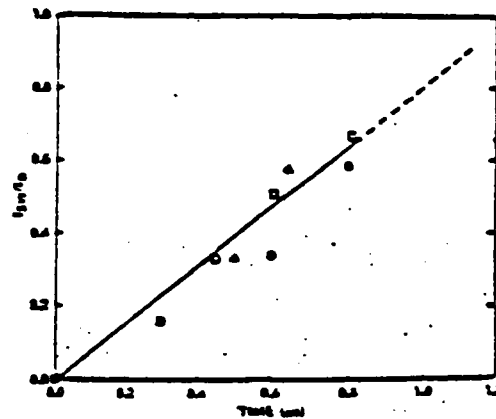


Figure 2. Plot of normalized switched current (switched current divided by bank current) for Los Alamos foil switch experiment.

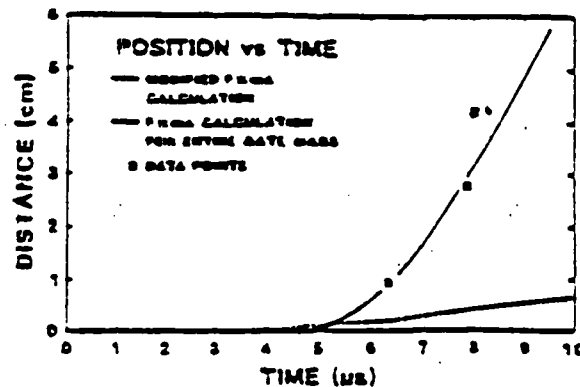
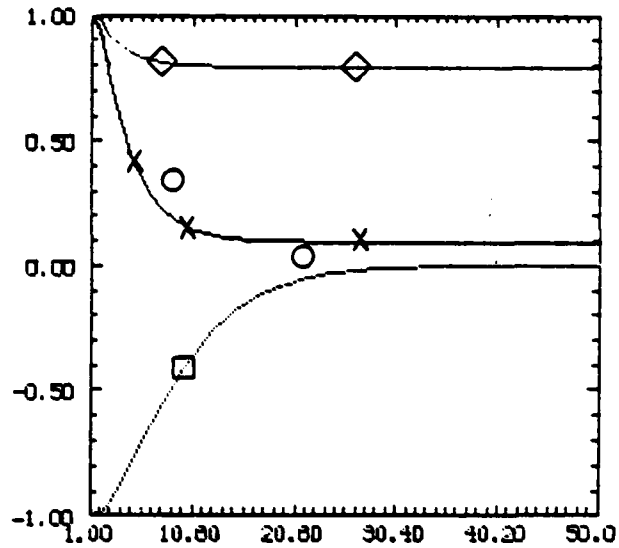


Figure 3. A plot of foil position versus time from 1) experiment data (squares) 2) $F = ma$ calculations using the entire foil mass (dotted curve). 3) $F = ma$ calculations using 5% of the original foil mass (solid curve).

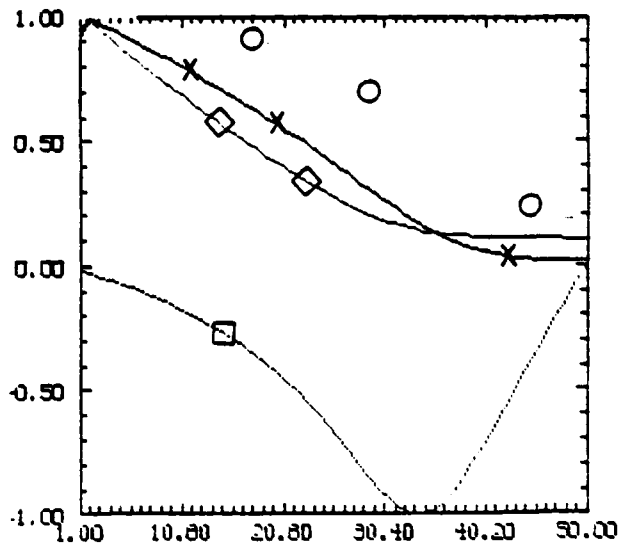
Time: 1.20 μ sec

B_0 : $1.84 \cdot 10^6$ Gs — \circ
 Q : $1.86 \cdot 10^6$ ergs — \times
 η : $3.11 \cdot 10^{-13}$ sec — \diamond
 J_r : $2.20 \cdot 10^{11}$ stA/cm² — \square



Time: 6.20 μ sec

B_0 : $2.82 \cdot 10^6$ Gs — \circ
 Q : $1.26 \cdot 10^6$ ergs — \times
 η : $2.36 \cdot 10^{-12}$ sec — \diamond
 J_r : $1.40 \cdot 10^{11}$ stA/cm² — \square



CELL INDEX

Fig. 4. EFS field penetration behavior.

G. Proton Beam Deposition, Heating, and Radiation from an Fe Plasma

I. INTRODUCTION

Recent advances in pulsed power and diode technologies have made it possible to deliver intense proton beams onto a target with high efficiency. Thus, the interaction of energetic charged particle beams with different materials has become an active field of research. A significant application for this research is the use of ion beams for x-ray generation. Other applications include and weapons lethality and vulnerability studies.

The interaction of a monoenergetic one MeV proton beam with a planar aluminum slab of 15 μm thickness has been previously investigated.¹⁻³ This beam was assumed to consist of a square-shaped pulse of 10 nanosecond duration with a flux of 10^{26} protons $\text{cm}^{-2} \text{sec}^{-1}$. The beam intensity on target is $1.6 \times 10^{13} \text{ W/cm}^2$, which is comparable to intensities available with current pulsed-power generators.

In the present study, the interaction of this same proton beam with a planar 8.0- μm -thick iron slab is treated. This distance approximately corresponds to the range of a one MeV proton in cold solid density Fe.⁴

The Fe atomic model used in this calculation did not have excited level structure in ionization stages below Fe XVI. Only ground states were carried for stages I through XV. While this lack of level structure and the resulting omission of lines from the radiation transport scheme can modify the energy balance in regimes where these lower stages are highly populated, it is estimated that the effect is less than a factor of two on the energy lost due to radiation.

The scheme for treating the proton beam-iron slab interaction is fundamentally the same as that described in Refs. 1-3 for treating the proton beam-Al slab interaction. The hydrodynamic response is treated via a one-dimensional model with a sliding-zone version of flux corrected transport. A special gridding algorithm moves zones in a Lagrangian fashion and adjusts the mesh in order to resolve steep gradients in the flow. A single temperature is assumed. A collisional radiative equilibrium treatment of the ionization balance is used. Radiation

transport is treated with a hybrid scheme which uses multifrequency ray tracing for the continua, and a probability-of-escape method for lines. The radiation transport is coupled self-consistently into the ionization dynamics. The proton stopping power includes contributions from bound atomic electrons, free plasma electrons, and plasma ions.

A major difference between this work with Fe as the target material and the previous work with Al as the target material is in the treatment of the bound electron stopping power. For the proton-Al^{+q} interaction, where q is the ionic charge, detailed stopping power cross sections are available;⁵ for the proton-Fe^{+q} interaction, no such data are currently available. In a previous simulation⁶ of a proton beam-Fe slab target interaction, a modified local-oscillator-model (LOM)^{7,8} was used to estimate stopping power due to bound electrons. Figure 1 (taken from Ref. 8) shows an LOM calculation of proton stopping power in neutral, solid density Fe in comparison with the Andersen-Ziegler⁴ data for this case. In this case, the LOM gives good results at low and high energies, but it underestimates the peak and shifts it to lower energy. This fact, coupled with some problems with the line spectra (which have since been resolved) in the previous treatment,⁶ led to a second attempt to treat the proton beam-Fe target interaction.

In the present treatment, an analytic fit to the Andersen-Ziegler⁴ proton-neutral Fe stopping power was obtained. Then, stopping power for Fe ions was scaled from the neutral Fe stopping power by the number of atomic electrons on the ion; i.e.,

$$S_b(p + Fe^{+q}) = ((Z - \bar{Z}) / Z) * S_b(p + Fe^{+0}),$$

where S_b is the bound electron stopping cross section, Z is the atomic number, and \bar{Z} is the average charge of the target Fe ions.

There are some difficulties with this stopping power model. One is that the peak stopping power occurs at the same proton energy for all ions. In the detailed Al^{+q} stopping power calculations⁵, the peak shifted to higher energy as q increased. Another difficulty is that Eq. (*) probably overestimates stopping power due to the ions. The detailed Al^{+q} calculations show the ratio of ion to neutral stopping power to be lower

AD-A167 849

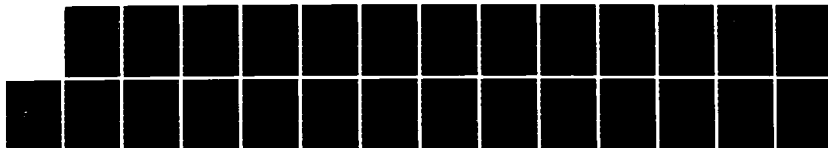
ADVANCED CONCEPTS THEORY ANNUAL REPORT 1985(U) NAVAL
RESEARCH LAB WASHINGTON DC 23 APR 86 NRL-MR-5759

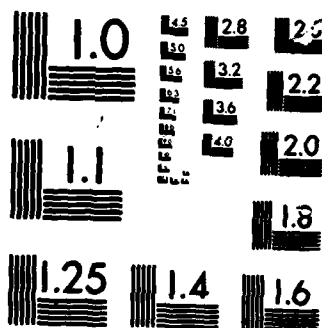
2/2

UNCLASSIFIED

F/G 28/9

NL





MICROCOPY

CHART

than that indicated by Eq. (1). However, due to the lack of more detailed information, some assumptions regarding stopping power must be made to treat the problem.

Some results of the most recent proton beam-Fe slab target interaction simulation will now be given and discussed. Figure 2 shows the energy history and partitioning in the beam target interaction. The effect of the beam cutoff at 10 nsec can be clearly seen as the total plasma energy decreases after this time. This is due to thermal (internal) energy losses as the plasma radiates and to potential (ionization) energy as the ions recombine. The radiated energy is negligible at early times, but becomes a significant factor at late times; at 13.2 nsec, it represents about 45 per cent of the deposited energy.

Figure 3 gives temperature and density profiles at different times in the plasma evolution. Generally the plasma gets wider and less dense as time goes on. However, the temperature appears to be relatively constant over most of the plasma at later times. This is reflected in the fact that the internal energy curve is fairly constant during the later times until the beam is turned off. The 13.248 nsec temperature profile is slightly cooler than the 10 nsec profile.

Figure 4a displays the temperature and density profile at 1.59 nsec from the previous proton beam-Fe target treatment.⁶ Although the plasma widths are approximately the same, the rear surface temperature is lower and the density higher in Fig. 3(a) at 1.569 nsec. The front surface temperatures are about the same in the two cases, but the present treatment yields a much lower front surface density. The differences in these profiles is due to the fact that Eq. (1) gives larger stopping powers than the LOM; hence the beam does not penetrate as far into the target and deposits its energy nearer the front.

Figure 4b shows temperature and density profiles at 9.76 nsec in the previous treatment of an Fe target.⁶ Comparison with the 10 nsec profile in Fig. 3 shows that the previous treatment produced much more uniform plasma profiles near beam shutoff, while the present treatment produces distinct variations in temperature and density near the rear. The front surface values are about the same in the two treatments. These differences are again due to the greater penetration allowed by the LOM stopping power model.

Figure 5 shows the time behavior of the density, temperature, and average charge \bar{Z} at the front and rear surfaces. At the front side, temperature and \bar{Z} rise very rapidly and then maintain fairly steady values afterward; the density drops rapidly at first, then drops more slowly to about 0.01 gm/cm^3 around 13 nsec. At the rear surface, density and temperature change very rapidly initially, then the variation proceeds more slowly. They do not achieve steady values however. The \bar{Z} curve follows the temperature curve. The peaks in the curve at 6 nsec are due to a shock arriving at the rear.

In Fig. 6 are displayed the calculated front and rear spectra at the same times as the plasma profiles in Fig. 3. The lack of level structure in ion stages below Fe XVI is clearly shown by the scarcity of lines at 1.569 nsec. As might be expected from the density and temperature plots, most of the radiation is lost from the front of the plasma; most of this radiation comes from zones near the front of the plasma. For the rear spectra, the least energetic radiation arises from zones near the rear. The increased emissions near 0.7 keV and around 2 to 3 keV consists of contributions from interior zones which escape through opacity "windows". At 10 nsec and 13.248 nsec, the radiation rises due to contributions from interior zones. These bumps in the rear spectra coincide with minima in the optical depth curves allowing radiation emitted in the interior to "shine through" to the rear side. To a lesser extent, the same phenomenon accounts for the relative maxima and minima in the front spectra. In the previous Fe target simulation,⁶ the rear surface emission was much higher. In that case, the front and rear spectra at 9.76 nsec and 12 nsec were very nearly equal. These differences are presumably due to the differences in stopping power predicted by the LOM and used in this model.

The results of this study and its comparison with a previous treatment⁶ of the same problem reinforces the necessity of having good stopping power data in ion beam-target interaction studies, particularly in higher Z targets where bound electron stopping power is significant over a wide range of temperatures and densities. In low Z ions where free electron stopping becomes dominant at low \bar{Z} , accurate bound electron stopping power becomes less critical at later times.

The Fe model used here has no structure in ion stages below Fe XVI; hence, radiation transport is affected at all stages of this simulation, since the maximum \bar{Z} attained was about 16. Radiation losses are hence underestimated, particularly near the rear surface, but it is estimated that the error is less than a factor of two. It was found that radiation transport and losses are a significant factor in beam-target interactions.

This is a one dimensional treatment; hence, field effects and energy flow perpendicular to the beam direction are omitted. These factors could change the profile shapes and magnitudes, and the projectile ranges in the plasma, and hence alter the results presented here.

References

1. J. E. Rogerson, R. W. Clark, and J. Davis, Phys. Rev. A 31, 3323 (1985).
2. J. E. Rogerson, R. W. Clark, and J. Davis, NRL Memorandum Report 5482 (1984).
3. Plasma Radiation Branch, PPD, NRL Memorandum Report 5590 (1985).
4. H. H. Andersen and J. F. Ziegler, Hydrogen-Stopping Powers and Ranges in all Elements, Pergamon Press (1977).
5. E. J. McGuire, J. M. Peek, and L. C. Pitchford, Phys. Rev. A 26, 1318 (1982).
6. Plasma Radiation Branch, PPD, NRL, DNA Progress Report (5 July 1985).
7. R. K. Nesbet and J. F. Ziegler, Appl. Phys. Lett. 31, 810 (1977).
8. J. E. Rogerson, NRL Memorandum Report 4485 (1981) ADA 097772.

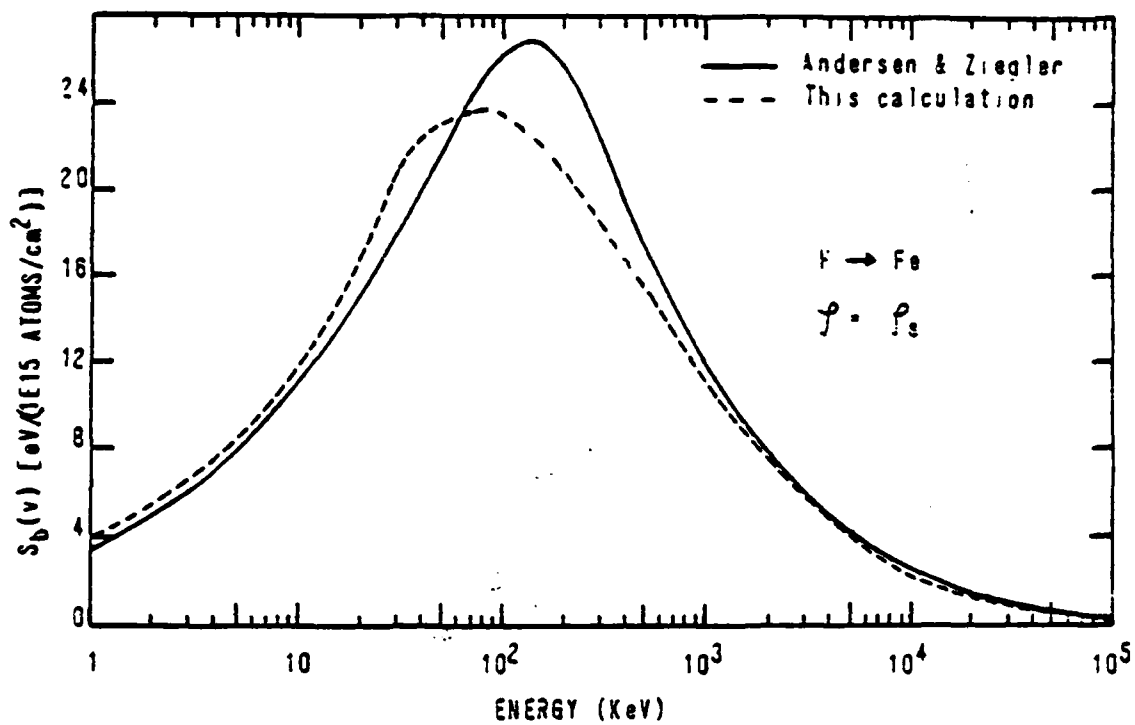


Fig. 1 — Comparison of the stopping power of protons in neutral Fe as given by the LOM and Ref. 4.

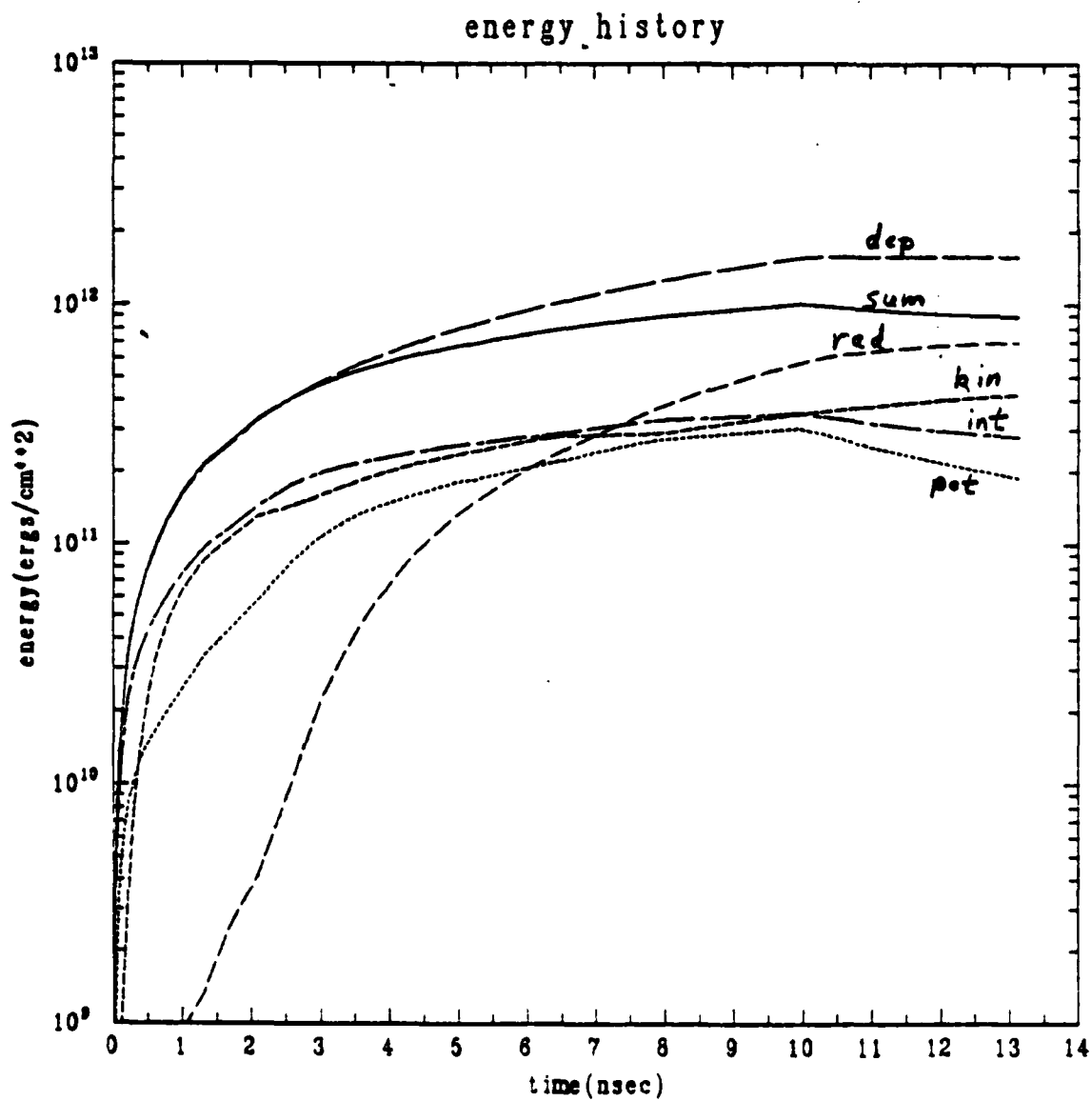


Fig. 2 — Energy history and partitioning in the beam-plasma interaction.

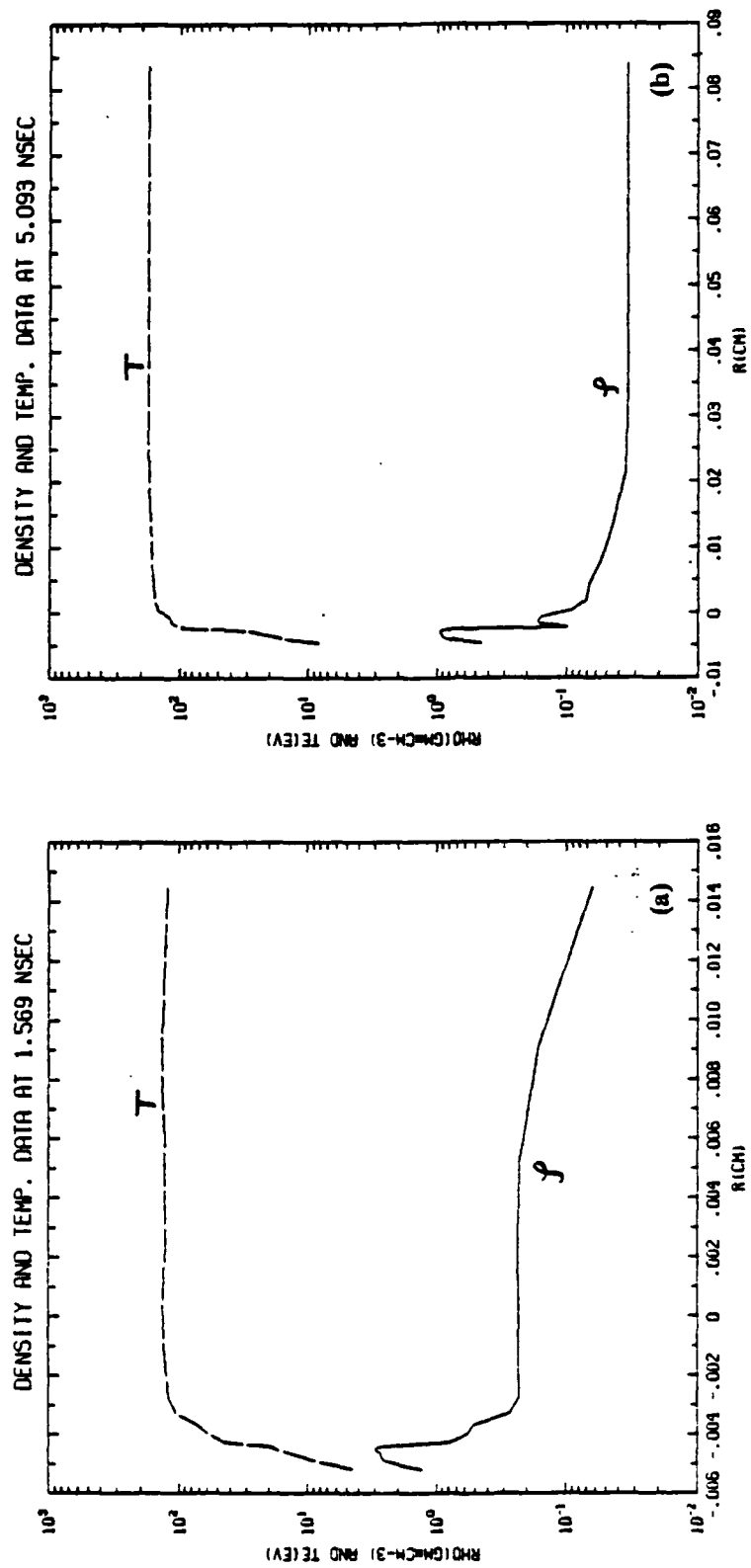


Fig. 3 — Plasma density and temperature profiles at various times.

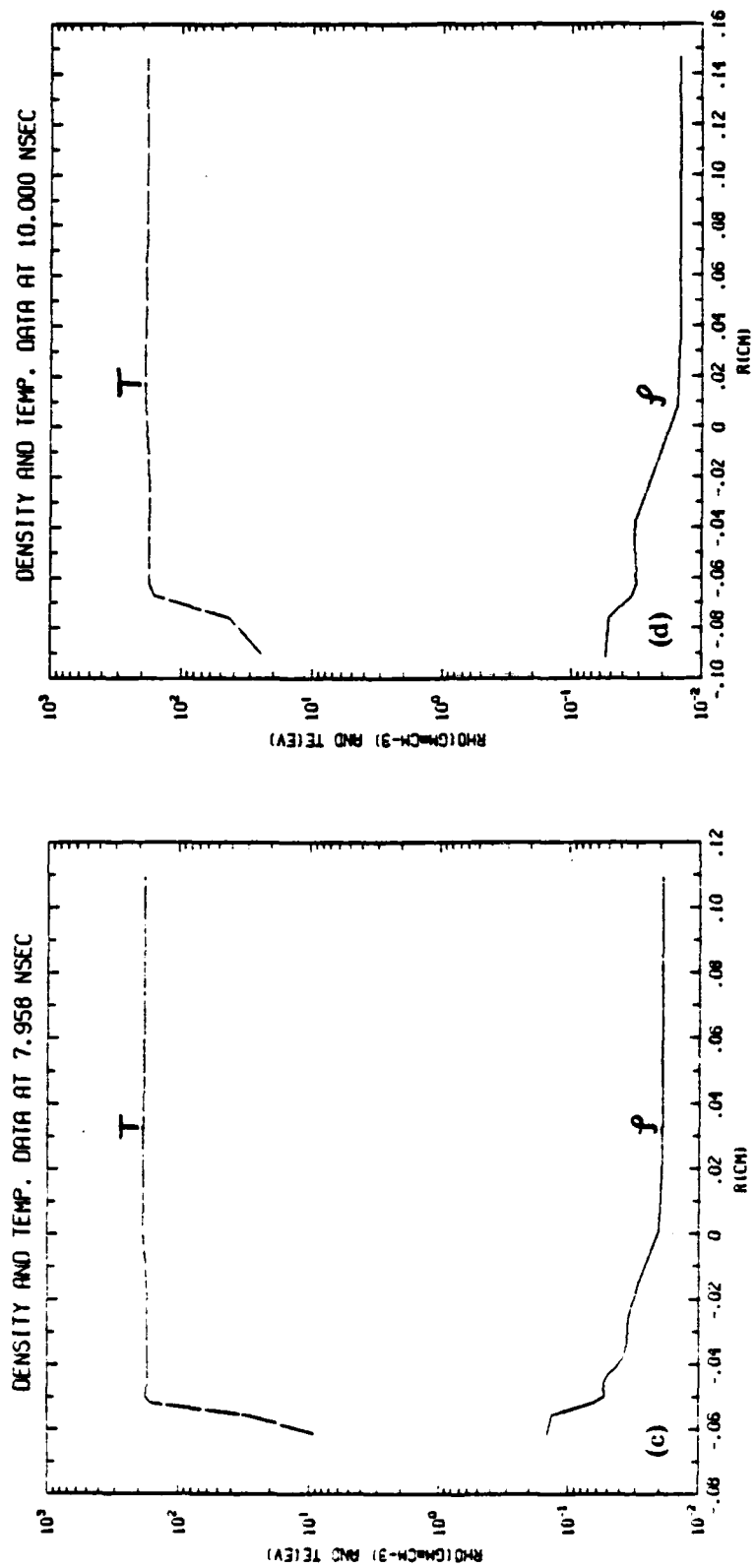


Fig. 3 (Cont'd) — Plasma density and temperature profiles at various times.

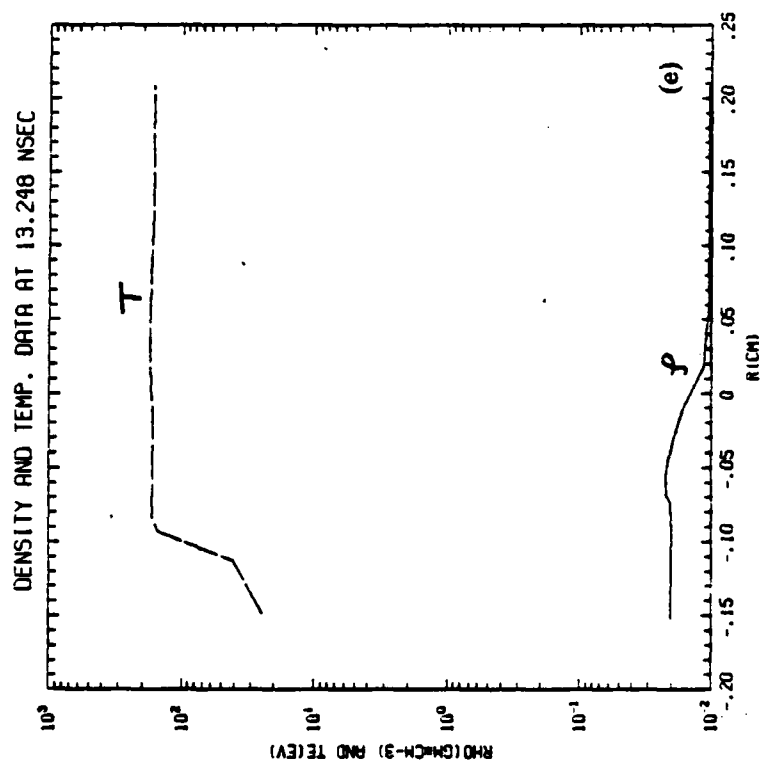


Fig. 3 (Cont'd) — Plasma density and temperature profiles at various times.

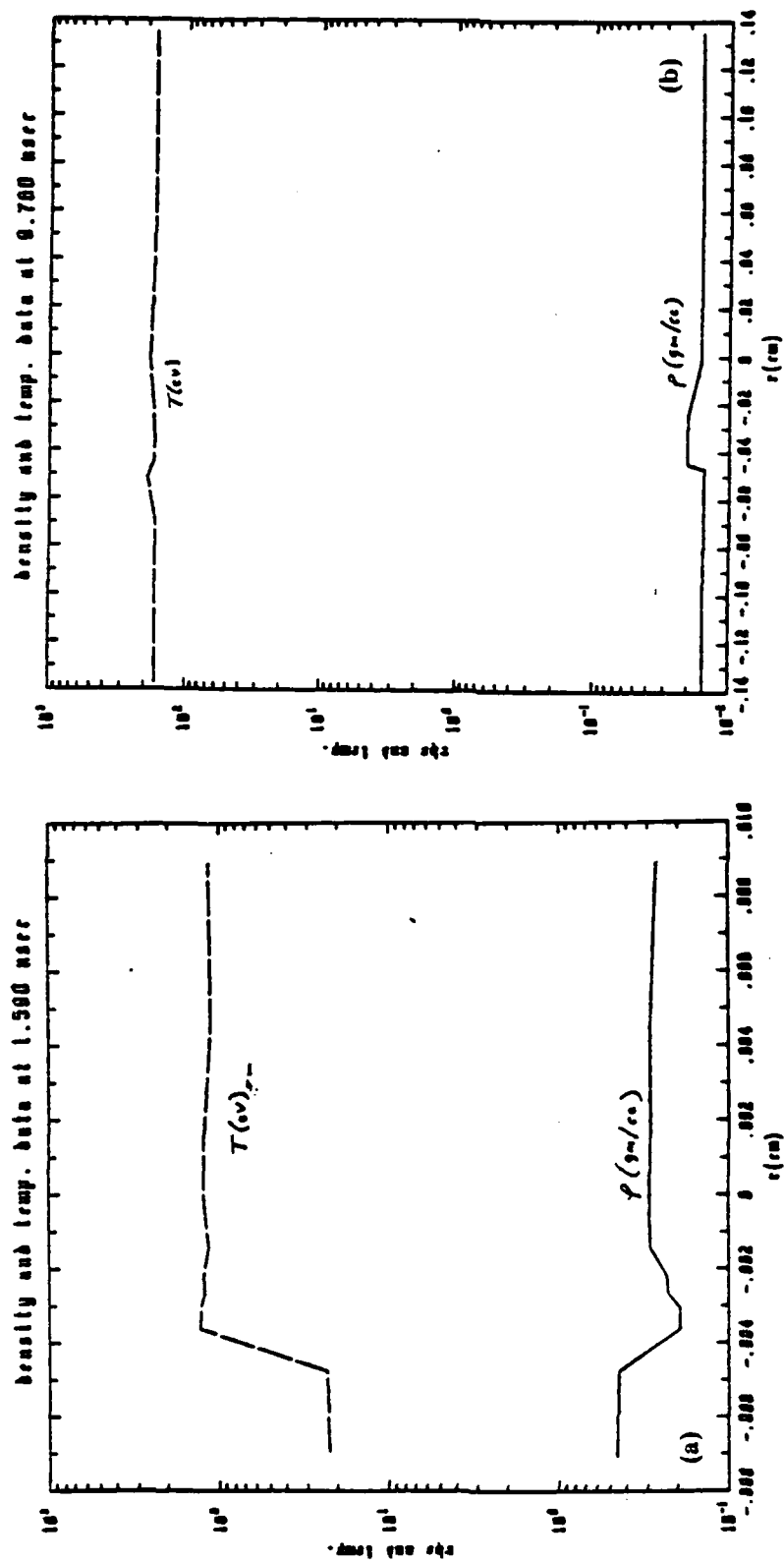


Fig. 4 — Plasma density and temperature profiles from the previous treatment.⁶

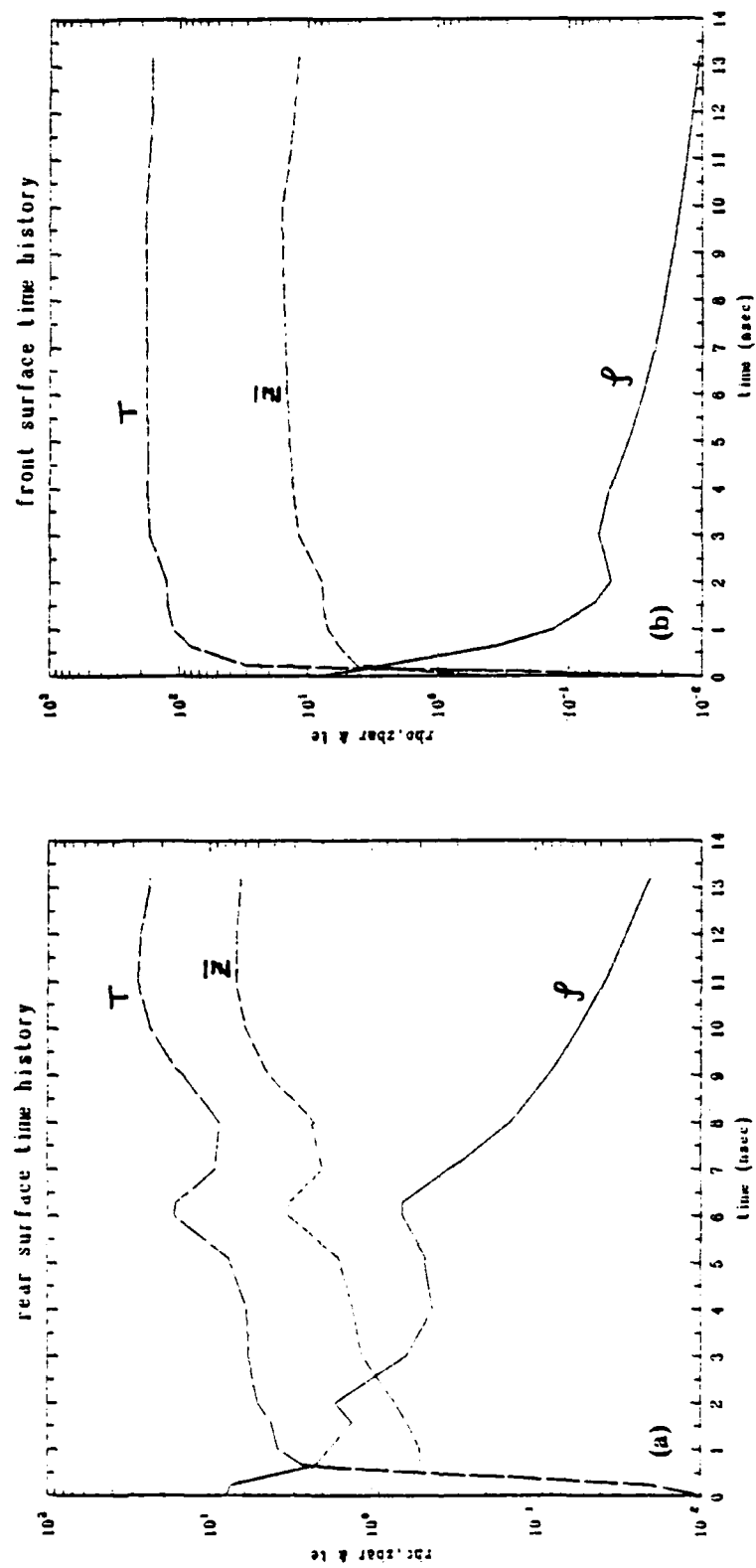


Fig. 5 — Time behavior of the temperature, density, and average charge at the front and rear plasma surfaces.

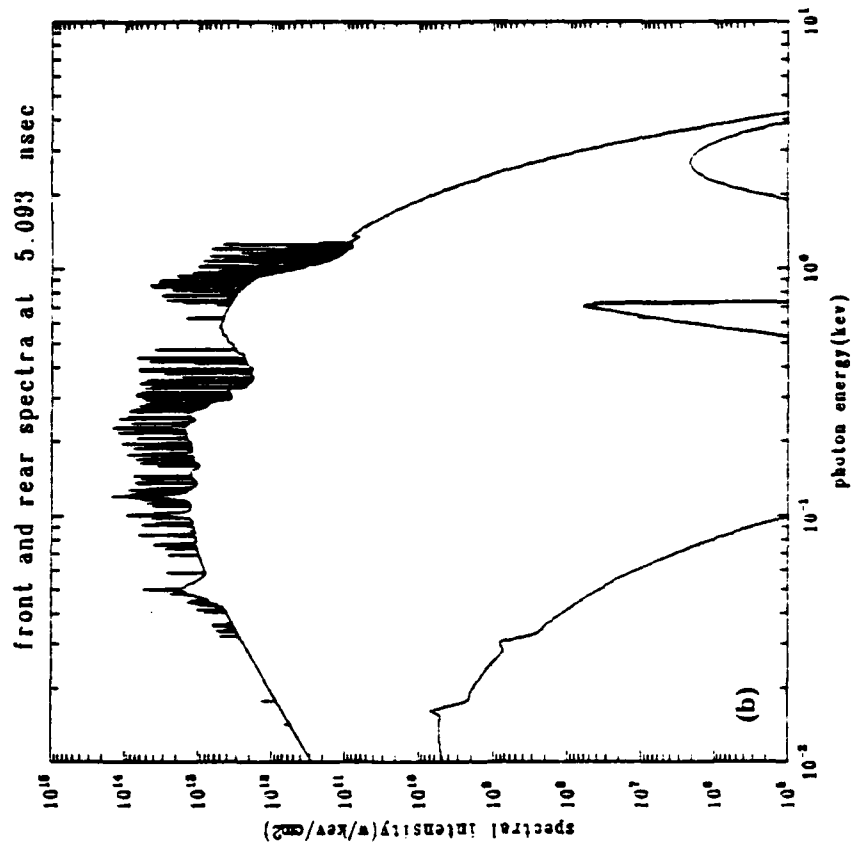
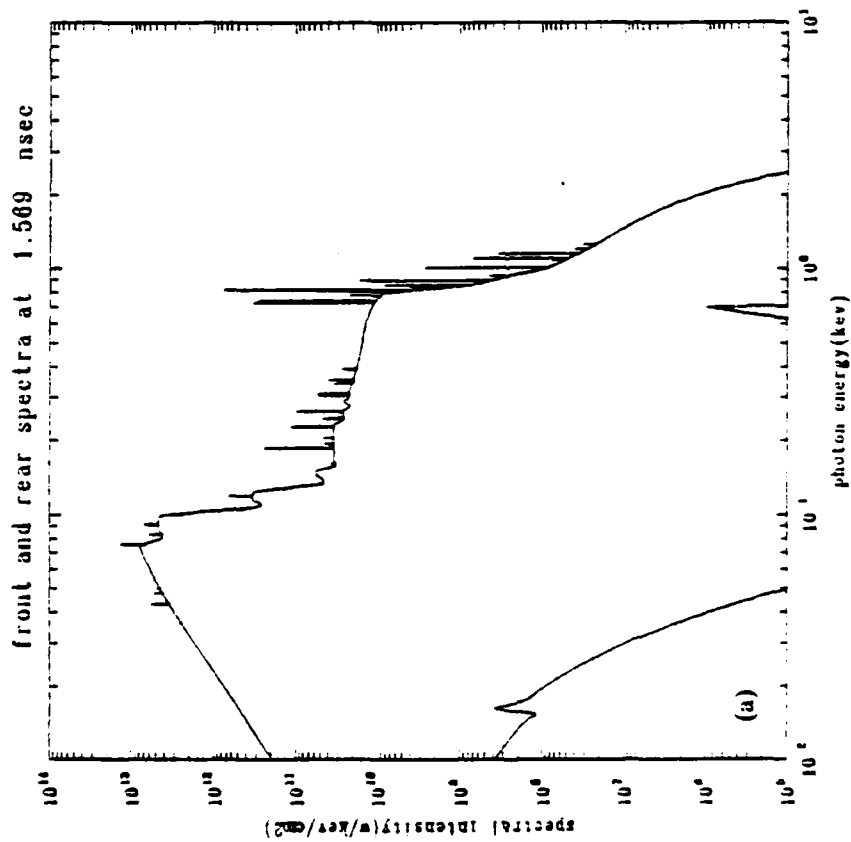


Fig. 6 — Calculated front and rear spectra at various times.

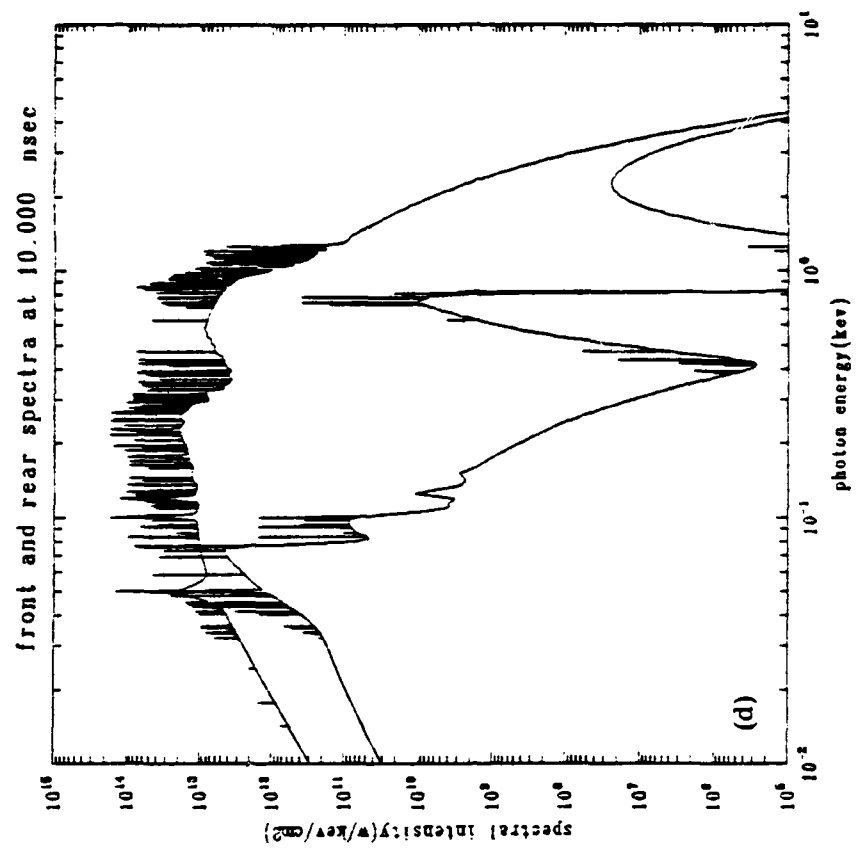
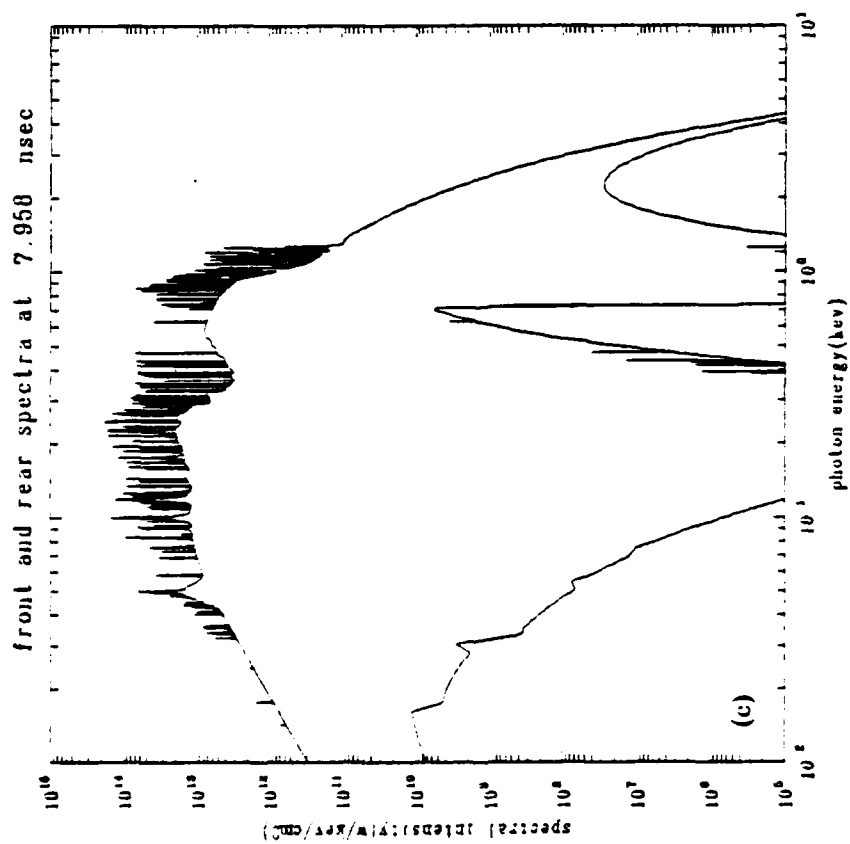


Fig. 6 (Cont'd) — Calculated front and rear spectra at various times.

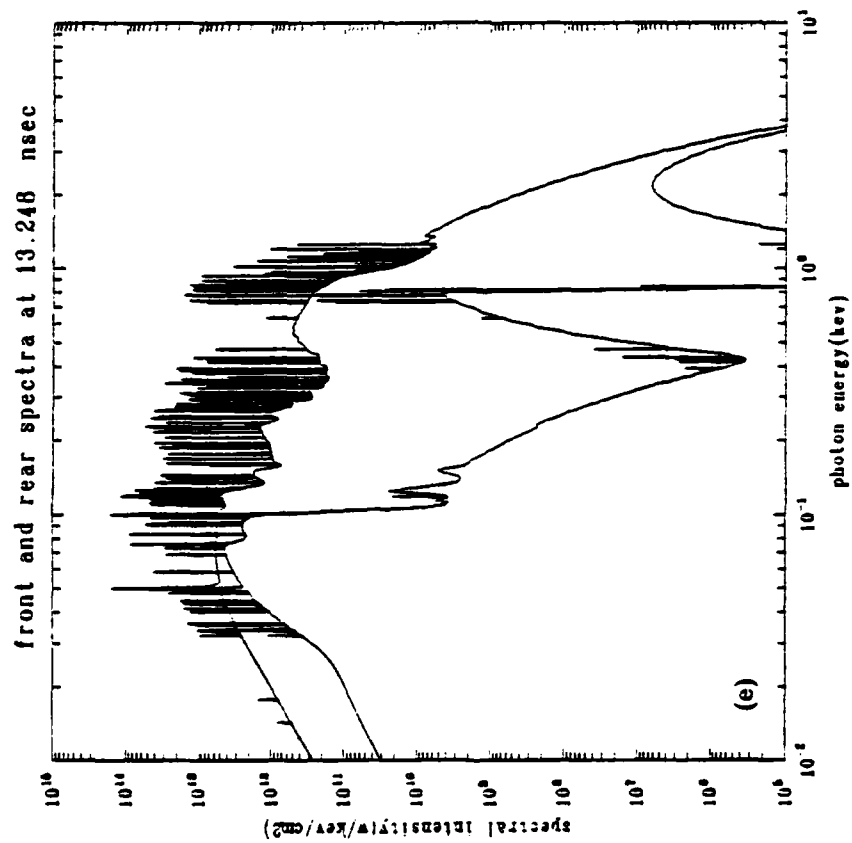


Fig. 6 (Cont'd) — Calculated front and rear spectra at various times.

B. Non-LTE Electron Distributions in Electrical Discharges

I. INTRODUCTION

The electron energy distribution function is the connecting link between the electrical and radiative behavior of electrical discharges; namely, it determines both the strength of the discharge's electrical and thermal conductivities as well as the strength of the ionization and excitation rates, and therefore the radiation loss rates. Thus, it is essential that electron distribution functions be calculated for pulse power x-ray machines, which should be designed to be as energy efficient as is physically possible in converting the heated free electron energy distributions to kilovolt x-rays. Without a good knowledge of the dynamics of the electron distribution function, the full potentialities of pulse power x-ray generators cannot be well assessed.

From the electrical and thermal conductivities, one calculates the current distributions (and thus the details of the implosion dynamics). Moreover, it has long been appreciated that the conduction properties of pulse power loads are anomalous, i.e. they are not understood in terms of classically calculated Spitzer conductivities. Within the DOE ICF community, flux correctors have long been in use to sharply reduce classical heat conduction in steep temperature and density gradients. Experience has also taught this community that the values of the flux corrector can change markedly depending on experimental conditions. Its use also contributes to the poor agreement that is usually obtained in matching theory with detailed experimental x-ray data.

II. PAST TREATMENTS

There are several inconsistent features to past treatments of the electron distribution function problem. For ionization calculations, it is generally assumed that the electrons have Maxwellian distributions $f^M(E)$, which is equivalent to assuming that the free electrons are in local thermodynamic equilibrium (LTE). $E = 1/2 m v^2$ is the electron kinetic energy. In order to compute electrical and thermal conductivities, however, one must assume from the beginning that the electron distribution function

f is non-Maxwellian and that it depends both on the electron energy E and on the cosine of the angle μ that the electron motion has with respect to the net effects of electric fields and plasma gradients. In lowest order approximation

$$f(E, \mu) = f_0(E) + \mu f_1(E)$$

f_1 is then determined as a local function of f_0 under the often false assumption that elastic collisions are always dominant. Spitzer conductivity is calculated in this manner and is widely used, with flux correctors, in hydrodynamics codes. However, electrical and thermal conductivities calculated in this way,

1. do not treat the effect of inelastic collisions on f and therefore apply only to fully ionized, hydrogenic plasmas
2. assume Maxwellian f_0
3. are not valid at high electric field strengths or in steep temperature or density gradients
4. do not treat transient time behavior, i.e. any effects due to the rapid rise in electric field.

Both electrical and thermal conductivities and excitation and ionization rates depend primarily on the shape of the high energy tail of f . Thus, the energetics of pulse power x-ray simulators has two key features. Not only must the electrons be bulk heated but this energy must flow continuously into the high energy tail of the electron distribution to replenish the energy that is lost when electrons collide inelastically with ions that radiate away the excitation energy. Energy that is fed into the high energy tail of f is also associated, however, with the problem of runaway electrons that decouple from the plasma altogether and lose their energy by colliding with the anode. However, runaway behavior has only been

analyzed in the absence of inelastic collisions, whose cross-sections do not fall off as rapidly with energy as do elastic cross-sections. Hence, the runaway electron problem has not been properly analyzed to date though it clearly bears on a potentially major energy inefficiency mechanism.

To briefly summarize the present situation, plasma conductivities and the details of power flow are both interrelated and time evolving characteristics of imploding z-pinchs that are impossible to experimentally measure directly. They must, therefore, be self-consistently calculated. However, in the past, the few people who have calculated the change in ionization level caused by non-Maxwellian electrons have failed to correlate this effect with changes in electrical conductivity. Also their calculations, were carried out only for hydrogen plasmas and showed large reductions in the number of high energy electrons. In a z-pinch, these electrons are needed in abundance to excite the K-shell of ions, thereby producing the kilovolt radiation. On the other hand, people who have calculated electrical conductivities, find that the high energy tail of the electron distribution is enhanced by the electric field, leading also to runaway electrons. These calculations, however, ignore inelastic collisions and the electric field effects on ionization balance. Calculated runaway electron production rates also agree poorly with experiment. Finally, recent work on the effects of steep gradients on heat flow have shown that the process is nonlocal, i.e., no longer described by the local gradient in temperature, and that the high energy tail of the electron distribution may either be depleted or populated relative to a Maxwellian by this energy flow.

III. APPROACH

As was done in the determination of the ionization balance and radiation loss rates of different atomic weight plasmas, the problem of calculating the electron energy distribution function is being approached as one involving moderate-Z, partially ionized, non-LTE plasmas. Thus, a model is being developed that will allow the Z-scaling behavior of plasma conductivities and plasma ionization balance to be calculated as a function of the strong and rapidly changing E and B fields of an imploding Z-pinch.

To begin the electron calculation, atomic models of hydrogen and argon plasmas are being developed. The hydrogen model is important for several reasons. One, it is an important dilutant to be used in the study of the implosion dynamics of mixed element loads. It is ionized quickly during the initial phases of the implosion and provides an additional sources of electrons for plasma heating and for enhancing excitation and ionization rates of the moderate-Z elements in the mixture. Two, a hydrogen model is easily scaled for use in the development of K-shell models for moderate-Z plasmas. And three, it is an atomic system for which much is known and for which conductivity and ionization balance calculations can be benchmarked. The argon model, on the other hand, will be developed to demonstrate that the calculation will also work in general for moderate-Z elements and to determine Z-scaling effects that will occur because of the different non-LTE behaviors of different ionization stages. The excitation of the argon system will also show different transient ionization and conductivity behavior.

The calculation of electron distributions from inelastic scattering processes entails a new approach to the problem of ionization equilibria as well. One must work with cross-sections rather than rate coefficients, which are to be obtained in this case as cross-section averages using the actual rather than an assumed Maxwellian electron distribution. Moreover, the cross-sections must be expanded in the same way as f , i.e., their angular distribution must be known in order to carry out the conductivity calculation.

IV. FUTURE

The main goal of the present effort is to self-consistently incorporate the effects of inelastic collisions in the calculation of the shape of the distribution function f_0 and on the ionization balance and radiation loss rates. A conductivity calculation will then be set up at first using this non-Maxwellian f_0 and then setting up a calculation that includes the simultaneous effects of a strong E field and inelastic collisions on f_0 and f_1 . These calculations will be applied to an investigation of the power flow problem in imploding z-pinchs. These calculations will be applied mainly to critique implosion behavior in

regions of the z-pinch plasma where the additional effects of a strong magnetic field on conductivity can be safely ignored. Finally, self-consistent nonlocal electron transport and magnetic field effects will be added to the calculation and investigated as long term goals of this effort.

I. Acknowledgments

This work was supported by the Defense Nuclear Agency. We would like to thank Mr. Jonathan Farber for his continued interest in and encouragement of this work and for his suggestion some years ago that double gas puffs had possible application as plasma radiator sources and switches. Thanks are also due to Lt. Col. Joel Benson for his assistance in organizing periodical working group meetings. Finally, we thank Drs. F. Young and S. Stephanakis, P. Burkhalter, and C. Melman of NRL, S. Wong of Physics International, and N. Pereira of Berkeley Research Associates for sharing their data, expertise, and ideas with us.

DISTRIBUTION LIST

Assistant to the Secretary of Defense Atomic Energy Washington, D.C. 20301 ATTN: Executive Assistant	1 Copy
Defense Technical Information Center Cameron Station 5010 Duke Street Alexandria, Va 22314	2 copies
Director Defense Intelligence Agency Washington, D.C. 20301 ATTN: DT-1B R. Rubenstein	1 Copy
Director Defense Nuclear Agency Washington, D.C. 20305 ATTN: DDST ATTN: TITL ATTN: RAEV ATTN: STVI	1 copy 4 copies 1 copy 1 copy
Commander Field Command Defense Nuclear Agency Kirtland AFB, New Mexico 87115 ATTN: FCPR	1 Copy
Chief Field Command Livermore Division Department of Defense P.O. Box 808 Livermore, CA 94550 ATTN: FCPRL	1 Copy
Director Joint Strat TGT Planning Staff Offutt AFB Omaha, Nebraska 68113 ATTN: JLKS	1 Copy
Undersecretary of Defense for RSCH and ENGRG Department of Defense Washington, D.C. 20301 ATTN: Strategic and Space Systems (OS)	1 Copy

Deputy Chief of Staff for RSCH DEV and ACQ
Department of the Army
Washington, D.C. 20301
ATTN: DAMA-CSS-N 1 Copy

Commander 1 copy each
Harry Diamond Laboratories
Department of the Army
2800 Powder Mill Road
Adelphi, MD 20783
ATTN: DELHD-N-NP
ATTN: DELHD-R J. Rosado
ATTN: DELHD-TA-L (Tech. Lib.)

U.S. Army Missile Command
Redstone Scientific Information Center 3 Copies
Attn: DRSMI-RPRD (Documents)
Redstone Arsenal, Alabama 35809

Commander 1 copy
U.S. Army Missile Command
Redstone Arsenal, Alabama 35898
ATTN: DRCPM-PE-EA

Commander
U.S. Army Nuclear and Chemical Agency
7500 Backlick Road 1 copy
Building 2073
Springfield, VA 22150
ATTN: Library

Commander 1 Copy
Naval Intelligence Support Center
4301 Suitland Road, Bldg. 5
Washington, D.C. 20390
ATTN: NISC-45

Commander 1 Copy
Naval Weapons Center
China Lake, California 93555
ATTN: Code 233 (Tech. Lib.)

Officer in Charge 1 Copy each
White Oak Laboratory
Naval Surface Weapons Center
Silver Spring, Md. 20910
ATTN: Code R40
ATTN: Code F31

Air Force Weapons Laboratory Kirtland AFB, New Mexico 87117 ATTN: SUL ATTN: CA ATTN: APL ATTN: Lt. Col Generosa	1 Copy each
Deputy Chief of Staff Research, Development and Accounting Department of the Air Force Washington, D. C. 20330 ATTN: AFRDQSM	1 Copy
Commander U.S. Army Test and Evaluation Command Aberdeen Proving Ground, MD 21005 ATTN: DRSTE-EL	1 Copy
AVCO Research and Systems Group 201 Lowell Street Wilmington, MA 01887 ATTN: Library A830	1 Copy
BDM Corporation 7915 Jones Branch Drive McLean, Virginia 22101 ATTN: Corporate Library	1 Copy
Berkeley Research Associates P.O. Box 983 Berkeley, CA 94701 ATTN: Dr. Joseph Workman	1 Copy
Berkeley Research Associates P.O. Box 852 5532 Hempstead Way Springfield, VA 22151 ATTN: Dr. Joseph Orens	1 Copy each
Boeing Company P. O. Box 3707 Seattle, WA 98134 ATTN: Aerospace Library	1 Copy
The Dikewood Corporation 1613 University Bldv., N.E. Albuquerque, New Mexico 87110 ATTN: L. Wayne Davis	1 Copy

General Electric Company Space Division Valley Forge Space Center P. O. Box 8555 Philadelphia, PA 19101 ATTN: J. Peden	1 Copy
General Electric Company - Tempo Center for Advanced Studies 816 State Street P.O. Drawer QQ Santa Barbara, CA 93102 ATTN: DASIAC	1 Copy
Institute for Defense Analyses 1801 N. Beauregard St. Alexandria, VA 22311 ATTN: Classified Library	1 Copy
IRT Corporation P.O. Box 81087 San Diego, CA 92138 ATTN: R. Mertz	1 Copy
JAYCOR 11011 Forreyane Rd. P.O. Box 85154 San Diego, CA 92138 ATTN: E. Wenaas F. Felbar	1 Copy
JAYCOR 205 S. Whiting Street, Suite 500 Alexandria, VA 22304 ATTN: R. Sullivan	1 Copy
KAMAN Sciences Corp. P. O. Box 7463 Colorado Springs, CO 80933 ATTN: Library	1 copy each
Lawrence Livermore National Laboratory University of California P.O. Box 808 Livermore, California 94550 Attn: DOC CDN for L-153 Attn: DOC CDN for L-47 L. Wouters Attn: DOC CDN for Tech Infor. Dept. Lib.	1 copy each
Lockheed Missiles and Space Co., Inc. P. O. Box 504 Sunnyvale, CA 94086 Attn: S. Taimlty Attn: J.D. Weisner	1 copy each

Lockheed Missiles and Space Co., Inc.
3251 Hanover Street
Palo Alto, CA 94304
Attn: J. Perez

1 Copy

Maxwell Laboratory, Inc.
9244 Balboa Avenue
San Diego, CA 92123
ATTN: A. Kolb
ATTN: M. Montgomery
ATTN: J. Shannon

1 Copy each

McDonnell Douglas Corp.
5301 Bolsa Avenue
Huntington Beach, CA 92647
ATTN: S. Schneider

1 Copy

Mission Research Corp.
P. O. Drawer 719
Santa Barbara, CA 93102
ATTN: C. Longmire
ATTN: W. Hart

1 Copy each

Mission Research Corp.-San Diego
5434 Ruffin Rd.
San Diego, California 92123
ATTN: Victor J. Van Lint

1 Copy

Northrop Corporation
Northrop Research and Technology Center
1 Research Park
Palos Verdes Peninsula, CA 90274
ATTN: Library

1 Copy

Northrop Corporation
Electronic Division
2301 120th Street
Hawthorne, CA 90250
ATTN: V. Damarting

1 Copy

Physics International Company
2700 Merced Street
San Leandro, CA 94577
ATTN: C. Stallings
ATTN: C. Gilman
ATTN: S. Wong

1 Copy each

R and D Associates
P.O. Box 9695
Marina Del Rey, CA 90291
ATTN: W. Graham, Jr.
ATTN: P. Haas

1 Copy each

Sandia National Laboratories P.O. Box 5800 Albuquerque, New Mexico 87115 ATTN: Doc Con For 3141 ATTN: D. McDaniel ATTN: P. VanDevender ATTN: K. Matzen, Code 4247	1 copy each
Science Applications, Inc. P. O. Box 2351 La Jolla, CA 92038 ATTN: R. Beyster	1 copy
Spire Corporation P. O. Box D Bedford, MA 01730 ATTN: R. Little	1 copy
SRI International 333 Ravenswood Avenue Menlo Park, CA 94025 ATTN: S. Dairiki	1 copy
S-CUBED P. O. Box 1620 La Jolla, CA 92038 ATTN: A. Wilson	1 copy
Director Strategic Defense Initiative Organization 1717 H Street Pentagon 20301-7100 ATTN: DE Lt. Col Richard Gullickson/DEO IST Dr. Dwight Duston ATTN: IST Dr. J. Ionson	1 copy each
Texas Tech University P.O. Box 5404 North College Station Lubbock, TX 79417 ATTN: T. Simpson	1 copy
TRW Defense and Space Systems Group One Space Park Redondo Beach, CA 90278 ATTN: Technical Information Center	1 Copy
University of Buffalo Dept. of Electrical Engineering Attn: Prof. J. Sargent 3435 Main Street Buffalo, New York 14214	1 Copy

Naval Research Laboratory

Plasma Radiation Branch

Washington, D.C. 20375-5000

Code 4720 - 50 Copies

Code 4700 - 26 Copies

Code 2628 - 20 Copies

Code 1220 - 1 Copy

Director of Research

U. S. Naval Academy

Annapolis, MD 21402 1 Copy

END

DTic

6-86